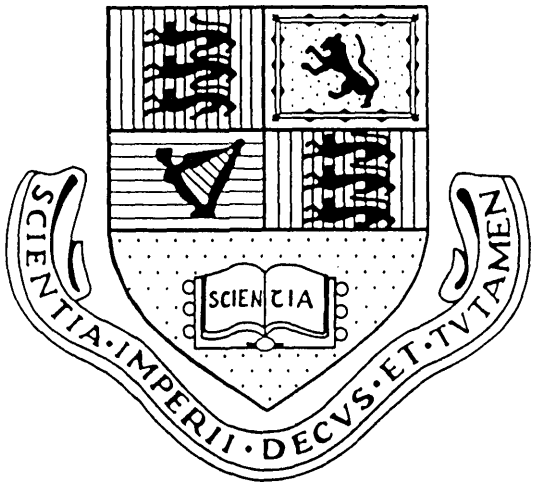
A thesis entitled

THE GROWTH AND CHARACTERIZATION OF α-Sn FILMS PSEUDOMORPHICALLY GROWN ON InSb SUBSTRATES BY MOLECULAR BEAM EPITAXY

by

Wing Kwan LIU



Submitted to the University of London for the degree of
Doctor of Philosophy and Diploma of Imperial College

Solid State Experimental Group
Blackett Laboratory
Imperial College, London.

1991

ABSTRACT

This thesis describes the growth and characterization of α-Sn films pseudomorphically grown on InSb substrates by molecular beam epitaxy (MBE). Semiconducting properties of α-Sn and the basic principles of MBE growth are briefly reviewed.

Several cleaning techniques for InSb substrates are studied using X-ray photoemission spectroscopy, Auger electron spectroscopy, reflection high energy electron diffraction (RHEED) and Nomarski microscopy. The most satisfactory result is achieved using a modified CP4A etchant (HNO_3 : CH_3COOH : HF : DI H_2O @ 2 : 1 : 1 : 10) followed by a combination of low energy Ar ion bombardment (~ 350 eV) and low temperature annealing (~ 275°C).

The growth of α-Sn films is carried out in a custom-designed MBE system. The effect of growth conditions on the surface quality and stability of the α-Sn films is studied using RHEED, optical microscopy and Auger composition profiling. Coherent, single-phase α-Sn films more than 1500Å thick can be grown only on InSb substrates with (100) orientation. The $\alpha \rightarrow \beta$ phase transition temperature, used as a measure of stability of α-Sn films, is found to be dependent on the overlayer thickness. Thinner films are found to have a higher transition temperature than thicker ones. Due to enhanced migration of surface adatoms, films grown at elevated substrate temperatures and slow growth rates produce sharper RHEED patterns which correspond to better surface ordering. On the other hand, preferential diffusion of Sb into the overlayer can be detected in films grown under these conditions. The optimum growth conditions are achieved using growth rates in the range of 0.5 to 0.7 Å/s and substrate temperatures between 10°C and 50°C. Using this set of growth conditions, high quality α-Sn films with good surface morphology can be stabilized to temperatures up to ~100°C.

A detailed investigation of the surface structure of α-Sn films grown on InSb(100) is carried out using the RHEED technique. The importance of employing a multi-azimuthal and multi-Laue zone approach is emphasized. The observation of curved 1/2-order diffraction streaks along <100> azimuths of the InSb surface prior to growth is explained in terms of the presence of 1-D disorder boundaries. The initial stage of α-Sn film growth is

characterized by disorder features. Above 20Å coverage, growth proceeds in a layer-by-layer mode and the α-Sn films are found to exhibit thickness-dependent surface reconstructions. Two-domain (2x1), (2x2), c(4x4) as well as atomic step structures are observed. The surface structure of α-Sn(100) is found to be very similar to that of Si(100) and a structural model based on dimers is proposed.

The electrical properties of the α-Sn/InSb system are found to be dominated by a high concentration, high mobility two-dimensional electron gas (2DEG) at the interface. Due to multi-carrier conduction effects, electrical data from Hall measurements are difficult to analyze and require careful interpretation. Instead, Shubnikov-de Haas (SdH) effect and magneto-optical techniques are used. Two-dimensionality of the electron gas is demonstrated by the $1/\cos\vartheta$ (ϑ is the tilt angle with respect to the normal of the 2DEG plane) dependence of the observed SdH oscillations. The total carrier concentration of the 2DEG is around 6×10^{12} cm^{-2} with at least seven subbands being occupied at 4.2K. Individual subband occupancy is found to be dependent on the overlayer thickness. Magneto-optical spectra for α-Sn/InSb samples are very complicated. In addition to bound hole transitions in the substrate, several broad structures with different overlayer thickness dependence can also be observed. These structures are believed to arise from cyclotron resonance transitions involving the 2DEG (corresponding to effective masses between $0.044m_o$ to $0.051m_o$) and the warped energy surfaces of the highly-strained pseudomorphic α-Sn overlayer (corresponding to $0.018m_o$ and between $0.028m_o$ to $0.034m_o$). Possible reasons for the occurrence of the 2DEG are discussed in terms of substrate cleaning and cross-doping artefacts, quantum size effects and band-bending effects at the α-Sn/InSb interface.

ACKNOWLEDGEMENT

I would like to thank Prof. R. A. Stradling for his supervision and helpful suggestions on different aspects of this project.

I am especially grateful to Dr. W. T. Yuen for designing the MBE system, for his encouragement and guidance throughout the course of my studies and with whom I shared much of the experimental workload and results. Without his perseverance, progress in this project would not be possible.

I am thankful to Prof. B. A. Joyce for some stimulating discussions on MBE growth and RHEED studies, and for reading over the manuscript of this thesis.

I would also like to thank all members of the Solid State Experimental Group and the IRC for semiconductor materials, in particular Steve Cussell, Harminder Flora and Derek Podger for technical assistance, and Neal Powell, Meilin Sancho, Nick Jackson and Dr. N. D. Lisgarten for their help in preparing the illustrations and photographs for this thesis.

The continual support of my parents and the encouragement of Dicky Yan throughout the past three years are deeply appreciated.

Finally, I would like to thank the Committee of Vice-Chancellors and Principles of the Universities of the United Kingdom for the provision of an Overseas Research Students Award.

CONTENTS

		page
ABSTRACT		1
ACKNOWLEDGEMENT		3
CONTENTS		4
Chapter 1	INTRODUCTION	6
Chapter 2	REVIEW ON THE SEMICONDUCTING PROPERTIES OF α-Sn	
	2.1 Introduction	8
	2.2 Properties of Bulk α-Sn	9
	2.3 Brief Survey of Thin Film α-Sn and Related Materials	14
Chapter 3.	FUNDAMENTALS OF MOLECULAR BEAM EPITAXY	
	3.1 Introduction	22
	3.2 Theories of Epitaxial Growth	23
	3.3 Basic Principles of Molecular Beam Epitaxy	25
	3.4 Pseudomorphic Growth and Stabilization of Metastable Phases	27
	3.5 Heteroepitaxial and Non-polar on Polar Growth	30
Chapter 4.	SUBSTRATE PREPARATION	
	4.1 Introduction	33
	4.2 *Ex-situ* Cleaning	34
	4.3 *In-situ* Cleaning	51
	4.4 Conclusions	66
Chapter 5.	MBE GROWTH OF SUBSTRATE-STABILIZED α-Sn	
	5.1 Introduction	68
	5.2 System Configuration	69
	5.3 System Operation	78
	5.4 Growth Studies	80
Chapter 6.	STRUCTURAL PROPERTIES OF α-Sn : A RHEED STUDY	
	6.1 Introduction	89
	6.2 Fundamentals of RHEED	89
	6.3 Multi-azimuthal Analysis	94
	6.4 Interpretation of RHEED Patterns	95
	6.5 Experimental	105
	6.6 Structural Models for α-Sn(100) Surfaces	115
	6.7 Conclusions	121

Chapter 7. MAGNETO-TRANSPORT AND MAGNETO-OPTICAL PROPERTIES OF α-Sn
7.1 Introduction 124
7.2 Hall Effect Measurements 125
7.3 Shubnikov-de Haas Effect Measurements 132
7.4 Far Infrared Magneto-optical Measurements 149
7.5 Conclusions 157
Chapter 8. CONCLUSIONS 158
Appendix LIST OF PUBLICATIONS 161
REFERENCES 162

CHAPTER 1 INTRODUCTION

It has long been known that the group IV element tin (Sn) can undergo a transformation from its usual metallic (β) phase to a semiconducting (α) phase when the temperature drops below 13.2°C. Apocryphal tales relating the woes suffered as a result of this phase transformation are legion, e.g., it is claimed that Napoleon's winter retreat from Moscow was seriously impeded by the fact that tin trouser buttons and bullets were used by his army.

Scientifically, α-Sn is generally accepted as a symmetry-induced zero-bandgap semiconductor. By applying a uniaxial stress or by alloying this material with Ge, a very small energy gap can be opened up, giving rise to potential infrared device applications. After the extensive investigations on the electrical and magnetic properties of bulk α-Sn by Ewald and his co-workers in the late 1950s, very little activity concerning this material was reported in the following decade. The main reason for this can be attributed to the instability of the semiconducting α-phase of bulk Sn which makes sample preparation extremely difficult and hindered the prospect of ambient temperature device applications. It was not until the advent of the molecular beam epitaxy (MBE) technique which enables the growth of substrate-stabilized α-Sn thin films with phase transition temperatures above 70°C, that research interest in α-Sn and its alloys was revived.

The work described in this thesis is concerned with the growth and characterization of α-Sn films pseudomorphically grown on InSb substrates by molecular beam epitaxy (MBE). It begins with a review on the semiconducting properties of α-Sn in which the probable band structure of the bulk material and the properties of α-Sn-related thin films are discussed. In chapter 3, the principles of molecular beam epitaxy and special features concerning the growth of α-Sn/InSb such as pseudomorphism, substrate-stabilization and non-polar/polar epitaxy are discussed. Several substrate preparation techniques are described in chapter 4. The credibility of each method is assessed using surface science techniques such as X-ray photoemission (XPS), Auger electron spectroscopy (AES), reflection high energy electron diffraction (RHEED) and Nomarski microscopy. Chapter 5 gives a brief description of the MBE system used in this work. The effect of growth

conditions such as substrate orientation, overlayer thickness, growth rate and substrate temperature on the quality and stability of the α-Sn films is presented. A detailed study of the surface structure of α-Sn/InSb(100) using RHEED is given in the following chapter. The RHEED technique and the interpretation of diffraction patterns are briefly reviewed. A comparison between the structure of the α-Sn(100) surface and that of Si(100) is then presented. Finally in chapter 7, the range of magneto-transport and magneto-optical techniques used for sample characterization is outlined and the experimental results are summarized. The effect of the presence of an interfacial two-dimensional electron gas (2DEG) on the electrical properties of the α-Sn/InSb samples is also discussed.

CHAPTER 2 REVIEW ON THE SEMICONDUCTING PROPERTIES OF α-Sn

2.1 Introduction

According to early studies of the electronic properties of bulk α-Sn, it is generally considered that this low temperature phase of Sn is a zero-bandgap semiconductor.[1] Unlike the other group IV semiconductors, namely Si and Ge, which also have the diamond structure, α-Sn has so far received much less attention despite its natural occurrence. In the past, unless special precautions were taken, bulk α-Sn was always obtained in powder form on which electrical measurements were difficult to perform.[1] In the late 1950s, Ewald and co-workers successfully grew single crystal α-Sn from a solution in mercury.[2] The ensuing extensive investigations on the electrical and magnetic properties of this material led Groves and Paul[3] to propose the widely accepted band structure model for bulk α-Sn. The feature of this model is that the α-Sn conduction and valence bands belong to the same irreducible representation of the Γ_8^+ symmetry group and they are degenerate at $\mathbf{k} = 0$. Many of the semiconducting properties of bulk α-Sn have also been established.[4]

Beginning in the early 1970s, there was a long interval in which little activity concerning α-Sn was reported. This occurred partly because potential applications were severely limited by the low phase transition temperature of α-Sn samples. It has long been known that at temperatures above 13.2°C, bulk Sn can exhibit a phase transition from its semiconducting (α) phase to a metallic (β) phase accompanied by a 27% decrease in volume.[1] This apparently eliminated any prospect for ambient temperature device applications and made even routine handling of the material highly inconvenient. However, the recent advent of the molecular beam epitaxy (MBE) technique resulted in the possibility of producing substrate-stabilized α-Sn thin films which can survive at temperatures well above 300K. Success in MBE growth of α-Sn films was first reported by Farrow *et. al.*[5] in 1981. Pseudomorphically grown on InSb(100) and CdTe(100) substrates, these films were found to be substrate-stabilized to about 70°C. However, at 77K they had hole densities greater than 10^{19} cm^{-3} and mobilities ≤ 250 cm^2/Vs. More recently, Tu *et. al.*[6] have grown α-Sn films with much more attractive electrical properties : $n \approx 4x10^{17}cm^{-3}$ and μ_n as high as $1.3x10^4 cm^2/Vs$ at

77K. Large optical non-linearities at 10.6 μm have also been reported.[7] These encouraging results coupled with recent predictions that quantum well structures, comprising symmetry-induced zero bandgap semiconductors like α-Sn confined between wider bandgap semiconductors, should exhibit novel and potentially useful infrared absorption properties[8,9] have revived considerable interest in the study of α-Sn related materials and a large number of experimental data have emerged in the past few years.[10]

In this chapter, the semiconducting properties of α-Sn are briefly reviewed. In § 2.2, the probable band structure of bulk α-Sn is discussed and its electrical and magneto-transport parameters are summarized. This is followed by a brief account of the properties of α-Sn-related materials pseudomorphically grown by MBE and other fabrication techniques (§ 2.3).

2.2 Properties of Bulk α-Sn

2.2.1 Historical Background

Since the discovery of its semiconducting properties in 1950,[11] considerable progress has been made in the preparation of α-Sn samples in the form of filaments and films for more reliable determination of electrical data. In their 1960 review paper,[1] Bosch and Kern have compiled considerable amount of experimental data although rather large discrepancies between the results were found. They suggested that all the analyses that had been made could be incorrect because they all assumed a simple two-band conduction model. They also pointed out the need for further measurements on higher purity materials, in particular single crystals. In 1958, Ewald and co-workers successfully grew α-Sn by crystallization from a liquid amalgam.[2] Relatively pure single crystal samples with donor concentration as low as 5×10^{14} cm^{-3} were prepared.[12] Since then, extensive investigation of the electrical, magneto-transport and stress-related properties of α-Sn has been carried out. Measurements on α-Sn single crystals soon yielded evidence of two types of negative charge carrier and therefore three-band conduction.[4] On the basis of these experimental results, Groves and Paul[3] devised an inverted band structure model for bulk α-Sn which will be discussed in the next section.

2.2.2. Band Structure of Bulk α-Sn

Theoretical calculations of the band structure of bulk α-Sn using the orthogonalized plane-wave method (OPW) predicted that the lowest conduction band of this material is at the centre of the Brillioun zone with Γ_7^- symmetry and the highest valence band has the Γ_8^+ symmetry.[13] This is in agreement with low temperature magnetoresistance data which showed no measurable anisotropy.[14,15] Above 200K, however, the transport properties were found to be dominated by electrons in the conduction band minima having (111) symmetry.[14] Furthermore, measurements of conductivity and Hall coefficient as a function of temperature[11,16] revealed that above 150K, electrons were intrinsically excited with an activation energy of about 0.09eV for samples with impurity concentrations in the 10^{18} cm^{-3} range. These data suggested the presence of band minima having (111) symmetry (plausibly L_6^+) at a slightly higher energy above the lowest conduction band. However, this combination of (000) and (111) bands apparently contradicts the oscillatory magnetoresistance measurements[15] which give an effective electron mass of $0.02m_o$ with no apparent dependence on carrier concentration (for $n < 4x10^{16}$ cm^{-3} at 4.2K).[3]

From the above experimental data and by calculating the effective mass of the Γ_7^- electrons using the **k·p** method, Groves and Paul[3] suggested that the Γ_7^- state should be placed 0.3eV **below** the Γ_8^+ state and that the Γ_8 conduction and valence bands are degenerate at **k**=0. This structure is qualitatively different from that of the other group IV semiconductors and is a result of the systematic variation of atomic interactions down the group.[4] With increasing atomic number the Γ_7^- band, which in Si and Ge lies above Γ_8^+, moves downward. In α-Sn, it lies below the Γ_8^+ bands. Because of its interaction with the light mass Γ_8^+ valence band, the curvature of both bands is reversed.[4] The inverted Γ_8^+ light hole band becomes the α-Sn conduction band; the degeneracy point at Γ_8^+ is both the top of the valence band and the bottom of the conduction band. The bandgap is therefore zero in accord with the measured $T^{3/2}$ dependence of the intrinsic carrier concentration.[3] Results from high temperature pressure and conductivity measurements [3,14] led Groves and Paul to place the L_6^+ minima, having (111) symmetry, at ~ 0.09eV above the Γ_8^+ conduction band minima. This G-P band model explains most of the electrical and magneto-transport data satisfactorily and has been widely accept as the most probable band

structure model for bulk α-Sn. Fig. 2.1 shows a full zone band structure for this material[19] (obtained from the non-local empirical pseudo-potential method) which closely resembles the G-P model.

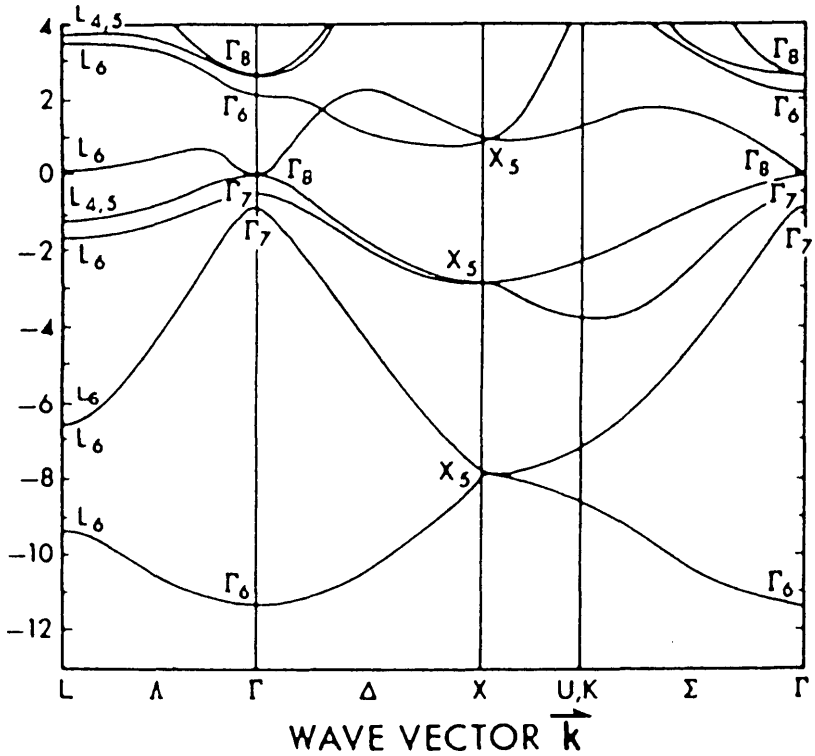


Fig. 2.1 A full zone band structure for bulk α-Sn (from Ref. 19)

2.2.3 Semiconducting Properties of α-Sn

Transport and optical parameters of bulk α-Sn determined from magneto-reflection,[12] Hall[20,21] and infrared reflectance measurements[23,24] are summarized in Table 2.1 and illustrated in association with the schematic G-P band structure in Fig. 2.2. As stated in the previous sections, bulk α-Sn is a zero bandgap semiconductor and some of its properties are summarized below :

TABLE 2.1

Parameters	Values	Ref.
$m_n^* (\Gamma_8^+)$	$0.024m_o$	15, 21, 24
$m_n^* (\Gamma_6^+)$	$0.17\text{-}0.21m_o$	20
$m_p^* (\Gamma_8^+)$	$0.195m_o$ $0.260m_o$	12 24
$m_p^* (\Gamma_7^-)$	$0.058m_o$	12
$E_g (L_6^+ - \Gamma_8^+)$ eV	0.092 @ 4.2K 0.115 @ 0K	20 24
$\mu_n (\Gamma_8^+)$ cm^2/Vs	$1.2x10^5$ @ 100K	20
$\mu_n (L_6^+)$ cm^2/Vs	$\sim 10^3$ @ 4.2K	20
μ_p cm^2/Vs	$1.0x10^4$ @ 100K	20
$\Delta(\Gamma_8^+ - \Gamma_7^+)$ eV	0.80	12
average ε	24	23

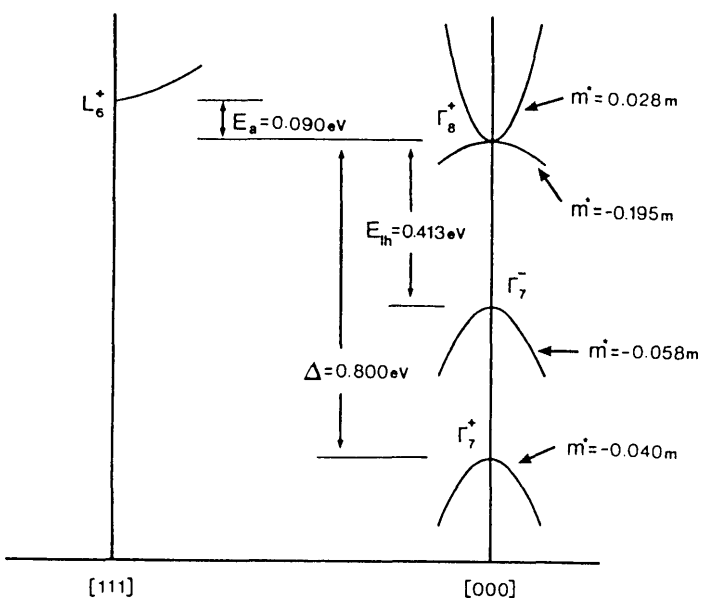


Fig. 2.2 A schematic band structure of bulk α-Sn based on the Grove and Paul model (from Ref. 12)

a) Electron mobilities at low temperature[14,15] for nominally undoped samples are in excess of $1x10^5$ cm^2/Vs and the net donor concentration[12] can be as low as $5x10^{14}$ cm^{-3}.

b) Bulk α-Sn samples with donor concentration in the range of $2.5x10^{18}cm^{-3}$ exhibit very pronounced Shubnikov-de Haas oscillations[22] as shown in Fig. 2.3. Spin-splitting features can be clearly resolved above 0.7T and the quality of the oscillations is among the best observed in semiconductor materials.

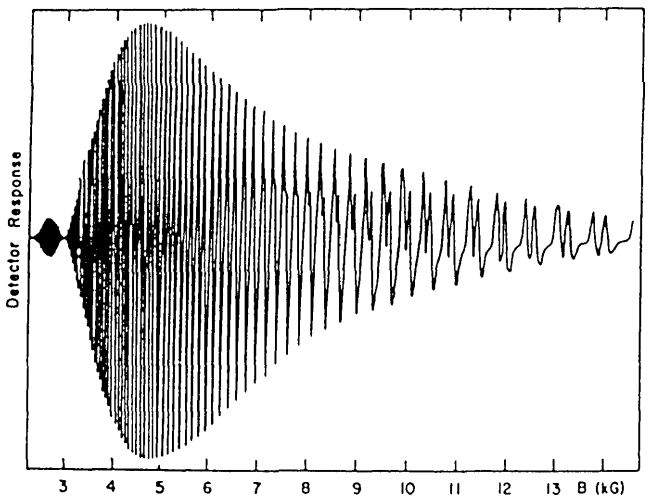


Fig. 2.3 An example of pronounced SdH oscillations obtainable from bulk α-Sn samples (from Ref. 22)

c) Degeneracy of the conduction and valence band can be lifted if the inversion symmetry of the lattice is destroyed by external perturbations such as anisotropic stress.[4] A study of the transport phenomena of uniaxially compressed α-Sn has indeed revealed the existence of a stress-dependent thermal energy gap.[25]

d) The symmetry-induced zero bandgap gives rise to an anomalous q^{-1} divergence in the static dielectric function $\varepsilon(q,0)$ at small values of q which can lead to a very effective screening of the Coulomb interactions between electrons and ionized impurities.[8,26] In the low concentration limit, this dielectric screening effect can manifest itself through an enhanced free carrier mobility at low temperature when ionized impurity scattering is dominant. Galvanomagnetic results of Lavine and Ewald[20] indicate that such a mobility enhancement does take place and a deviation

from the expected concentration dependence can be observed.

e) Being a zero bandgap semiconductor, α-Sn also exhibits all the special features characteristic of narrow bandgap materials. These include the non-parabolic dispersion of E(**k**) in the conduction band, mixed symmetry character and spin mixing in the electron wave functions, and the strong dependence of the stress-induced energy gap and effective mass on temperature, pressure, magnetic field and carrier density.[27]

2.3 Brief Survey of Thin Film α-Sn and Related Materials

It is well known that if a thin layer of a zero gap semiconductor of thickness comparable to the inelastic mean free path of carriers can be grown on a non-zero bandgap semiconductor, the conduction and valence bands will be split into subbands and a bandgap can be opened up as a result of quantum size effects.[27] α-Sn-based superlattices are thus potential infrared heterojunction detector and laser candidates with the bonus of interesting electronic properties. The theoretical bandgap of α-Sn grown on CdTe as a function of overlayer thickness calculated by Craig and Garrison[28] is shown in Fig. 2.4. Other calculations considering the dielectric response of thin α-Sn films indicate that the bulk singularities in q^{-1} and $\omega^{-1/2}$ are not present in thin films.[8] Instead, the static dielectric constant depends linearly on the α-Sn film thickness.[8] Due to a gap-independent effective mass and a drastic change in the joint density of states, the absorption coefficient of a thin α-Sn film is much higher and more abrupt than that of an alloy semiconductor with a comparable energy gap.[8,29]

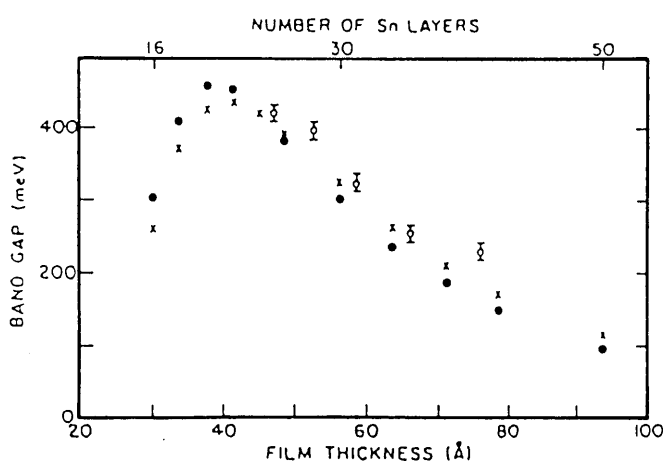


Fig. 2.4 Theoretical bandgap of epitaxial α-Sn grown on CdTe as a function of overlayer thickness (from Ref. 28)

If the lattice constant of this zero gap semiconductor is reduced, for example by alloying α-Sn with Ge, the resulting bandgap of the α-Sn_xGe_{1-x} alloy can be tailored over a wide range. Assuming a linear relationship between the band structure of both components, the indirect L_6^+- Γ_8^+ gap of Ge would turn into a direct Γ_7^-- Γ_8^+ gap of E_g ~ 0.55eV for x ~ 0.2.[30] Above this Sn concentration, the bandgap would close further eventually reaching the zero gap condition at x ~ 0.65. Fig. 2.5 is a schematic illustration of the postulated band structure variation with alloy composition.[31] Due to the greatly reduced polar scattering, these α-Sn_xGe_{1-x} alloys can exhibit very high carrier mobilities. Their potential in infared device applications, especially as an alternative to $Hg_xCd_{1-x}Te$, has provided great incentive for the study of α-Sn-related thin films in recent years. Unfortunately, many problems exist in the preparation of these α-Sn_xGe_{1-x} alloys. Besides the well emphasized instability of α-Sn at temperature above 13.2°C, the mutual solid solubility between Sn and Ge is less than 1%.[32] Attempts to grow these metastable materials must therefore rely on non-equilibrium techniques such as MBE. The following is a brief account of some of the most important developments in the study of these materials.

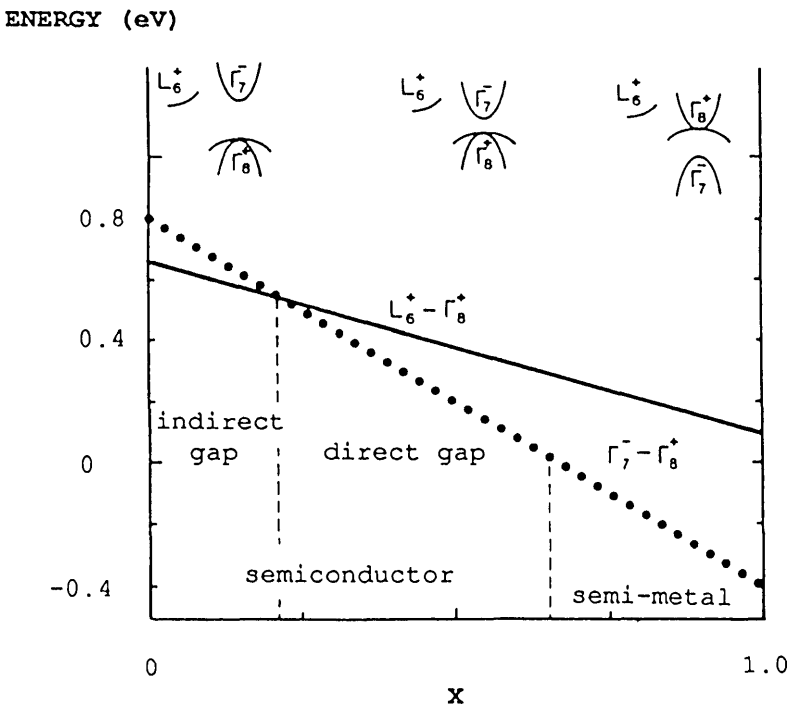


Fig. 2.5 Schematic illustration of the postulated band structure variation of α-Sn_xGe_{1-x} with alloy composition

2.3.1 Metastable α-Sn thin films

a) α-Sn on InSb

In 1981, Farrow *et. al.*[5] demonstrated that up to 0.5μm of α-Sn can be grown on InSb(001) substrates at 25°C. These films were found to be substrate-stabilized to about 70°C before transforming back to the β-phase (details of the substrate stabilization effect will be discussed in the next chapter). Since then, there have been several confirmatory investigations and even higher transition temperatures have been reported.[33,34] The α → β conversion in α-Sn grown on InSb(001) substrates was studied by Menéndez and Höchst using Raman scattering.[33] They suggested that the α-phase is stabilized by substrate interfacial bonds and the phase transition temperature of α-Sn films 600Å thick was found to be as high as 115°C. Structural studies of α-Sn films grown on InSb(001) substrates using reflection high energy electron diffraction (RHEED)[35,36] and low energy electron diffraction (LEED)[37] revealed a two-domain (2x1) reconstruction similar to that observed on Si(100) surfaces. Recently, we have observed two new reconstructions, namely p(2x2) and c(4x4), on our α-Sn films.[38] The structure of the film is found to undergo a thickness dependent change and a dimer model has been proposed (see chapter 6 for details).[38] The electronic band structure of α-Sn thin films has been determined by angle-resolved photoemission studies (ARUPS)[39,40] and found to agree well with theoretical calculations. Using core-level photoemission, the final valence band discontinuity at the α-Sn/InSb(100) heterojunction was found to be 0.40 ± 0.06eV,[36] in close agreement with the theoretical value calculated using Tersoff's model (0.33eV).[41] Evidence for some Sb segregation into the α-Sn films during the initial stages of interface formation were also revealed. This may be related to Satoh and Kimata's observation that the quality of α-Sn films grown on InSb(100) substrates at high temperatures (~75°C) was superior to that grown at lower temperatures.[34] Recently, there has been a surge of interest in the study of α-Sn films from AT&T Bell Labs. where triple-axis X-ray diffractometry was employed to determine the structural parameters and the strain distribution.[42] The study of the optical properties of α-Sn/InSb(100) samples has so far been limited to the measurement of the dielectric function using ellipsometry.[43] The reported results compared reasonably well with available band structure calculations.

Besides the (100) surface, there have also been attempts to grow α-Sn films on other InSb surfaces. Höchst and co-workers have conducted ARUPS and RHEED studies to investigate the growth mode and microscopic electronic structure of α-Sn(111) films grown on InSb(111) and $(\bar{1}\bar{1}\bar{1})$ surfaces.[44,45] They reported that bulk α-Sn(111) could only be grown up to a thickness of ~ 40MLs (~ 150Å), beyond which 3-D island growth started and the films showed a mixture of α and β phases. Only a bulk (1x1) reconstruction pattern was observed throughout the growth. In contrast, Kasukabe *et. al.*[46] have succeeded in growing up to 150MLs (~ 600Å) of α-Sn(111) on InSb$(\bar{1}\bar{1}\bar{1})$ substrates cleaned by heating in Sb_4 beams. The α-Sn surface showed a (3x3) reconstruction pattern. Our α-Sn/InSb$(\bar{1}\bar{1}\bar{1})$ films up to 1000Å thick were found to exhibit the same reconstruction.[47] In addition, we also observed a (3x1) pattern in thicker films. Epitaxial films as thick as 1500Å have been successfully grown with no detectable β-phase formation and magneto-transport measurements have been performed (detailed discussions can be found in § 7.3.3).[47] Relatively thin (300Å) α-Sn films have been deposited on the non-polar (110) surface of InSb by Menéndez and Höchst.[33] The quality of these films was found to be inferior to those grown on the (100) surface and no sharp α → β transition could be observed. RHEED experiments carried out during growth show weak diffraction spots indicating island growth. Recently, we have also grown α-Sn/InSb(110) layers with thicknesses up to 1000Å which exhibit clear diffraction streaks in the RHEED patterns (refer to § 5.4.1).

The growth of α-Sn films on InSb substrates is not limited to the use of the MBE technique. Islets of α-Sn epitaxially grown by liquid phase epitaxy (LPE) on InSb$(\bar{1}\bar{1}\bar{1})$ substrates were found to be stable to approximately 60°C although the morphology of the film as revealed by scanning electron microscopy (SEM) was quite poor.[48] Nevertheless, this indicates the extent to which the studies of α-Sn films have proceeded in recent years.

b) α-Sn on CdTe

In addition to InSb, CdTe substrates, which are also closely lattice-matched to α-Sn, have been used to stabilize α-Sn films. Whereas the study of the electrical properties of α-Sn films grown on InSb is hindered by multi-carrier conduction arising from the substrate, CdTe substrates are

available in high resistance form thereby making the interpretation of electrical data easier. On the other hand, the structural quality of α-Sn films grown on CdTe(100) was reported to be poorer than those grown on InSb(100) in terms of the narrowness of the full width half maxima (FWHM) of double crystal X-ray rocking (DCXR) curves and structures in X-ray topographs.[49]

The first α-Sn film grown on CdTe(001) substrates by Farrow *et. al.*[5] was reported to be p-type with a high donor concentration ($10^{19}cm^{-3}$) and low mobility (≤ 250 cm^2/Vs @ 77K). Takatani and Chung[50] have also grown α-Sn films up to 200Å on CdTe(111) substrates which were stable up to 80°C. From their HREELS (high resolution electron energy loss spectroscopy) results, they concluded that finite bandgaps in the range of 420 to 230 meV can exist in α-Sn layers ~ 50 to 80Å thick. Their results compare favourably with theoretical estimation of quantum size effects in α-Sn films which predicts the existence of a thickness dependent bandgap due to carrier confinement within the overlayers (see Fig. 2.4).[28]

Following their success in the study of bulk α-Sn during Ewald's era,[4] research groups in Northwestern University (USA) have continued to pursue the magneto-transport properties of α-Sn/CdTe(001) thin films in recent years.[6,51-54] Grown on a CdTe buffer layer, the electrical properties of their α-Sn layers are far superior to those reported by Farrow *et. al.*.[5] Thin films (less than ~ 400Å) were found to be p-type with carrier concentrations as high as $2x10^{19}$ cm^{-3} which they attributed to out-diffusion of the substrate elements. This is in contrast to ARUPS results from which Tang *et. al.*[29] found that the α-Sn/CdTe(100) interface is abrupt and non-reactive with no noticeable inter-diffusion nor segregation of Cd in the α-Sn layer. Films thicker than 400Å were found to be n-type with carrier densities as low as $2x10^{17}$ cm^{-3} (Hall measurements) and low temperature mobilities in excess of $10^4cm^2/Vs$.[6,51] Quantum size effects, manifested as a thickness dependent bandgap, was also observed.[52] Recently they reported the first observation of SdH oscillations in α-Sn/CdTe(001) heterostructures.[51] The SdH carrier concentration of a 1210Å film was found to be $2.3x10^{17}cm^{-3}$, which is in good agreement with the Hall data. The observed oscillations at oblique magnetic field angles were found to be increasingly two-dimensional in character as the film thickness decreased.[53] They ascribed these observations to the quantization of carrier motion in the direction normal

to film growth and the occupation of several subbands arising from quantum size-effects. A far infared study of cyclotron resonance (CR) and plasma-shifted CR was also carried out on these samples.[54] An effective mass of $m^* = (0.0333 \pm 0.0002)m_o$ and an estimated dielectric constant of $\varepsilon \approx 23$ were reported, in close accord with values for bulk α-Sn samples.[23] CR features and SdH oscillations involving many more subbands were also recorded in our α-Sn films grown on InSb(100) and $(\bar{1}\bar{1}\bar{1})$ substrates although a high carrier concentration two-dimensional electron gas (2DEG) is responsible in our case.[47,55]

Recently, Hoffman *et. al.*[56] reported detailed magneto-transport studies of α-Sn/CdTe(100) MBE layers using a three-band transport model (L_6 electrons, Γ_8 electrons, and Γ_8 holes). Electron transfer from the Γ_8 minimum to the L_6 valleys was studied and the L_6- Γ_8 energy gap was found to resemble closely the bulk value. The same group has also reported the observation of optical non-linearity at 10.6μm in their α-Sn samples.[7,57] Non-degenerate four-wave mixing experiments revealed a non-linear susceptibility $\chi^{(3)}$ comparable in magnitude to that observed in HgTe-CdTe superlattices.

The effect of growth conditions on the stability of α-Sn films grown on different surfaces of CdTe substrates was studied by Reno and Stephenson of Sandia National Lab., U.S.A..[58] They showed that the non-polar (110) surface is a better orientation than (100) and that CdTe$(\bar{1}\bar{1}\bar{1})$ is totally unacceptable for MBE growth of α-Sn films. Höchst *et. al.*[59] have conducted interface and growth studies of α-Sn/CdTe(110) superlattices (10 periods, each 50Å thick). Core-level photoemission spectra indicated both sides of the interface to be stable, non-reactive and abrupt for growth temperatures up to 100°C and a valence band offset of 1.1eV was obtained.

Up to date, the most sophisticated structure involving α-Sn has been produced by Satoh and Kimata.[34] CdTe/α-Sn/CdTe/InSb multilayer structures involving 15 periods of α-Sn/CdTe superlattices (30Å each) have been grown at ~ 170°C.

2.3.2. α-Sn_xGe_{1-x} alloys and α-Sn/Ge superlattices

In their pioneering work resulting in the first successful growth of

α-Sn films by MBE, Farrow *et. al.*[5] also grew samples with 1% Ge added. The resulting change in lattice parameter was measured using DCXR and found to obey Vegard's law. Thereafter, Paul's group have synthesized $Ge_{1-x}Sn_x$ alloys with $x \rightarrow 0.3$ using pulsed UV laser crystallization.[31] Their studies demonstrated the opening up of a direct bandgap varying from 0 to 0.5eV depending on x. Using multi-target sputter deposition, Greene and co-workers have successfully grown single crystal metastable $Ge_{1-x}Sn_x$ ($x \leq 0.08$) alloys on Ge(100) and GaSb(100) substrates.[60] Recently, they have extended their studies to $(GaSb)_{(1-x)}(Sn_2)_x$[61] and quaternary $(GaSb)_{1-x}(Ge_{2(1-y)}Sn_{2y})_x$[62] alloys grown on GaAs(100) substrates.

Single phase Sn_xGe_{1-x} alloys with $x \leq 0.3$ MBE grown on Si(100) have been reported by Pukite *et. al.*[63] at IBM. To provide a better lattice match, Ge buffer layers were grown prior to the deposition of the alloys. The critical thickness of the alloy film is limited to ~ 2000Å for x = 0.3 due to the onset of phase separation. At this composition, the optical bandgap is estimated to be 0.4 ± 0.1eV and the room temperature mobility is comparable to that of pure Ge films (≈ 1000 cm^2/Vs for $n \approx 5x10^{18}cm^{-3}$). On the other hand, Asom *et. al.*[64] of AT&T Bell Labs. have grown alloys of α-Sn_xGe_{1-x} with $0.01 < x < 0.1$ by MBE on InSb(100) substrates. Using RHEED, they observed a (2x1) reconstruction which deteriorated into a spotty pattern when the film thickness reached 1500Å. We also observed a (2x1) reconstruction pattern for our 1000Å α-$Sn_{0.02}Ge_{0.098}$ sample. The band structure and electronic properties of metastable α-Sn_xGe_{1-x} alloys have been extensively studied by Jenkins and Dow.[65]

Following their success with α-Sn films, Höchst's group have moved on to the studies of MBE grown α-Sn_xGe_{1-x} alloys and some of their results are summarized as follows :

a) Growth studies :[30,49]
   - CdTe(100) substrates are not suitable for the growth of homogeneous films with $x \geq 0.1$.
   - alloy films with good crystalline order can be grown with a thickness up to ~ 300Å at ~ 400°C on Ge(100) and preferential growth of an alloy with x ~ 0.5 (compositional pinning) is observed.

b) Angle-resolved photoemission spectroscopy (ARPES) studies of α-$Sn_{0.48}Ge_{0.52}$ on Ge(100) :[66]

- a shift of the Γ_8 valence band from ~ 0.6eV in Ge(100) to ~ 0.16eV below E_F in the alloy.
- a direct band gap of E_g ~ 0.2eV.

c) Magneto-transport measurement with a three-band transport model :[56]
(α-$Sn_{1-x}Ge_x$ on CdTe(100) with $x \leq 0.02$)
- the L_6- Γ_8 energy gap has a strong dependence on alloy composition which goes in the opposite direction from that expected on the basis of bulk properties due to lattice-mismatch-induced strain.

d) Magneto-optical studies (α-$Sn_{0.99}Ge_{0.01}$ on CdTe(100) with $x \leq 0.02$) :[56]
- observation of CR effective masses in the range of 0.0365 to 0.0372m_o.

e) Non-degenerate four-wave mixing experiments :[7,57]
(α-$Sn_{1-x}Ge_x$ on CdTe(100) with $x \leq 0.08$)
- large non-linear susceptibility $\chi^{(3)}$ observed at 10.6μm which varies with composition.

Recently, short-period α-Sn/Ge strained-layer superlattices (SLSs) lattice-matched to Ge(001) substrates have also been synthesized by MBE using a large modulation of substrate temperature during growth.[67] These SLSs, consisted of a sequence of alternating 2ML α-Sn and 20ML Ge, were found to be stable up to ~ 395°C. Pseudomorphic growth with good crystalline quality and little intermixing was revealed in high resolution lattice images. Distinct superlattice effects were also observed in the structural and phonon scattering properties of these samples.

2.3.3 α-Sn_xSi_{1-x} Alloys

Gallerneault *et. al.*[68] reported that Si is at least as effective as Ge in stabilizing α-Sn. Recently, Hanke *et. al.*[69] calculated the band structure of Si_n/Sn_m(001) short period superlattices using the empirical tight-binding method and treating the band-offsets and the location of the strain as parameters. They found that, depending on their detailed assumptions about these parameters, the superlattice could be a metal or a new zero bandgap semiconductor. However, doubts have been raised about the stability of the superlattice in the presence of a 20% lattice mismatch.[10]

CHAPTER 3 FUNDAMENTALS OF MOLECULAR BEAM EPITAXY

3.1 Introduction

Molecular beam epitaxy (MBE) is a highly controlled crystal growth technique involving molecular/atomic beams chemically reacting with or directly condensed onto a heated single crystal substrate in an ultra-high vacuum (UHV) environment. It is essentially a combination of two growth techniques that emerged in the 1960s :

(i) The "three-temperature" technique used by Günther[70] for the stoichiometric growth of polycrystalline III-V semiconductor films. In this method, separate elemental (group III and group V) sources maintained at different temperatures were used to provide the appropriate flux ratio at the substrate which is held at some third temperature. It was not until a decade later, however, that Davey and Pankey[71] demonstrated the epitaxial growth of single crystal GaAs using this method.

(ii) The molecular beam system used by Joyce and co-workers[72] to investigate the nucleation of homoepitaxial Si films produced by the pyrolysis of SiH_4. They also studied the influence of the substrate surface on nucleation and the subsequent behaviour of layer growth. At the same time, Arthur[73] was investigating the surface kinetics of the interaction of modulated Ga and As_2 beams with GaAs substrates which provided the basis for the understanding of the growth mechanism of this material.

These investigations led to the development of MBE as a practical thin film growth technique when Cho applied a similar technique to grow thin films for device application.[74]

In this chapter, the basic concepts underlying epitaxial growth will be outlined, giving special attention to the different growth modes identified experimentally. The principles of MBE and its differences from other epitaxial techniques will be discussed in § 3.3. Finally, special features concerning the growth of α-Sn on InSb substrates such as the concept of pseudomorphism, substrate-stabilization of the metastable α-phase and non-polar/polar epitaxy will be addressed.

3.2 Theories of Epitaxial Growth

Epitaxy refers to the formation of an overgrowth which is crystallographically related to the substrate.[75] By definition, epitaxy is a dynamic phenomenon and the roles of thermodynamics and kinetics are both important. Conventional theories of thin film growth have mostly been based on statistical thermodynamic formulations and kinetic rate equations. Weeks and Gilmer[76] have reviewed the general theory from a thermodynamic view point and verify some predictions of analytical theories based on the solid-on-solid (SOS) model using Monte-Carlo simulations. Later, Venables *et. al.*[77] reviewed the more atomistic nucleation theory based on kinetic rate equations and compared it with experimental results based on electron microscopy. These and other experimental studies on epitaxial growth have established three basic growth modes which are illustrated schematically in Fig. 3.1 :[77,78]

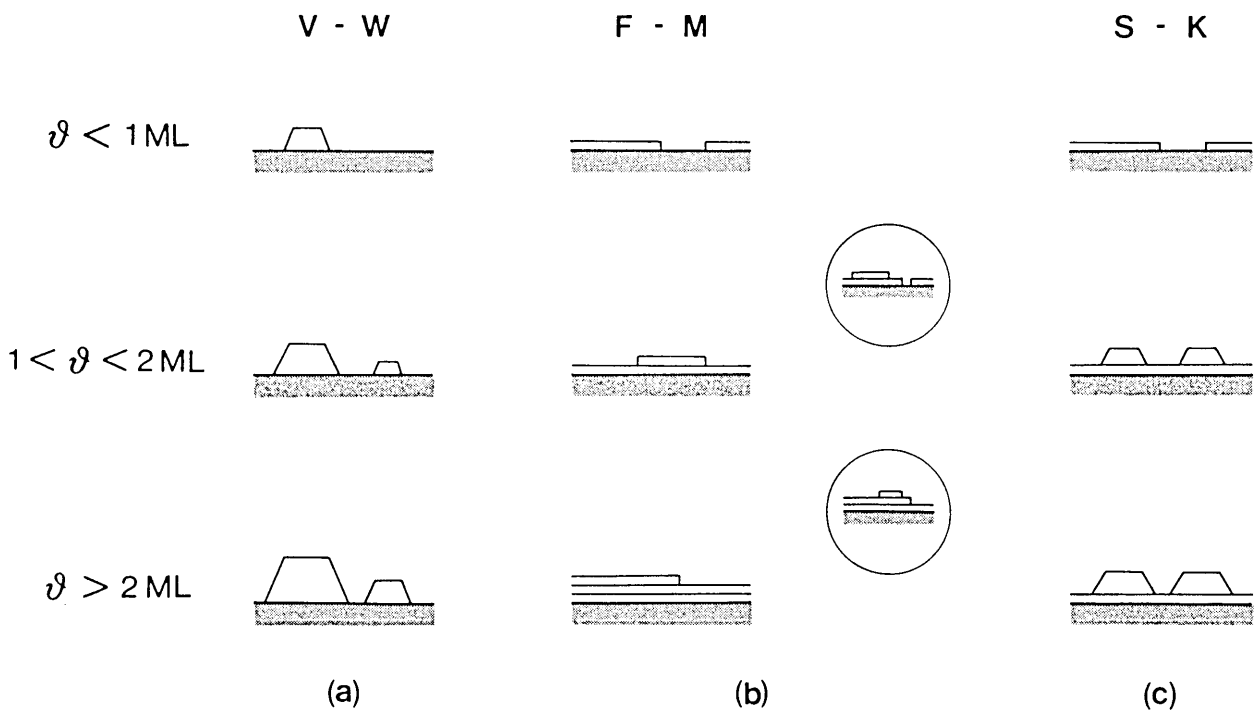


Fig. 3.1 Schematic illustrations of the three basic epitaxial growth mode

a) In the Volmer-Weber (V-M) or island growth mode (Fig 3.1a), initial deposit atoms aggregate as small 3-D islands which increase in size as further deposition continues until they touch and intergrow to form a continuous film. Such nucleation occurs when the binding between the deposit atoms is stronger than their binding to the substrate. The initial stages of MBE growth of InSb on GaAs(001) was found to proceed by this mode.[79]

b) The Frank-van der Merwe (F-M) or layer-by-layer growth mode (Fig. 3.1b) proceeds through 2-D nucleation because the deposited atoms are more strongly bound to the substrate than to each other. Deposit atoms aggregate to form monolayer islands which enlarge as deposition continues until a complete monolayer coverage has taken place. This layer is then covered with a somewhat less tightly bound second layer. Provided the binding energy of the newly arrived atoms with respect to the bulk value of the deposit is decreasing, layer-by-layer growth is maintained. The true F-M mode represents a somewhat idealized situation which is improbable though not impossible to achieved in practice. It is more likely, however, that a thickening layer grows in the form of "simultaneous multilayers"[78] whereby a new layer starts to grow before the completion of the layer underneath (see inset of Fig. 3.1b). Homoepitaxial growth of GaAs(001)[80] as well as Si(001)[81] were found to proceed in this way as evidenced from the damped oscillatory behaviour of the RHEED intensity observed during growth.

c) The Stranski-Krastanov (S-K) or layer plus island growth mode depicted in Fig. 3.1c is an intermediate case. After forming the first few monolayers, subsequent layer growth is unfavourable and islands are formed on top of these intermediate layers. This growth mode is commonly observed in heteroepitaxial systems with finite misfit since uniform films with thicknesses greater than several monolayers are reported to be unstable in such cases.[82]

In addition to these well-classified modes, growth can also proceed via the formation of steps and kinks on the growing surface due to thermodynamic fluctuations at high temperature and thereby circumventing the need for nucleation as suggested by Burton *et. al.*[83]

3.3 Basic Principles of Molecular Beam Epitaxy (MBE)

MBE is a versatile technique for growing thin epitaxial structures involving thermal molecular/atomic beams of the constituent elements chemically reacting with or directly condensing onto a substrate surface (usually maintained at an elevated temperature) in ultra-high vacuum. The use of the term "molecular" beam epitaxy is somewhat confusing as it does not refer to the chemical composition of the beam, but rather to the fact that the flow of components from the source to the substrate is in the molecular and not viscous flow regime as in metal-organic chemical vapour deposition (MOCVD).[84] The beams can thus be considered as unidirectional with negligible interaction between them. The composition of the grown overlayer and its doping level depends on the arrival rates of the constituent elements and dopants. For solid sources, the arrival rates depend on the evaporation rates of the appropriate sources. The growth rate employed in MBE (typically 1 μm/h or 1 monolayer/s) is low enough to enable surface migration of the impinging species on the growing surface. Simple mechanical shutters can be placed in front of the beam sources to interrupt the fluxes thereby allowing abrupt changes in composition and doping on an atomic scale. Details of the MBE system used in this work will be described in chapter 5 and reviews of the MBE process can be found in a number of articles[74,85,86] and books.[84,87,88]

What distinguishes MBE from other vacuum deposition techniques is its significantly more precise control of the beam fluxes and growth conditions. Employing vacuum deposition, MBE growth is carried out under conditions far from thermodynamic equilibrium and is governed mainly by the kinetics of the surface processes occurring when the impinging beams react with the outermost atomic layers of the substrate crystal.[88] This is in contrast to other epitaxial growth techniques, such as liquid phase epitaxy (LPE) which proceed at conditions near thermodynamic equilibrium or vapour phase epitaxy (VPE) which is most often transport (both mass and heat) limited.[88] This is particularly important for α-Sn related materials since epilayers containing metastable phases can only be grown (e.g. α-Sn_xGe_{1-x} alloys) by non-equilibrium techniques such as MBE.[89]

In comparison to all other epitaxial growth techniques, MBE has a unique advantage. Being realized in an ultra-high vacuum environment, it may

be monitored *in-situ* by surface sensitive diagnostic methods such as reflection high energy electron diffraction (RHEED), Auger electron spectroscopy (AES), photoemission spectroscopy (PES) or low energy electron diffraction (LEED) etc..[88] These facilities allow the chemical and structural properties of the epilayer to be monitored throughout the growth process. Much of the guesswork involved in crystal growth can thus be eliminated and the growth conditions optimized to enable the fabrication of sophisticated device structures. The first two methods, namely RHEED and AES, have been used extensively for the growth studies of α-Sn in this work.

Because of the lack of involvement of kinetics in the predominantly thermodynamic approach in their formulation, conventional theories concerning epitaxy seem to be ill-equipped for describing the MBE process. To address this problem, Madhukar and co-workers performed Monte-Carlo simulations of MBE (mainly GaAs growth) with the inclusion of relevant kinetic and growth parameters.[89] Based on the concept of localized equilibrium between the substrate and the growing film, the role of kinetic parameters such as sticking coefficient, surface migration and evaporation rate was discussed in details.

To date, most effort on growth simulations has been directed towards III-V compound semiconductors and group IV materials have received comparatively little attention despite the reduced complexity due to the involvement of only one species. However, recent developments in the integration of III-V opto-electronic devices with elemental semiconductors, in particular GaAs on Si,[90] have stimulated interest in the theoretical studies of homo- and heteroepitaxy of group IV semiconductors. In their Monte-Carlo simulation of Si(001) growth by MBE, Barnett and Rockett modified the SOS model to account for the diamond structure.[91] Surface reconstruction was also included by allowing dimer formation to occur on the surface. Their results indicate that surface dimers play an important role in determining the crystal growth kinetics, which is a combination of step propagation and two-dimensional island nucleation. Accounting for the subsurface strain energy interaction between dimers, dimer pairs forming ordered (2x1) domains with a small percentage of c(4x2) domains were observed in the simulated growth surface (note that Barnett and Rockett labelled the c(4x2) domains as c(2x2), treating one dimer pair as a single unit). The co-existence of these structures was confirmed by scanning

tunneling microscopy results.[92] For the case of low temperature Si growth, Clarke and Vvedensky[93] introduced a surface incorporation mechanism into the SOS model, with which they were able to reproduce the layer by layer growth mode manifested experimentally by the presence of monolayer RHEED oscillations at temperatures too low to promote significant surface adatom mobility, previously believed to be the driving mechanism of the layer-by-layer growth mode in MBE.[94] Clarke *et. al.*[95] extended this model by explicitly including a surface anisotropy in interatomic bonding with respect to the direction of the dimers and a finite ranged incorporation mechanism. They were able to account for the observation of a bilayer period in the intensity oscillations of the RHEED specular spot due to the alternation of (2x1) and (1x2) reconstructions in progressive monolayers on pre-annealed Si(001) surfaces.[81] The origin of the azimuthal dependence of these bilayer oscillations and the need for pre-annealed surfaces was also discussed.

Besides the Si(001) surface, these models are also applicable for studies of the Ge(001) surface.[91] On the other hand, the study of the α-Sn/InSb system is still in its infancy and to date there have been no reports of theoretical growth studies of this novel material. Inevitably, the growth mechanism of α-Sn on InSb(100) will be different from the homoepitaxy of Si(100) due to the non-polar/polar interface. Nevertheless, the similarity of the (100) surface structure between Si and α-Sn such as the co-existence of (2x1) and c(4x2) domains and the alternating (2x1) $\leftrightarrow$ (1x2) reconstructions (see chapter 6 for details) offers the possibility of modifying the Si(100) models for the study of the α-Sn/InSb(100) surface.

3.4 Pseudomorphic Growth and Stabilization of Metastable Phases

Pseudomorphic growth is characterized by the imposition of the in-plane crystal structure and lattice dimensions of the substrate on the overlayer growing upon it with a corresponding distortion in the orthogonal lattice parameters of the overlayer perpendicular to the interface.[96] The idea of pseudomorphic growth is introduced by Frank and van der Merwe following their studies of the layer-by-layer growth mode.[97] They suggested that the lowest energy state of a growing monolayer would be one matching in spacing with the substrate surface plane provided the natural misfit is less than

some limiting value. The misfit f is normally defined as :[98]

$$f = \frac{a_o - a_s}{a_s} \tag{3.1}$$

where a_o and a_s are the stress-free lattice parameters of the overlayer and the substrates respectively. They predicted that any epitaxial layer having less than 9% misfit with the substrate would initially grow pseudomorphically, i.e. for very thin layers the deposit would be elastically strained to have the same interatomic spacing as the substrate, forming a coherent interface.[97] At sufficiently low temperature, a larger misfit (up to 14%) can also be accommodated with the overlayer metastably deposited in exact fit on the substrate.[97]

Later, Jesser and Kuhlman-Wilsdorf[98] modelled the phenomenon of coherent growth for the case of a cubic deposit on a cubic substrate crystal (Fig. 3.2). In their model, the interfacial energy is controlled by the energy of the interfacial dislocations. If the film is elastically strained to accommodate the lattice mismatch (Fig. 3.2b), the interfacial energy is reduced at the expense of the strain energy stored in the film. The equilibrium elastic strain in the film is that which minimizes the total energy of the bicrystal system, i.e. the sum of the interfacial energy and stored elastic strain energy. For sufficiently thin films, they showed that the total energy is minimized when the film is strained to accommodate the lattice mismatch completely. For thicker films however, misfit dislocations will be generated to relieve part of the misfit (Fig. 3.2a). The critical thickness h_c, beyond which it becomes energetically favourable for dislocation formation was calculated to be :[98,99]

$$h_c = \frac{G_s\, b^2}{2\pi a_s |f| (1+2\upsilon)(G_o + G_s)} \ln\left(\frac{(G_o + G_s)\, G_i (1-\upsilon)}{2\pi\, G_o G_s |f|}\right) \tag{3.2}$$

where G_i, G_o and G_s are the shear moduli of the interface, overgrowth and substrate, a_s the lattice constant of the substrate, b the magnitude of the Burgers vector and υ the Poisson's ratio. For semi-quantitative estimates, this rather formidable equation can be simplified to :[99]

$$h_c = \frac{b}{2\,|f|} \tag{3.3}$$

Since b is always of the order of the unit cell dimension, Eqn. 3.3 can thus be interpreted to mean that the overlayer will be pseudomorphic until the

accumulated misfit ($h_c|f|$) exceeds about half of the unstrained unit cell dimension (~ b/2).[99]

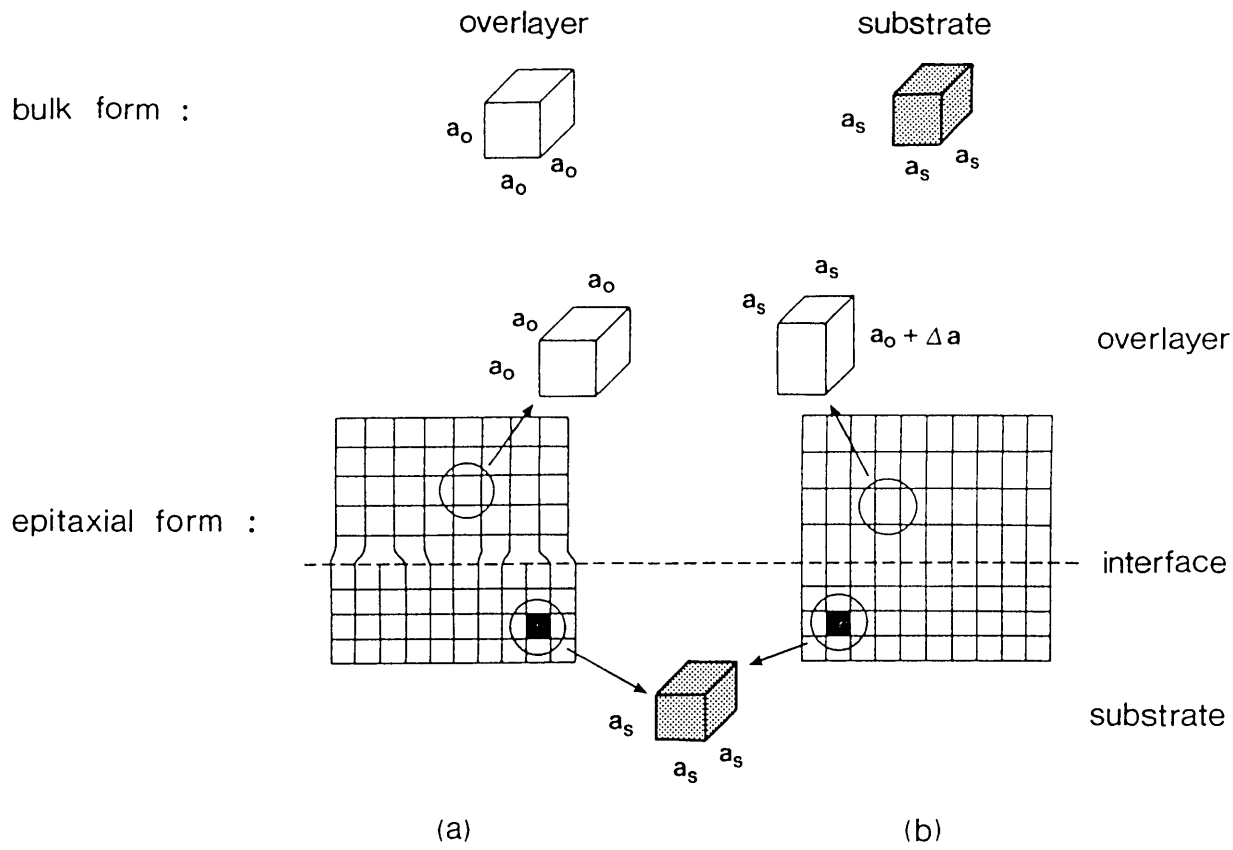


Fig. 3.2 · Schematic diagrams of the interface between a cubic substrate and cubic epitaxial film illustrating the difference between heteroepitaxial growth with lattice misfit accommodated by (a) interfacial misfit dislocations and (b) elastic strain in the film.

The concept of stabilizing metastable phases by epitaxy has its origin in the studies of coherent and pseudomorphic growth of metals on single crystal metal surfaces during the 1950s and 1960s. Jesser and Matthews[100] reported the first demonstration of the stabilization of a metastable (allotropic) phase of Fe by epitaxy and provided convincing evidence that the substrates can control the crystal structure of thin overlayers. They found that room temperature deposition of Fe on the (001) surface of Cu in ultrahigh vacuum resulted in 2-D pseudomorphic growth of γ-Fe. This is remarkable since the γ-phase of Fe is only thermodynamically stable within the limited temperature range of 916-1400°C. In thicker films (≥ 20Å),

misfit dislocation and α-Fe nuclei were observed indicating the onset of the relaxation of the metastable phase to its thermodynamically stable phase (i.e. α-Fe) by the generation of local disorder.

The observation of this substrate-stabilization phenomenon has opened up prospects for the preparation of a variety of interesting and potentially useful metastable materials such as α-Sn by a similar technique. Indeed, substrate-stabilized α-Sn epilayers have been successfully grown on both InSb(100) and CdTe(100) surfaces[5] (at 25°C, the lattice constants for bulk α-Sn, InSb and CdTe are 6.489Å, 6.479Å and 6.4829Å respectively).[5, 42] In both cases, the lattice mismatch is small enough (~ 0.14% and 0.094% respectively) to enable pseudomorphic growth for films less than 0.5 μm thick. Since there are no reliable elastic modulus data for α-Sn thin films, the critical thickness cannot be calculated accurately using Eqn. 3.2. From the simplified expression of Eqn. 3.3, the lower limit of h_c is estimated to be ~ 0.25μm. Experimentally, Asom *et. al.*[42] reported that unrelaxed α-Sn layers up to 1μm thick can be pseudomorphically grown on InSb(100) substrates. They postulated that the dislocation formation was kinetically inhibited due to the low growth temperature (< 30°C).

3.5 Heteroepitaxial and Non-polar on Polar Growth

The growth of high quality abrupt heterojunctions using MBE has already been well demonstrated with certain material systems during the past decade.[88] The most intriguing feature of these structures is the carrier confinement at the interface resulting from energy band discontinuities and the associated space charge fields between the two semiconductors. The motion of charge carriers normal to the plane of the heterojunction is thus quantized into 2-D discrete energy subbands and the mobility of these carriers can be very high. The interfacial properties of lattice-matched non-polar/polar heterostructures formed between elemental group IV and III-V compound semiconductors are particularly interesting because : i) The occurrence of the quantum effect requires extreme crystallographic perfection at the interface and is most frequently observed in lattice-matched systems, ii) The {100} and {111} interfaces contain both polar and non-polar bonds whereas only the latter is present at the {110} interface[101] (see Fig. 3.3), and iii) The interfacial and carrier confinement properties of these heterojunction can be used in device

design.[102]

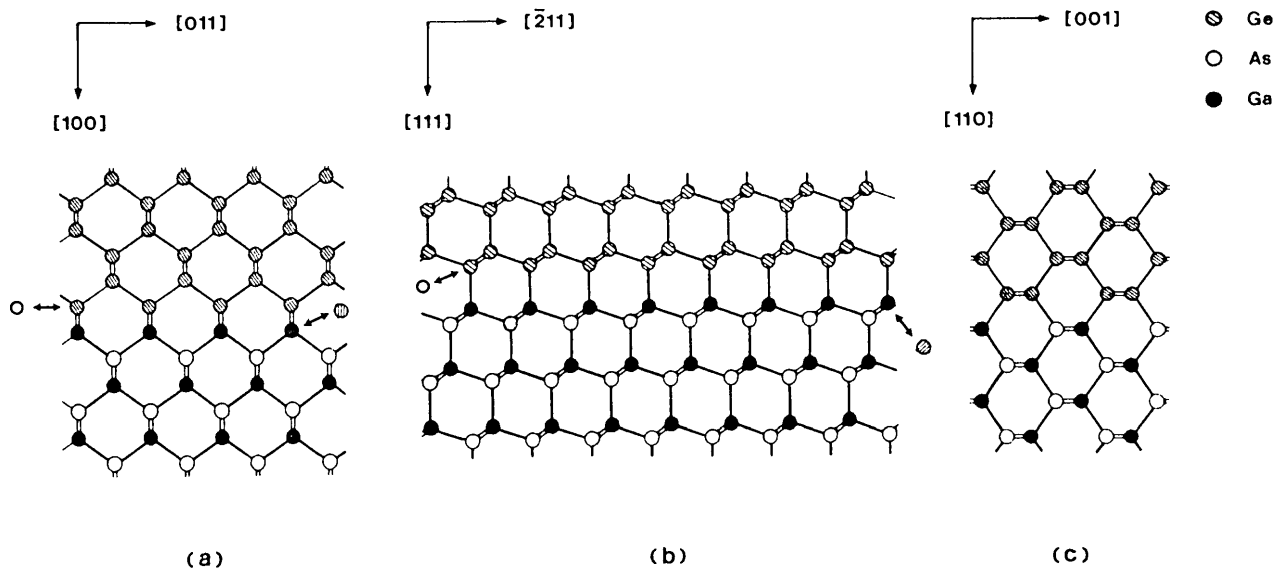


Fig. 3.3 Atomic arrangements at the interfaces of three heterostructures having different orientations

The Ge/GaAs(100) system, a prototype of such lattice-matched non-polar/polar heterostructures, has been extensively studied in recent years.[101-103] There were indications that a planar atomic configuration composed of unbroken bulk planes at the non-polar/polar Ge/GaAs(100) and (111) interfaces is highly unfavourable energetically. This interfacial instability arises from the problems of electrical neutralization at the polar interface.[101] It has been suggested that one way in which the interface can minimize the electrostatic energy involved is by reconstruction in order to neutralize the interface dipole,[101,104] i.e. the group IV atoms will bond with group III atoms as well as group V atoms forming a highly disordered and electrically compensated interfacial region extending over several transition layers. The resulting atomic rearrangement at the polar interfaces suggested by Harrison *et. al.*[101] is shown by arrows in Fig. 3.3a and b. It must be noted that due to the use of elevated growth

temperatures (~ 300°C),[102] which may enhance certain kinds of atomic dynamics such as inter-diffusion, the exact mechanism controlling the energetics of the interfacial reconstruction cannot be unambiguously defined in this system. An exchange reaction resulting in the formation of a GeAs-like compound[103] may further complicate the interface region. The isoelectric α-Sn/InSb system can, however, be grown at room temperature[42,47,55] and neither SnAs nor InSn compounds have been identified, suggesting this system may be more suitable for the study of heterojunction properties. Inevitably, an electrically compensated interfacial region will also be present in this system due to the non-polar/polar heterojunction, but the observation of a two-dimensional electron gas (2DEG) at the interface of the α-Sn/InSb system[47,55] and not at that of Ge/GaAs seems to indicate that the interfacial structure in the former system is more abrupt and well-defined. On the other hand, the problem with inter-diffusion still cannot be ruled out totally. A 1% diffusion of atoms over one monolayer (or 10^{-4} atoms over 1 Å) either way would produce the observed density of ~ 10^{12} cm^{-2} for the 2DEG.

CHAPTER 4 SUBSTRATE PREPARATION

4.1 Introduction

It is well known that proper substrate preparation, yielding a smooth, stoichiometric and atomically clean surface, is an essential prerequisite for the growth of high quality films by molecular beam epitaxy.[105] Any defect or dislocation present in the substrate may replicate itself or propagate onto the overlayers and degrade them. Using several X-ray diffraction techniques, Bowman *et. al.*[49,106] demonstrated that the quality and homogeneity of their α-Sn and α-$Sn_{1-x}Ge_x$ metastable epilayers depend strongly on the structural perfection of the substrates. Substrate quality is particularly important for the growth of α-Sn since it has been reported that the α to β phase transition always originates from defects or dislocation sites.[5] Similar results have also been observed in our samples and will be discussed in chapter 5.

The growth and subsequent removal of native oxides has proven to be the most successful method for cleaning Si and GaAs substrates for MBE work.[107] A thin oxide film is formed on the substrate surface by chemical etching which is then removed *in-situ* under vacuum prior to growth. When the same approach is used for the preparation of InSb substrates some difficulties arise : i) While many chemical etchants have been used, none of them seems to be satisfactory. It has been pointed out by Henneke[108] that some of these etchants can lead to non-stoichiometric surfaces. In some cases, surface roughenings have also been observed in the etched surfaces.[109,110] ii) Unlike GaAs where the oxide layers formed from chemical etching can be readily desorbed thermally, it has not proved possible to prepare passivating layers for InSb substrates which can be as easily removed and are at the same time resistant to atmospheric contamination. Some oxides (depending on the particular etchant used) formed on InSb surfaces do not evaporate even up to a temperature where the substrates start to decompose. In addition, thermal desorption is found to be inefficient in removing high concentration of carbon contaminants.[111,112] iii) While the alternative *in-situ* cleaning method i.e. the cyclic process of ion bombardment followed by annealing is very effective in the removal of active contaminants such as oxygen and carbon, it is well known that In droplets can be formed due to

preferential sputtering.[40,113] This technique also has the disadvantage of causing crystallographic damage[114] and can even produce a slightly conducting surface layer.[111,115]

In view of these difficulties, several chemical etchants and *in-situ* cleaning procedures were studied in order to find an appropriate and reproducible cleaning process for InSb substrates prior to MBE growth. Morphological analyses of the treated surface were performed by Nomarski microscopy and RHEED while surface atomic compositions were determined by X-ray photoemission spectroscopy (XPS) and Auger electron spectroscopy (AES). In this chapter, the main results from these studies are presented and the pros and cons of each cleaning method are discussed. Finally an optimum cleaning procedure for preparing InSb substrates prior to MBE growth of α-Sn is proposed.

4.2 Ex-situ Cleaning

4.2.1 Chemical etching

InSb(100) substrates as received from MCP Ltd. have been mechanically polished to a mirror finish. They are covered with petroleum jelly for protection during transit which has to be removed chemically. A typical degreasing procedure is outlined below :

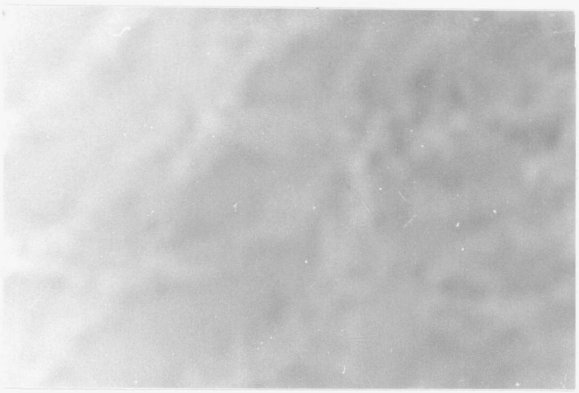
1) Boil in Trichloroethyne twice, each for 3 mins.
2) Boil in Acetone for 3 mins.
3) Boil in Methanol for 3 mins.
4) Boil in Propanol for 3 mins.
5) Blow dry with filtered nitrogen gas

Prior to loading into the system, the substrates were chemically etched to remove surface defects and passivate their surfaces from atmospheric contamination. In this study, various etchants commonly used for preparing InSb substrates were compared. Since most of these etching processes are diffusion controlled,[109] it is desirable to rotate the substrate uniformly in the etchant. A rotatable holder has been designed and was used for all subsequent etching. Only analytical grade quality chemicals were used in all substrate cleaning processes.

A mixture of lactic acid : HF : HNO_3 is one of the most widely used etchants for the preparation of InSb substrates. Both Noreika *et. al.*[116] and Ashley *et. al.*[117] have used it in the proportion of 25:4:1 for the subsequent homoepitaxial growth of InSb(100). The substrate surface so prepared is found to exhibit undulations when observed under a Nomarski microscope as shown in Fig. 4.1. These artefacts have prompted us to seek for an alternative etchant and several recipes have been tried.

Bromine-Methanol (Br_2- MeOH) etchants with varying Br_2 concentrations have been used by several workers to prepare InSb substrates.[110,118-120] When tested, etchants containing low concentration of Br_2 (0.05 - 0.4%) did not cause significant reduction in substrate defect density. On the other hand, higher bromine concentrations (0.4 - 1.0%) were found to produce 'orange peel-like' surfaces[110] (Fig. 4.2). In their preparation of InSb(110) substrates for homoepitaxial growth, Bosch *et. al.*[110] used HCl : Ethanol (1 : 10) to strip off the native oxide before etching with 0.2% Br_2- MeOH. However, no observable improvement on the surface morphology could be found using this treatment.

The process of chemically polishing InSb has also been investigated by Luft *et. al.*[109] They claimed that etchants containing H_2O_2 : HF : lactic acid in the proportion range of 30-60% : 20-70% : 2-20% by volume will give a surface roughness of less than 0.02 μm. Various compositions within this prescribed range have been tried, all of them resulting in ripples on the surface similar to those shown in Fig. 4.1. Apparently, the highly viscous lactic acid is not a very suitable reagent for dissolving InSb oxidation reaction products. CH_3COOH (acetic acid) with a lower viscosity was tried instead. In addition, large amount of gas bubbles were observed when the substrate was etched using Luft's original recipe,[109] suggesting that the etch rate might have been too fast. The oxidizing agent was thus changed from H_2O_2 to HNO_3 and the whole solution was diluted by de-ionized (DI) water. Various concentrations have been tried and a solution of HNO_3 : CH_3COOH : HF : DI H_2O in the proportion of 2:1:1:10 was found to provide the most satisfactory surface finish. This recipe is actually a modification of the CP4A etchant (HNO_3: CH_3COOH : HF @ 5 : 3 : 3) used for the study of the mechanical properties of InSb.[121] Using this etchant, InSb substrate with mirror finish and low surface defect density can be obtained as demonstrated by the Nomarski micrograph shown in Fig. 4.3.



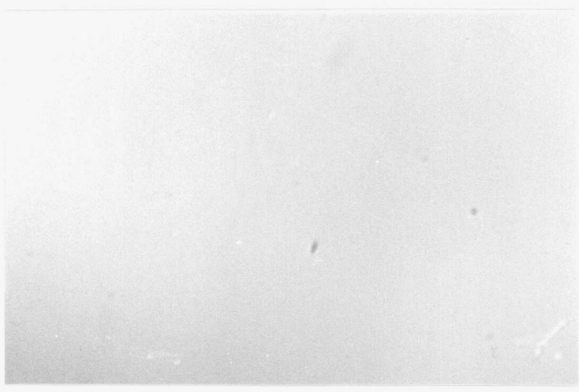
200μm

Fig. 4.1 Undulations observed on InSb(100) surface etched by lactic acid : HF : HNO_3 @ 25 : 4 : 1



10μm

Fig. 4.2 Orange peel-like features observed on InSb(100) surface etched by 0.4% Br_2 - MeOH



10μm

Fig. 4.3 Smooth InSb(100) surface etched by the modified CP4A etchant

Besides good surface morphology, the cleaning procedure should aim to produce a substrate surface that is free from carbon contaminants. It has been reported that residual carbon can cause surface roughening as well as affecting the electrical characteristics of MBE grown GaAs films.[122] One possible source of carbon contamination has been identified to arise from atmospheric CO_2 being absorbed by the water film left on the substrate surface.[122,123] Except for Br_2- MeOH where the freshly etched substrates are rinsed in methanol, it is common practice to give the substrate a thorough rinse in DI water before it is dried, making it susceptible to carbon contamination. It is therefore important to minimize the time that the wet substrate is exposed to the atmosphere. One solution is to boil the substrate in propanol (which is much more volatile than water) immediately after the DI water rinse prior to drying. This procedure has been used throughout this study. Both AES and XPS studies showed that all of the etching procedures tested produced approximately the same residual carbon level which was low enough to be readily removed by *in-situ* cleaning (see § 4.3.2 for details).

4.2.2 Study of oxide composition by XPS

Another criterion for choosing a suitable etchant for InSb is that the passivating oxide formed should be readily desorbed *in-situ*. This depends very much on the composition of the oxide formed since different etchants are known to produce passivating layers with different In to Sb oxide ratios.[108,112,124] Three etchants producing acceptable surface finishes were tested and the detailed treatments are listed in Table 4.1. In addition, an oxide layer formed by anodization commonly employed in InSb MOS technology[125] was also studied. This sample was anodically oxidized using a KOH electrolyte and possessed a characteristic bluish appearance. The effect of *ex-situ* treatments on the composition of the oxide layers and the ease of removing them were investigated by X-ray photoelectron spectroscopy (XPS).

TABLE 4.1

Sample 1	HNO_3 : HF_2 : CH_3COOH : H_2O @ 2 : 1 : 1 : 10 (modified CP4A)
	1. Degrease* 2. Dip in etchant for 2 mins. 3. Rinse in DI-H_2O for 3 mins. 4. Boil in MeOH for 3 mins. 5. Blow dry with filtered nitrogen
Sample 2	0.4% Br_2 - MeOH
	1. Degrease* 2. Dip in etchant for 10 sec. 3. Rinse in MeOH for 2 mins. 4. Boil in MeOH for 3 mins. 5. Blow dry with filtered nitrogen
Sample 3	HCl - EtOH + Br_2 - MeOH
	1. Degrease* 2. Etch in HCl - EtOH @ 1:20 for 10 sec. 3. Rinse in DI-H_2O for 3 mins. 4. Boil in MeOH for 3 mins. 5. Dip in cold MeOH for 1 min. 6. Etch in 0.4% Br_2 - MeOH for 10 secs. 7. Rinse in MeOH for 2 mins. 8. Boil in MeOH for 3 mins. 9. Blow dry with filtered nitrogen
Sample 4	Anodization by KOH
	1. Degrease* 2. Anodize using a KOH electrolyte 3. Rinse in DI-H_2O for 3 mins. 4. Blow dry with filtered nitrogen

* details of the degreasing procedures are listed in § 4.2.1

a) Theoretical background

The basis of photoelectron spectroscopy involves exposing a specimen to a flux of nearly monoenergetic radiation with mean energy $h\upsilon$, and observing the resultant emission of photoelectrons with kinetic energies described by the photoelectric equation :[126]

$$E_k = h\upsilon - E_b - \Psi \qquad (4.1)$$

where E_k is the kinetic energy of the photoelectron, Ψ the work function of the solid and E_b the binding energy of the electron in the solid relative to the Fermi level.

A photoelectron spectrum is an energy distribution curve of counts of electrons (proportional to the photoelectron current) per energy increment against binding energy (BE). The energy distribution of these photoelectrons has a one-to-one correspondence with the initial state energy distribution and hence mirrors the electronic structure of the analyzed material.

The technique of XPS utilizes X-ray radiation to stimulate emission. Photon sources most commonly used in these studies are the Al or Mg Kα lines, both of which are energetic enough to excite the core levels of most atoms. Since these core levels representing filled subshells have well defined binding energies, the peaks in XPS spectra are characteristic of individual elements and are well tabulated. Element identification can thus be accomplished by locating the core levels and comparing them with reference data. Because of the ability of XPS to identify elements, this technique is also referred to as ESCA (electron spectroscopy for chemical analysis).

Surface sensitivity in XPS is due to the short escape depth of photoelectrons. Depending upon the material and the ionization energy, the mean depth for emission ranges from 3 to 10 atomic layers and the observation of photoelectrons intrinsically emphasizes the surface contribution.[126,127] In the following studies where Alkα radiation (1486.6 eV) is used to probe the 3d transitions, the electron escape depth is approximately 6 - 7 atomic layers.

When comparing ESCA lines from the same element in different

surroundings, shifts in peak positions can often be observed which are caused by the rearrangement of the average charge distribution of the valence electrons.[128] In principle, each set of chemically inequivalent atoms will give a distinct core binding energy in the ESCA spectrum. The chemical shift is generally towards higher binding energy with increasing oxidation state. An oxidation process corresponds to a partial decrease of valence electron density at the oxidized atom which in turn decreases the shielding of the remaining atomic electrons (including core electrons), yielding an increase in E_b.[128] Differences in the chemical shifts from species of equivalent oxidation state are usually correlated with the electronegativity of the ligands. In this study, chemical shifts are used to detect the presence of oxide layers on the substrate surfaces. The identity of the oxides can also be determined by comparing the observed chemical shifts with the literature values for standard oxides. It should be noted that several other effects, primarily related to complexities in the final state of photoemission (e.g. relaxation phenomena, many electron interactions etc.), can also affect the observed chemical shifts although they will not be considered here. A comprehensive discussion on the interpretation of chemical shifts can be found in Ref. 129.

b) Experimental Details

X-ray electron spectroscopic experiments were conducted in a ESCALAB Mark II system (VG Scientific), courtesy of Dr. R. D. Egdell and the Chemistry Department, ICSTM. This system is equipped with a twin anode X-ray source and a concentric hemispheric analyzer (CHA). Noise arising from Bremsstrahlung and stray electrons is minimized by placing a thin Al window between the X-ray source and the sample. A coaxial RF feedthrough (Leybold Heraus Ltd.) fitted inside the introduction chamber provides heating for thermal desorption and annealing purposes.

Samples are secured by tantalum foils which are folded at the corners and spot-welded onto Mo holder stubs. These stubs can be manipulated inside the system by means of wobble sticks. Once introduced inside the ESCALAB through the fast entry loadlock, the substrates are heated to about 200°C for an hour in the preparation chamber. This initial outgassing procedure is required to desorb water vapour and other volatile contaminants from the substrate surface prior to analysis.

All data acquisition, storage and processing which includes signal averaging, background subtraction, spectral deconvolution and curve fitting etc. are accomplished using an Apple II microcomputer and supporting software.

XPS spectra arising from the 3d transitions in In and Sb were obtained by running the $Alk\alpha_{1,2}$ source ($h\upsilon$ = 1486.6 eV)[126,129] at a potential of 10 keV with 10mA emission current. During analysis, the base pressure of the system was kept below 10^{-9} Torr. The constant analyzer energy (CAE) mode which maintains a fixed resolution at all kinetic energies was used throughout this work. A pass energy of 10eV representing a compromise between resolution and signal to noise ratio was selected for all the runs. To take into account charging effects and work function differences between the sample and the analyzer, binding energies for the transitions have to be calibrated. This is achieved by referencing to the C1s line (assuming a binding energy of 285.0 eV) from carbon contaminants adsorbed on the sample surface.[128,130]

It must be stressed that due to the fairly low resolution of the ESCALAB (± 0.5 to 0.75 eV accuracy), all XPS peaks recorded are composite. They represent a convolution of many different states such as surface and bulk core levels and transitions arising from different chemical environment experienced by the element. In the following studies, chemical shifts rather than absolute binding energies are preferentially used to identify the chemical species.

c) Reference Spectra

Samples made from pure In wires (6N, MCP Ltd.) and Sb shots (6N, MCP Ltd.) were used for the determination of pure elemental oxide composition. Thermal oxides (InO_x and SbO_x) were formed by heating these samples in an oxygen atmosphere in the introduction chamber. An argon-ion-cleaned InSb sample was also included for reference. XPS spectra, corrected by smoothing and subtracting the appropriate linear background from experimental curves recorded during progressive oxide removal by thermal desorption, are shown in Figs. 4.4 - 4.6. Also shown in these spectra are the 3d transitions of Sb and In in the argon-ion-cleaned InSb sample (free from carbon and oxygen) for comparison.

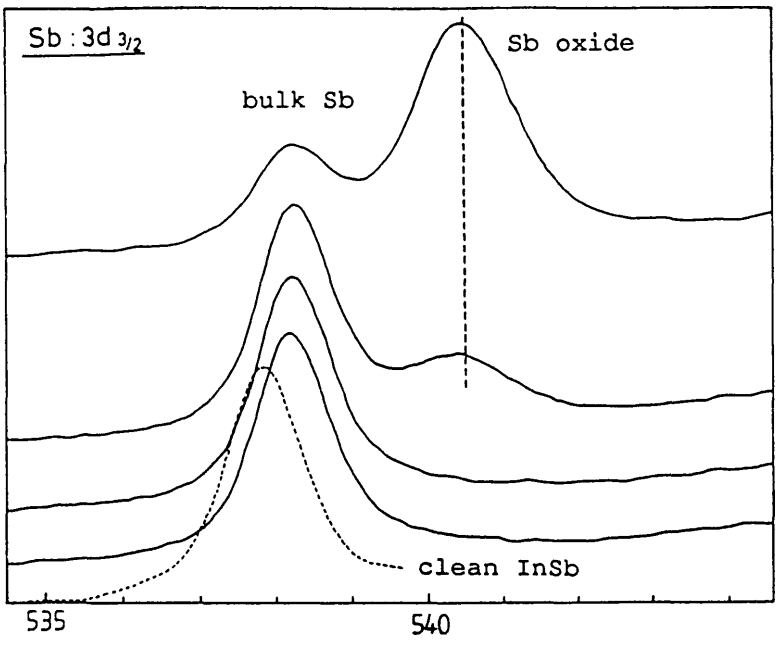


Fig. 4.4 $Sb3d_{3/2}$ spectra

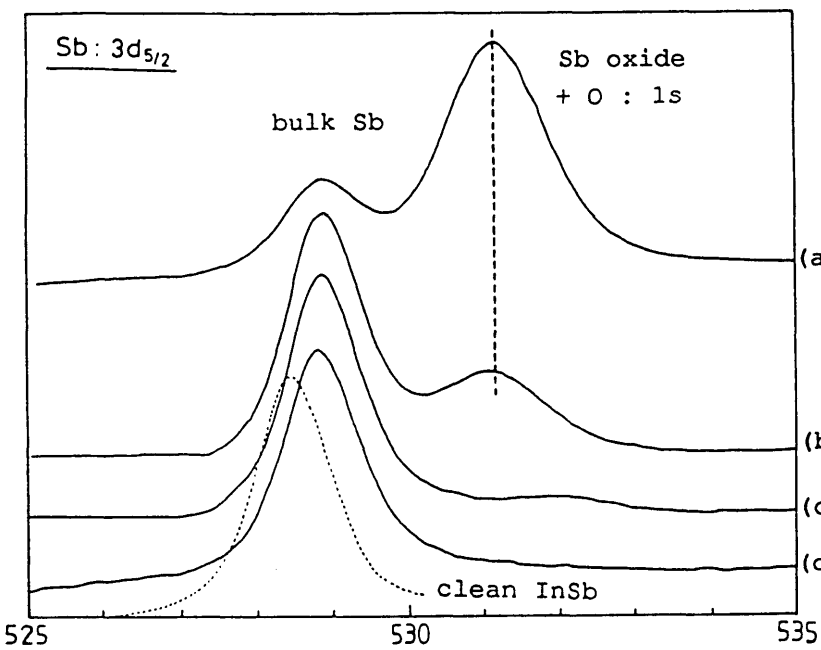


Fig. 4.5 $Sb3d_{5/2}$ spectra

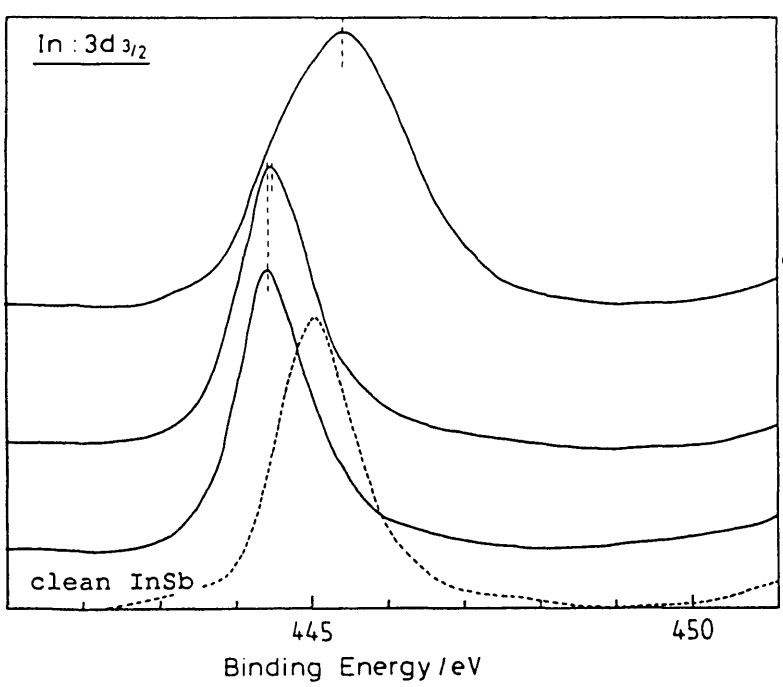


Fig. 4.6 $In3d_{3/2}$ spectra

Figs. 4.4 - 4.6 XPS spectra showing the progressive removal of oxides by thermal desorption

The 3d transitions are split into $3d_{3/2}$ and $3d_{5/2}$ peaks because of spin-orbit interaction although the $In3d_{3/2}$ peak is not shown here. The spin-orbit separation for the Sb3d transitions was measured to be 9.40 ± 0.5 eV which is consistent with that obtained by Copperthwaite *et. al.*.[131] Composite peak structures are clearly visible in the Sb3d spectra of the freshly prepared SbO_x sample (Figs. 4.4a and 4.5a). The low energy peaks (537.6 and 528.0 eV) belong to bulk Sb while the larger doublets at higher B.E. correspond to oxidized Sb species. In both transitions, chemical shifts of 2.3 ± 0.5eV were observed between the doublets. A further complication occurs in the $Sb3d_{5/2}$ case due to the proximity of the Sb oxide peak and the O1s line. These two peaks cannot be resolved in our XPS spectrum and the high energy doublet (@ ~ 530.3 ± 0.5eV) has to be treated as a superposition of these two peaks. On the other hand, the $In3d_{5/2}$ peak (Fig. 4.6a) appears singular but is very broad and asymmetric. Such a lineshape may result from the overlapping of bulk and oxide signals since chemical shifts of the In3d levels are known to be very small.[129,130] These observations are all consistent with the fact that we are looking at an oxide layer on top of a bulk structure.[124]

The observed binding energies for various transitions are listed in Table 4.2 together with some results obtained by other workers.[124,130-7] Comparing the $In3d_{5/2}$ transitions, the binding energy of our thermally grown InO_x is very close to that of In_2O_3. Since the trioxide is known to be the only stable crystalline In oxide,[124] it can be concluded that In_2O_3 was formed on the pure In surface on oxidation. On the other hand, the identity of the Sb oxide formed thermally is still very controversial. While it has been widely assumed that the thermal oxide is Sb_2O_3 where the reaction between Sb and O is presumed to proceed under a deficient supply of oxygen,[112,125,132] Tang *et. al.*[124] recently argued that the more energetically stable pentoxide Sb_2O_5[132] was formed after heating the pure Sb sample in O_2. It is not easy to distinguish these two oxides since their difference in binding energies is very small (<1eV) and can be masked by charging effects due to their poor conductivity.[124] There are also large discrepancies in the literature values of their binding energies due to different experimental conditions and reference levels adopted (refer to Table 4.2). However, if the chemical shifts are compared instead of the absolute binding energies, it is evident that our thermal Sb oxide is more likely to be Sb_2O_5. The possibility that the two kinds of oxides co-existed

on the surface cannot be ruled out although the line shapes of the O1s and $Sb3d_{3/2}$ (oxide) peaks seem too symmetric.

TABLE 4.2

Sample	Binding Energies (eV)			Chemical Shifts[a] (eV)			Ref.
	$Sb3d_{3/2}$	$Sb3d_{5/2}$	$In3d_{5/2}$	$\Delta Sb3d_{3/2}$	$\Delta Sb3d_{5/2}$	$\Delta In3d_{5/2}$	
Sb	537.6	528.3					124
		526.5±0.2[b]					131
	537.7[c]	528.3[c]					136
	537.8[b]	528.5[b]					137
	537.8±0.5[b]	528.4±0.5					this work
Sb_2O_3	538.8[d]	529.4[d]					124
		528.4±0.2[b]			1.9±0.4		131
	538.4±0.3[b]	530.1±0.3[b]		1.6±0.6	1.6±0.6		137
Sb_2O_5	540.0[d]	530.5[d]					124
					2.5		134
	540.2±0.3[b]	531.0±0.3[b]		2.4±0.6	2.5±0.6		137
SbO_x thermal oxide	540.1[b]	530.8[b]		2.3	2.3		this work
In			443.9				124
			444.0±0.2[b]				131
			443.6±0.2[d,f]				133
			443.6±0.1[e]				135
			444.15[c]				136
In_2O_3			444.5±0.2[d,f]			0.9±0.4	133
						1.0	134
			444.9±0.1[e]			1.4±0.2	135
InO_x thermal oxide			444.5[b]				this work

p.t.o.

cont'd

Sample	Binding Energies (eV)			Chemical Shifts[a] (eV)			Ref.
	$Sb3d_{3/2}$	$Sb3d_{5/2}$	$In3d_{5/2}$	$\Delta Sb3d_{3/2}$	$\Delta Sb3d_{5/2}$	$\Delta In3d_{5/2}$	
InSb	537.0[d]	527.8[d]	444.2[d]				124
				-0.5	-0.5	0.4	130
		526.0±0.2[b]	444.5±0.2[b]				131
	537.4[b]	527.6[b]	444.3[b]				this work
InSb + O_2	537.2±0.1[b]	527.8±0.1[b]	444.3±0.1[b]	2.1	2.1	1.0	130
	540.0[c]	530.6[c]	444.7[c]				136
etched InSb sample :							this work
1	539.5[b]	530.2[b]	444.3[b]				
2	539.6[b]	530.4[b]	444.6[b]				
3	539.5[b]	530.3[b]	444.6[b]				
4	539.8[b]	530.8[b]	444.5[b]				

a : w.r.t. pure element

b : w.r.t. Cls = 285.0 eV

c : w.r.t. emission threshold of the clean samples

d : argon ion cleaned

e : w.r.t. $Au4f_{7/2}$ = 83.8 eV

f : w.r.t. Cls = 284.4 eV (pass energy = 25 eV)

After 3 cycles of annealing up to 390°C, the Sb oxide peak disappeared leaving a large bulk Sb peak in both of the Sb3d spectra (Fig. 4.4d and 4.5d). This provides additional support for the argument that the pentoxide was found since bulk Sb_2O_5 is known to lose oxygen at ~ 380°C while Sb_2O_3 sublimes at the much higher temperature of ~1550°C.[136] For InO_x, annealing at successively higher temperature narrowed the linewidth of the $In3d_{5/2}$ and shifted the peak towards lower BE reflecting a decrease in oxidation number (Fig. 4.6c). When the sample was annealed to 550°C (close to the melting point of InSb) the main peak energy was found to be ~ 444eV, similar to that of pure In (refer to Table 4.2). However, a weak asymmetry still remained which tailed off towards higher binding energies. This suggests that some In oxide is still present in the sample even after annealing at

such a high temperature. It also indicates that InO_x is much more difficult to desorb than SbO_x as expected from the difference in their free energies of formation.[132,134] It is known that In_2O_3, which is ionic in nature, has a very high melting point and low vapour pressure whereas Sb oxides are much more volatile.[132] It follows that the substrate will be easier to clean by thermal desorption if its passivating oxide contains a larger proportional of SbO_x than In_2O_3.

Note that the Sb3d peaks in InSb (dashed curve in Figs. 4.4 to 4.6) are shifted towards lower binding energies with respect to the pure Sb sample whereas the opposite trend is observed for the In3d transition. This is consistent with the oxidation state dependence of chemical shifts mentioned in § 4.2.2a and indicates a positive charge transfer from Sb to In on forming InSb.

d) Results and discussions

Figs. 4.7 - 4.9 show representative XPS spectra for InSb surfaces treated by the four cleaning methods listed in Table 4.1. At least three samples treated by each method were studied and the results were found to be very consistent (difference in binding energy ≤ 0.2eV). Reference spectra from clean InSb (dotted curve) and the thermal oxides In_2O_3 and SbO_x (dashed curve) are also shown in the relevant graphs. The low energy peak in Fig. 4.7 corresponds to Sb in a bulk InSb surrounding and the other represents Sb in an oxide ambient. For the $Sb3d_{5/2}$ spectrum (Fig. 4.8), the smaller peak at lower energy again corresponds to Sb in InSb but the high energy peak is a superposition of the $Sb3d_{5/2}$ oxide peak and the 01s peak which includes contributions from both Sb and In oxides. The spectra for each sample differ significantly from each other in terms of the intensity ratio of the two peaks. The positions of the peaks, however, are very similar (except sample 4) and closely resemble those found in the thermal oxide. The anomalous shift in binding energy observed in sample 4 can be attributed to the fact that anodization can produce much thicker oxide layers than chemical etching processes.[124] Note that the line shape of the high energy oxide doublet in the $Sb3d_{5/2}$ spectrum is very asymmetric (Fig. 4.8b) suggesting that several kinds of oxides (In_2O_3, Sb_2O_3, Sb_2O_5 etc.) may be present. In the In spectrum (Fig. 4.9), shifts in BE with respect to clean InSb as well as the lineshapes are different for different samples as the amount of In oxide present varies according to treatment.

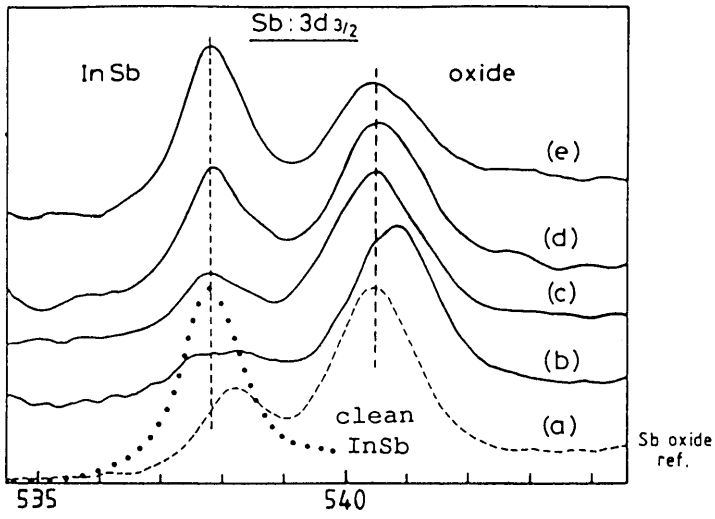


Fig. 4.7 $Sb3d_{3/2}$ spectra

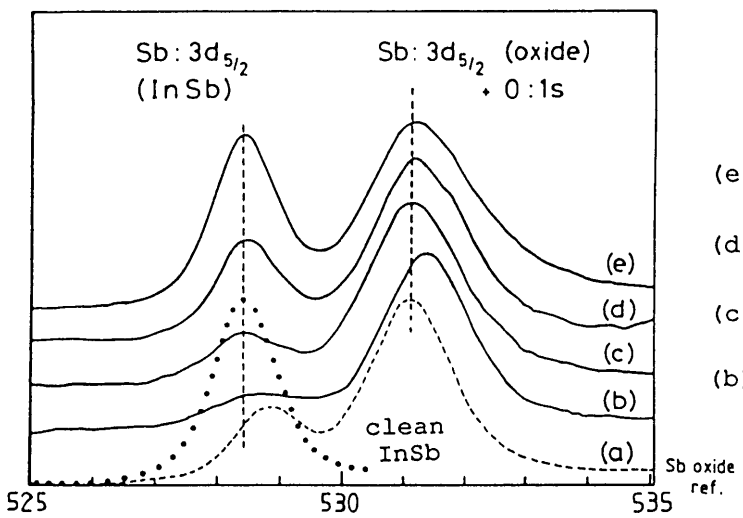


Fig. 4.8 $Sb3d_{5/2}$ spectra

(e) sample 1 (HF : HNO_3 : CH_3COOH : D I H_2O)

(d) sample 3 (HCl-EtOH + 0.4% Br_2 - MeOH)

(c) sample 2 (0.4% Br_2 - MeOH)

(b) sample 4 (anodic oxide)

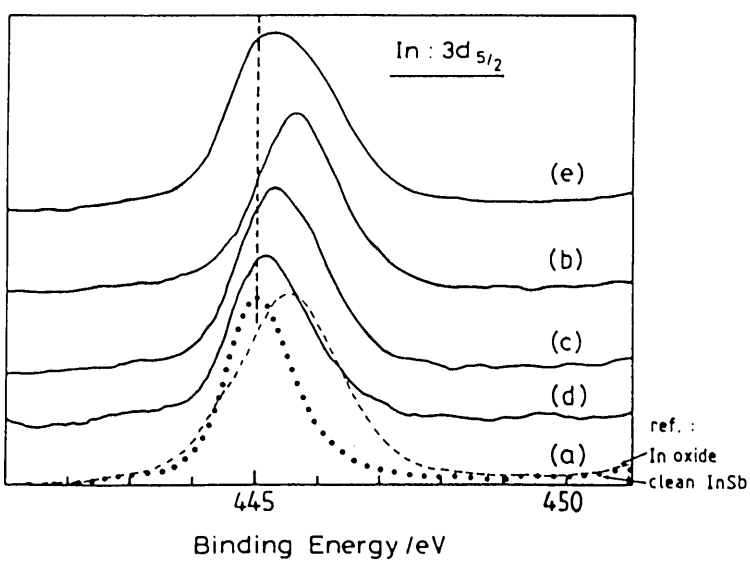


Fig. 4.9 $In3d_{3/2}$ spectra

Figs. 4.7 - 4.9 XPS spectra for four differently prepared InSb(100) substrate surfaces

Judging from the position of the main peaks, it can be concluded that In_2O_3 is formed in all these samples. The observed binding energies and chemicals shifts with respect to the pure elements are collected in Table 4.2. In cases where composite peak structures are present, energies of the high energy peaks pertinent to the oxide matrix are listed.

These samples were then cleaned in turn by thermal desorption. The $Sb3d_{5/2}$ XPS spectra for sample 1 (etched by HNO_3 : CH_3COOH : HF : DI H_2O @ 2:1:1:10) are shown in Fig. 4.10. As the sample was gradually heated, the intensity of the high energy peak decreased accordingly. After 25 mins. of heating at 440°C, this peak disappeared completely suggesting that all oxides (from both In and Sb) have been removed.

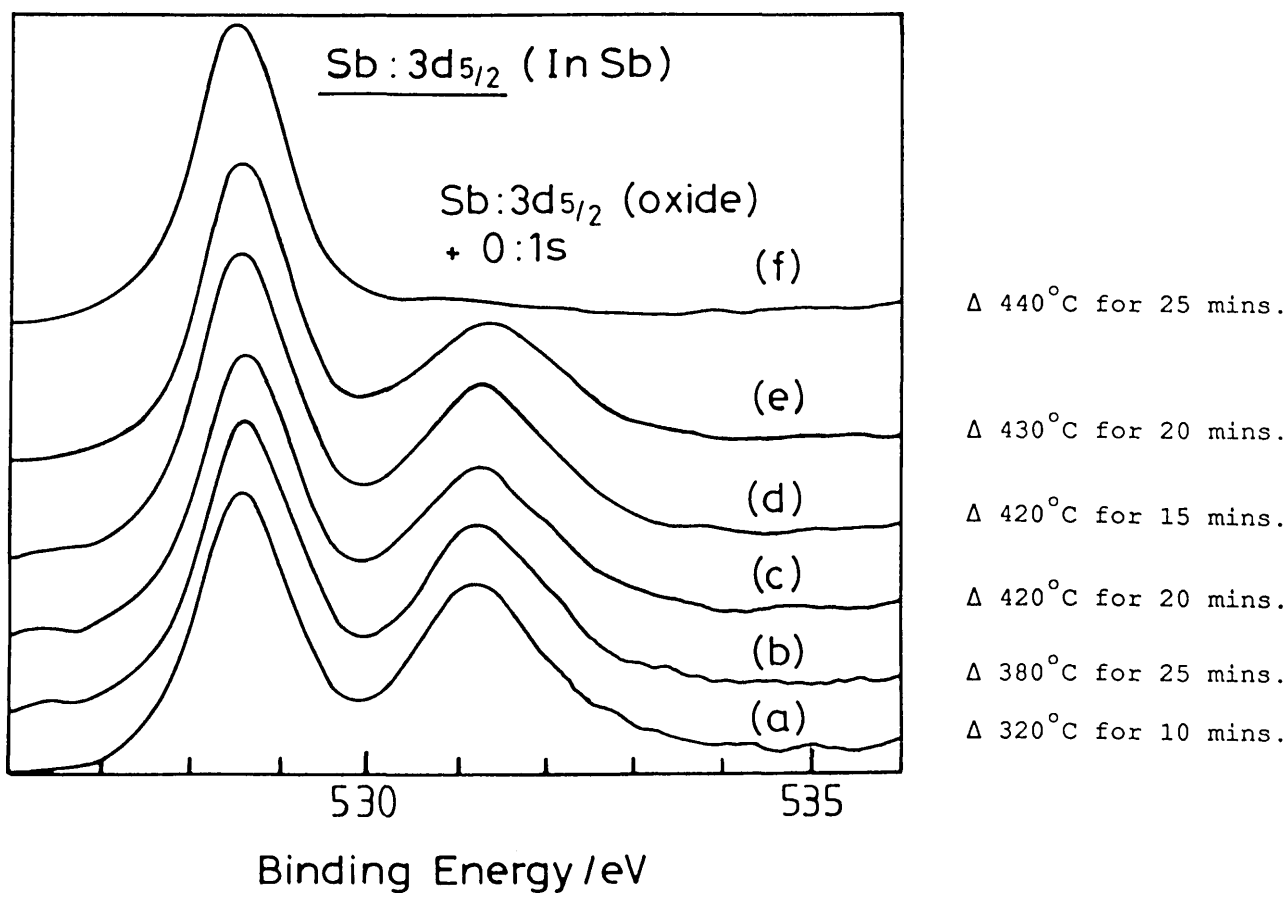
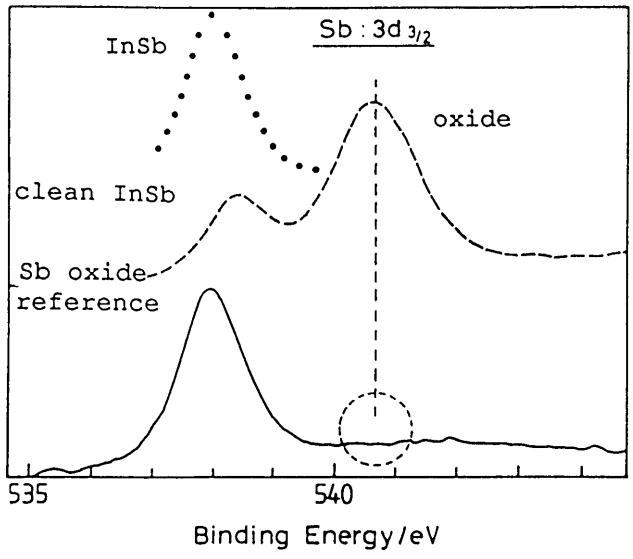


Fig. 4.10 $Sb3d_{5/2}$ XPS spectra for sample 1 (etched by modified CP4A etchant) showing the sequential removal of oxide by thermal desorption

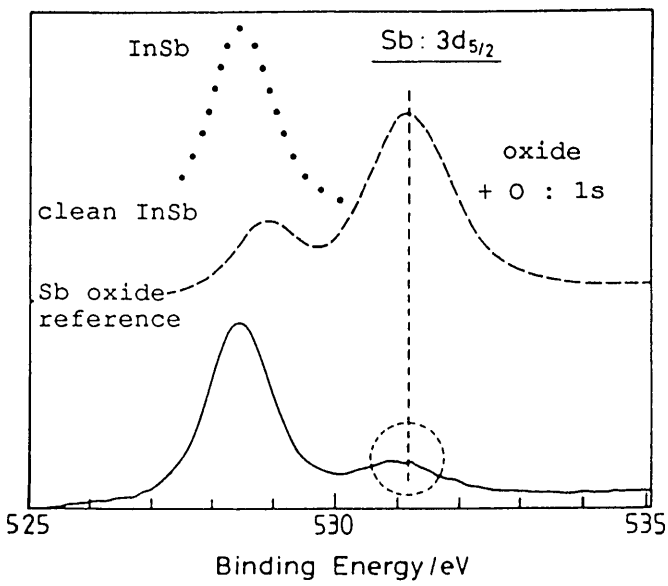
The complete removal of oxides was not, however, achieved for the other samples. Take sample 3 (etched by HCl-EtOH + 0.4% Br_2- MeOH) as an example : after heating the sample up to about 450°C, the oxide peak in the $Sb3d_{3/2}$ spectrum (Fig. 4.11a) disappeared completely. However, a sizable high energy peak still persisted in the $Sb3d_{5/2}$ spectrum (Fig. 4.11b) which is likely to come from the O1s line due to the presence of In oxide. A comparison between the $In3d_{5/2}$ spectrum of this sample and that of the clean InSb reveals a significant shift in binding energies indicating that some In oxide did remain on the substrate surface (Fig. 4.11c). This suggests that Br_2- MeOH etchants produce In oxide rich surfaces which are difficult to clean by thermal desorption, a result that is consistent with that obtained by Tang *et. al.*.[124] An enrichment of Cd has been found in Br_2- MeOH treated CdTe samples.[138] Assuming that InSb behaves in a similar fashion, a corresponding enrichment of In or In bromide can be expected. Chang *et. al.*[107] suggested that rinsing the sample with methanol and exposing it to air may convert the bromides into oxides and large amounts of In oxide can thus be formed. Following this argument, it is not surprising that sample 2 (0.4% Br_2- MeOH) was also difficult to clean.

The attempt to completely remove the anodic oxide from sample 4 was also unsuccessful. Anodization has been shown to produce passivating films comprising a mixture of In and Sb oxides[125] which is consistent with our observations (Figs. 4.7-9b). Wilmsen[139] showed that his anodic oxide formed using KOH is an In oxide containing a large concentration of elemental Sb. This is supported by the fact that KOH can dissolve pure Sb oxides but not In_2O_3.[139] It seems that our anodically oxidized sample is also rich in In_2O_3 and is therefore difficult to clean by thermal desorption.

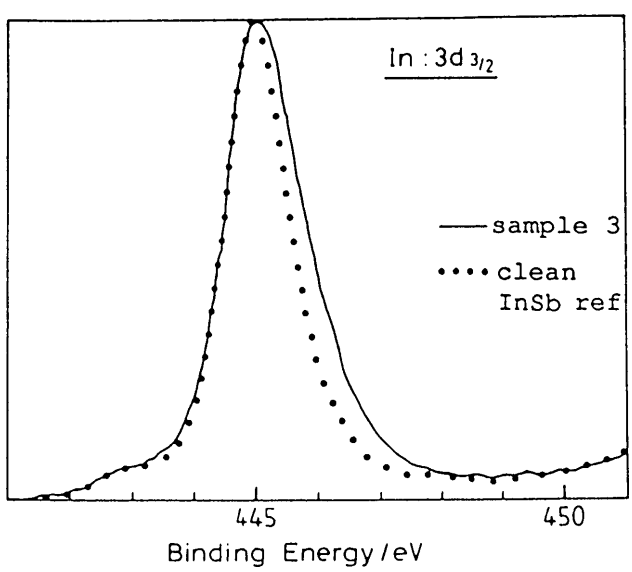
From the above findings, it can be concluded that the best chemical etchant for InSb is a mixture of HNO_3 : CH_3COOH_3 : HF : DI H_2O in the proportion of 2:1:1:10. This treatment produces a smooth surface passivated by an oxide layer low in carbon content and easy to remove by *in-situ* thermal desorption.



(a) $Sb3d_{3/2}$ spectra



(b) $Sb3d_{5/2}$ spectra



(c) $In3d_{3/2}$ spectra

Fig. 4.11 XPS spectra for sample 3 (etched by HCl-EtOH + 0.4% Br_2 - MeOH) showing the incomplete removal of In oxide by thermal desorption

4.3 In-Situ Cleaning

According to Farrow *et. al.*,[5] cycles of low energy argon ion bombardment (IB) followed by annealing is the most reproducible way of achieving a well-ordered, impurity free InSb surface which can sustain reproducible epitaxial α-Sn films. Since then, this cleaning procedure has been widely adopted for the growth of α-Sn on InSb.[33,37,39,40] However, the side effects of ion bombardment such as In island formation due to preferential sputtering of Sb[40,113] and modification of the electrical properties of the substrates[115] have also been reported. An alternative method, namely thermal desorption used by Satoh *et. al.*[34] in growing α-Sn/CdTe/InSb superlattices was therefore tried and compared with the ion bombardment method. The effects of IB and thermal desorption on surface stoichiometry were investigated in terms of the Sb/In peak ratio by XPS. In a later stage, the cleaning experiments were conducted in the MBE system. This allows the complete substrate cleaning procedure used for MBE growth (including substrate mounting, outgassing and transfer between chambers etc.) to be assessed. Surface composition and stoichiometry were checked by Auger electron spectroscopy (AES). Reflection high energy electron diffraction (RHEED) was used to monitor the surface morphology during heat treatments. The electrical properties of *in-situ* cleaned substrates were investigated using the Shubnikov-de Haas (SdH) effect. Finally, the effect of the cleaning procedures on the quality of the overlayers were studied by growing α-Sn test layers on the treated substrate surfaces.

4.3.1 XPS Studies

a) Experimental Details

Three batches of InSb substrates treated by the modified CP4A etchant were *in-situ* cleaned by cycles of argon ion bombardment followed by annealing and thermal desorption at two different temperatures. Cleanliness of the substrates was ensured by the disappearance of the C1s and the high energy peaks in the $Sb3d_{5/2}$ spectra after the *in-situ* treatments. Surface stoichiometry of the substrates was deduced from the Sb to In atomic ratio (N_{Sb}/ N_{In}). In XPS, the integrated intensity of an electron signal I_x (area under the peak) is directly proportional to the fractional atomic concentration of the species X.[128] Taking into account the difference in

photoelectric cross sections between the two elements, the atomic ratio can be estimated from :[133]

$$\frac{N_{Sb}}{N_{In}} \cong \frac{I_{Sb}}{I_{In}} \cdot \frac{\sigma_{In}}{\sigma_{Sb}} \qquad (4.2)$$

where σ is the photoelectric cross section. Values calculated by Scofield [141] are used in this study and are tabulated in Table 4.3.

TABLE 4.3

electron transitions	ionization cross-sections* (σ)
$Sb3d_{5/2}$	16.39
$In3d_{5/2}$	13.32
$Sb3d_{3/2}$	11.35
$In3d_{3/2}$	9.22

* For the Kα lines of Al at 1487 eV, in units of the C1s cross section of 22,200 barns (from ref. 141)

To achieve greater surface sensitivity, grazing angle emission was used in addition to normal emission. By changing the exit angle (ϑ), the electron escape depth is modified which in turn alters the attenuation of the substrate signal due to inelastic scattering in the overlayer.[129] The surface contribution to the XPS peak intensity thus increases (with respect to that from the bulk) with decreasing ϑ. Using an exit angle of ~ 20° in this study, the escape depth of the electrons has been limited to ~ 2 atomic layers.

Argon ion bombardment was conducted in the preparation chamber of the ESCALAB using a Penning-type AG2 argon ion source. The ion gun was operated at voltages ranging from 0.5 to 2 keV with a background pressure of approximately 10^{-6} Torr. RF heating was used for both thermal desorption ($T_{TD} \geq 400°$ C) and post-ion-bombardment annealing ($T_A \cong 200°$C).

b) Results and discussions

As ϑ was lowered to ~ 20°, marked changes occurred in the relative intensities of the XPS peaks as illustrated by the $Sb3d_{5/2}$ spectra of an as-loaded sample without any *in-situ* treatment (Fig. 4.12). The surface enhancement effect was even more dramatic when the sample was "nearly clean" after being heated at 440°C for 4 mins. (Fig. 4.13). Whereas the intensity contribution of the thin oxide layer left on the surface is hardly visible at normal emission, the spectrum obtained at ϑ = 20° by contrast exhibits a clear high-energy oxide peak. This observation is of particular importance as the credibility of an *in-situ* cleaning procedure is partly judged by its ability to remove the surface oxide completely. As a result, the $Sb3d_{5/2}$ spectrum taken at grazing angle of emission was always checked after each treatment.

A major requirement for achieving surface sensitivity enhancement with grazing emission is that the surface has to be flat. Surface roughness can lead to an averaging of electron exit angles and produce shadowing effects.[126] The observation of marked enhancement in surface sensitivity proved indirectly that our cleaning procedure can indeed produce smooth and flat surfaces.[126]

In theory, a shift in binding energy should be detected accompanying the increase in surface sensitivity. The origin of such surface core level shifts has been explained by Spanjaard *et. al.*.[142] The reduced coordination number of the surface atoms results in a narrowing of the valence band and produces a modification of the charge distribution in the surface region. This implies a local change of potential which is felt by the core electrons causing a small change in the binding energies. However, due to the limited resolution of our spectrometer, no clear surface core level shifts were detected. Instead, a slight difference in lineshape can be observed as illustrated in Fig. 4.12.

The average atomic ratios for the 3d transitions resulting from three different *in-situ* cleaning methods are summarized in Table 4.4. At normal emission, the Sb to In ratios for the thermally desorbed and IB samples are all close to unity. When the emission angle was lowered to 20°, surface stoichiometry was maintained in the thermally desorbed sample whereas the

atomic ratios of the IB sample were found to have reduced by about 10%. A considerable amount of Sb has thus been depleted from the top layers of the latter sample probably due to preferential sputtering, the well known artifact of the IB treatment.[40,113] This can often lead to the formation of In islands on the substrate surface and degrade the quality of the overlayer. The Sb to In ratios can be further reduced by increasing the ion bombardment voltage. The effect of ion dosage on the quality of the α-Sn overlayer has been investigated using AES and will be discussed in the next section (§ 4.3.1c).

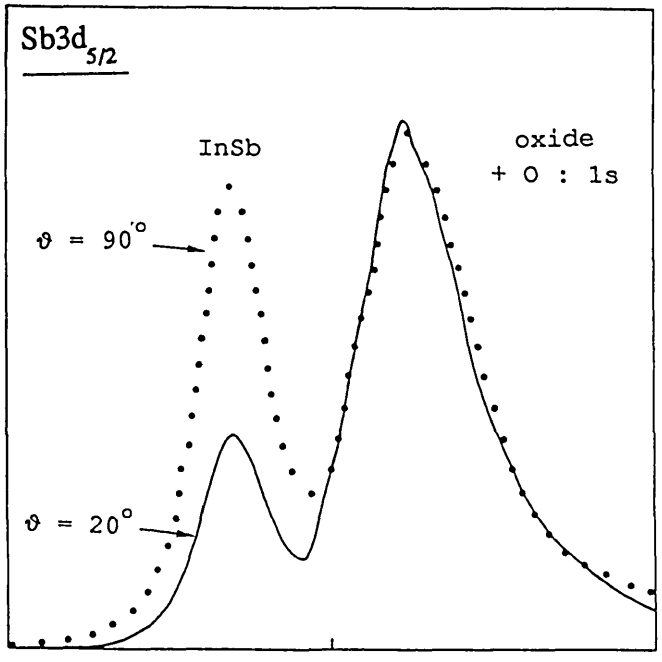


Fig. 4.12 $Sb3d_{5/2}$ XPS spectra of an as-loaded sample

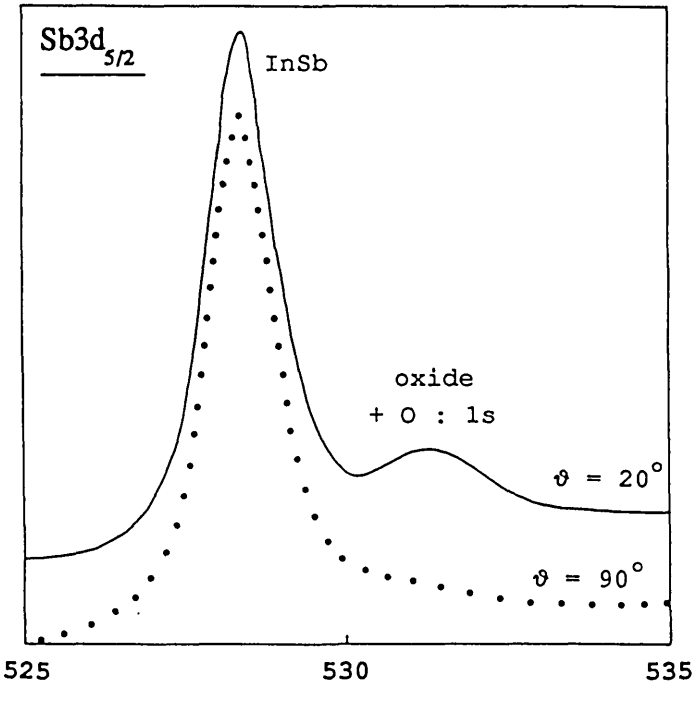


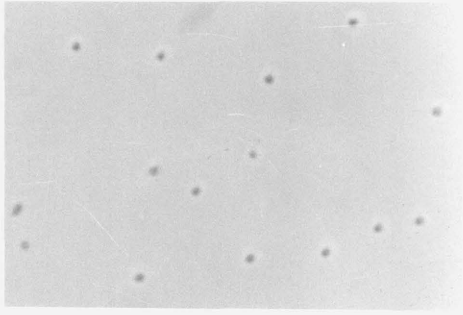
Fig. 4.13 $Sb3d_{5/2}$ XPS spectra of a "nearly clean" sample after being heated at 440°C for 4 mins.

Finally, it should be noted that although thermal desorption can produce a stoichiometric InSb surface, this process is very difficult to control in the ESCALAB. Without any *in-situ* facilities (such as RHEED) for monitoring the surface structure during annealing, it is very easy to overheat the sample. The surface stoichiometry of a sample subjected to prolonged high temperature annealing is found to be severely disturbed as its Sb to In ratios for both normal and grazing emission are well below unity (see Table 4.4). This probably occurs because of preferential desorption of Sb from the surface due to its much higher volatility compared with In. In addition, some of the thermally desorbed substrates have shown defect spots on the surface when viewed under the Nomarski microscope as a consequence of overheating (Fig. 4.14). Further experiments on thermal desorption were thus carried out in the MBE system where the RHEED technique could be utilized to monitor and control the heating process as discussed in the next section.

TABLE 4.4

In-situ Treatment	Thermal Desorption (440°C, 25 mins)		Prolong High Temp. Annealing (550°C, 5 mins)		Argon Ion Bombardment + Annealing	
θ	90°	20°	90°	20°	90°	20°
$\frac{Sb3d_{5/2}}{In3d_{5/2}}$	1.036 (1.270)	1.013 (1.246)	0.642 (0.790)	0.675 (0.831)	1.013 (1.247)	0.916 (1.127)
$\frac{Sb3d_{3/2}}{In3d_{3/2}}$	1.001 (1.233)	1.003 (1.236)	0.606 (0.746)	0.669 (0.818)	1.006 (1.238)	0.880 (1.083)

The figures in brackets are the measured integrated intensity ratios without correcting for the difference in photoelectron cross sections.



10μm

Fig. 4.14 InSb(100) surface subjected to prolong high temperature annealing showing circular pits

4.3.2 AES and RHEED Studies

In view of the difficulties encountered in using the ESCALAB for heat treatments, *in-situ* cleaning experiments were conducted inside the MBE system. Built-in analytical facilities such as AES and RHEED are used for assessing the surface cleanliness, stoichiometry and morphology of the treated samples.

a) Theoretical Background

The radiationless Auger electron emission and X-ray emission are competing processes in bringing an excited atom back to a lower energy state. Both AES and XPS involve the ejection of electrons with energies E_e characteristic of the elemental composition and chemical state of the target. Electron bombardment is used in AES to cause the ejection of either core or valence electrons, depending on the primary energy E_p. These ejected electrons do not exhibit discrete energy values because of interactions between the electrons. The core level ionized atom returns to a state nearer to the atomic ground state by the decay of an upper level electron. De-excitation may take place by the transfer of the released energy to a second electron which is ejected as an Auger electron or by emission of a characteristic X-ray photon. Due to the discrete nature of the electronic levels concerned, the energy E_{WXY} of the ejected Auger electron is characteristic of the emitting atom of atomic number Z (see Fig. 4.15) :[128]

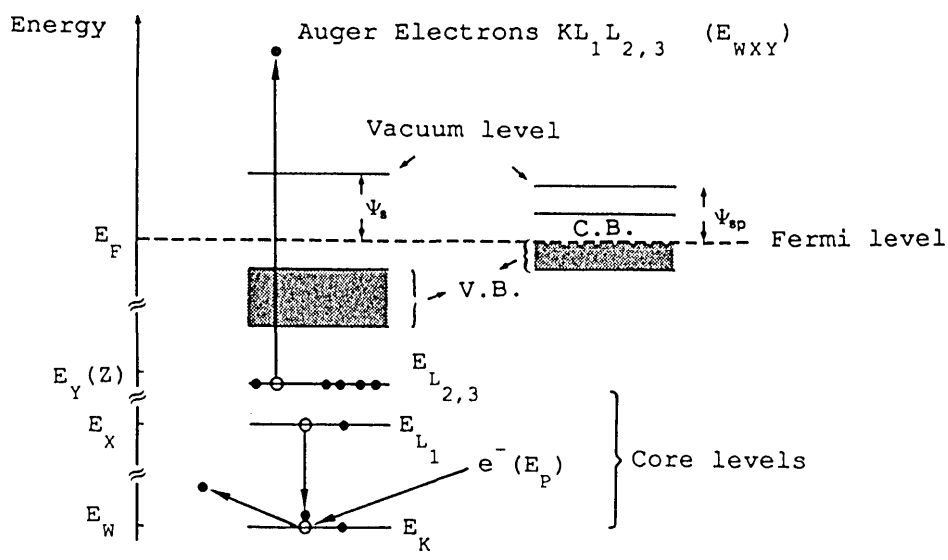


Fig. 4.15 Schematic illustration of the Auger process

$$E_{WXY} = E_W(Z) - E_X(Z) - E_Y(Z+\Delta) - \Psi_s \qquad (4.3)$$

where E_W, E_X and E_Y denote the electronic energy levels of the atom with respect to the Fermi level, Ψ_s is the work function of the sample and Δ is the de-screening correction , i.e. the change in the effective nuclear charge Z due to the de-screening in the doubly ionized final state of the atom.

AES is essentially a surface probe as the data comes from the top five layers or so, depending upon the material and the ionizing energy.[143] For transition energies up to 500eV, the mean free path of the electrons is less than 20Å.

Qualitative Auger analysis for element identification using the energy E_{WXY} and the shape of the Auger lines is straightforward since standard "fingerprint" Auger spectra of elements with Z≥3 are readily available for comparison.[144] As in XPS, considerable chemical shifts often occur in AES which are caused by changes in the electron density distribution due to chemical bonding. These shifts, however, are often less marked and are difficult to interpret in AES since three electron levels subjected to such changes are involved and will not be considered in this study.

Maximum values of the ionization cross section affecting Auger yields can be obtained when the primary energy (E_p) of the incident electrons is about 3 to 5 times the energy of the excited core level (E_W). Since the primary energies available in typical Auger systems lie between 0.5 to 10keV, there are necessarily limitations in any one part of the Periodic Table on the Auger transitions that can be excited with optimum efficiency. The most prominent Auger lines for elements relevant to this study i.e. C, O, In, Sn and Sb are summarized in Table 4.5. The energetic positions of the Áuger peaks are taken, by convention, as that of the minima in the high energy negative excursions.[126]

TABLE 4.5

Elements	Prominent Auger lines		Inverse Sensitivity Factors (α)[+]
	transitions	energies (eV)	
C	$KL_{2,3}L_{2,3}$	272	3.00 ± 0.7[*]
In	$M_{4,5}N_{4,5}N_{4,5}$	410	0.56 ± 0.1
Sn	$M_{4,5}N_{4,5}N_{4,5}$	430	
Sb	$M_{4,5}N_{4,5}N_{4,5}$	454	0.67 ± 0.1
O	$KL_{2,3}L_{2,3}$	510	2.40 ± 0.2[*]

+ from ref. 145

* assumed to be equal to those for a GaAs matrix

The surface atomic concentration (X_i) of each element i can be estimated from the simplified semi-quantitative formalism which requires only the Auger current I and the inverse sensitivity factors α which are listed in Table 4.5 :[146]

$$X_i = \frac{\alpha_i I_i}{\sum_j \alpha_j I_j} \qquad (4.4)$$

where j runs over all elements present in the sample. For InSb, the Sb to In atomic ratio is thus given by :

$$\frac{X_{Sb}}{X_{In}} = \frac{\alpha_{Sb} I_{Sb}}{\alpha_{In} I_{In}} \qquad (4.5)$$

In theory, the integrated intensity of the high energy doublet should be used since a variation in the matrix composition can alter the shape of the Auger peak as well as its height. However, due to the limited resolution achievable in our system, the main peak height was used instead. In a way, Eqn. 4.5 is an over-simplified relation. Nevertheless it enables a comparison to be made between the Sb to In ratios before and after the various *in-situ* cleaning treatments.

b) Experimental Details

Sample preparation procedures are similar to those used in the ESCALAB except for the mounting of the samples. For our MBE work, the substrate is attached to a Mo-block using molten Ga (M.P. ≅ 38°C). Samples were outgassed at about 200°C in the preparation chamber prior to *in-situ* cleaning. Three batches of substrates were studied, each having received a different treatment which included Ar^+ ion bombardment followed by annealing, thermal desorption and a combination of both. Details of the three cleaning methods employed are summarized in Table 4.6.

During ion bombardment, the entire preparation chamber was filled with high purity argon gas (Masonlite) up to a pressure of ~ 10^{-4} Torr. A VG AGS1 ion gun, capable of producing Ar^+ ions with energies ranging from 0.2 to 10 keV was used in the defocused mode. Samples were placed at near normal incidence to the ion beam. Low temperature heat treatment (≤ 300°C) including initial outgassing and post-IB annealing were conducted in the preparation chamber. The same outgassing stage can be used for heating, IB as well as Auger analysis. On the other hand, the final heat treatment employed in all of the cleaning methods was carried out in the growth chamber. This allows the surface morphology of the substrates to be continuously monitored by RHEED, thereby reducing the risk of overheating. Details of the RHEED facilities available will be described in chapter 6.

Stoichiometry as well as carbon and oxygen content of the substrate surfaces before and after *in-situ* treatments were studied by AES. Auger experiments were carried out in the preparation chamber using a VG LEG2 electron gun with a retarding field analyzer (RFA) comprising of a 3-grid optics arrangement. By varying the negative bias potential of the repeller grid, a scattered electron energy distribution can be obtained. In order to include the C, O, In, Sb and Sn signals in the spectrum, the grid potential is scanned from -560 to -200 eV (refer to Table 4.6 for the energies of these Auger lines). The primary energy of the incident electrons was set at 2keV for efficient ionization.[128]

TABLE 4.6

Treatment 1 : Ar^+ Ion Bombardment + Annealing
1. Outgas at 180°C for 30 mins. in preparation chamber
2. IB at 800eV for 1 hr. at room temperature (P ~ 7 x 10^{-6} Torr)
3. Anneal at 180 C°for 35 mins.
4. Anneal at 385 C°for 1 hr. in growth chamber
5. Perform Auger analysis in preparation chamber
6. Heat up to 385 C°and slow down to room temp. in 1 hr.
7. Start α-Sn growth
8. Interrupt growth after 0.1μm α-Sn coverage
9. Perform Auger analysis
10. Growth continued until the α-Sn layer thickness reached ~ 0.4μm
11. Perform Auger analysis

Treatment 2 : Thermal Desorption
1. Outgas at 180°C for 45 mins. in preparation chamber
2. Heat up to 350°C in growth chamber
3. Increase temperature gradually and anneal at 400°C for 90 mins.
4. Perform Auger analysis in preparation chamber
5. Repeat steps 3 and 4
6. Grow an α-Sn layer 0.15μm thick
7. Perform Auger analysis

Treatment 3 : Low Energy Ar^+ Ion Bombardment + Low Temperature Annealing
1. Outgas at 375°C for 30 mins. in preparation chamber
2. IB at 350eV for 35 mins. at room temperature (P ~ 3 x 10^{-3} Torr)
3. Anneal at 275°C for 1 hr. in growth chamber
4. Perform Auger analysis in preparation chamber
5. Gradually heat up to 275°C and slow down to room temp. in 1 hr.
6. Grow a layer of α-Sn 0.2μm thick
7. Perform Auger analysis

Since a RFA is a high pass filter, i.e. it will transmit and collect electrons with energies greater than the set pass energy, the collector current I is given by :

$$I(E) = \int_{eU}^{E_p} N(E)\, dE \qquad (4.6)$$

where E_p and eU are the primary energy of the incident electron and the pass energy of the RFA respectively. The actual electron energy distribution N(E) was obtained by differentiation accomplished electronically in our system by modulating the repeller grid with a small amplitude sine wave (~ 6V p.t.p., 4.5KHz.). The modulated output from the electron multiplier was then fed into a phase-sensitive lock-in amplifier so that signals proportional to dI/dE could be extracted.

After *in-situ* cleaning, thin layers (≤ 0.3 μm) of α-Sn were grown onto the substrates. Detailed growth procedures will be described in § 5.3.2. The effects of each cleaning method on the quality of the α-Sn overlayers were studied by RHEED and AES.

c) Results and Discussions

i) Ion-bombarded sample

Auger spectra of InSb(100) substrates prior to *in-situ* cleaning always show considerable carbon and oxygen surface contamination. A typical spectrum is depicted in Fig. 4.16a. Note that the In and Sb signals are both very weak. For this sample, *in-situ* cleaning was accomplished by an hour of Ar^+ IB at 800eV and subsequent annealing at 350°C in the growth chamber (details of the cleaning procedures can be found in Table 4.6). The resulting Auger spectrum (Fig. 4.16b) showed the removal of carbon and oxygen impurity peaks and substantial increase in the In and Sb Auger peak intensities. However the Sb/In peak ratio was found to be very small suggesting that the substrate surface was not stoichiometric. In fact, the Sb/In ratio was found to have decreased by ~ 50% after this *in-situ* treatment.

After 0.1 μm of α-Sn was grown, a series of Sn-related peaks emerge in the Auger spectrum (Fig. 4.16c). However, when growth was terminated after

the α-Sn coverage had reached ~ 0.4 μm, a sizable In signal still remained which was somewhat unexpected for such a high coverage. (Fig. 4.16d). The persistence of the In signal (but not Sb) on α-Sn overlayers grown on IB InSb substrates has also been reported by Middelman *et. al.*[40] in their XPS studies. A possible cause for these observation may be the preferential sputtering of Sb leading to the formation of free In which coalesces into droplets. The formation of such droplets is well known in sputtered and annealed surfaces of other III-V compound semiconductors.[112] This is also consistent with the low Sb/In peak ratio recorded in the Auger spectrum prior to growth (Fig. 4.16b) as well as our ESCA data. It is also known that between the In droplets, the surface is clean and well-ordered. This explains the fact that sharp RHEED patterns revealing clear surface reconstructions could still be seen in the IB samples.

It has also been suggested that the presence of the In peak may be caused by an exchange reaction at the interface.[40] Indium released during the reaction is free to diffuse through the α-Sn layer and can coalesce into droplets. However, the possibility of this happening may be very remote since no stable compound of Sn and Sb (nor Sn and In) is known to exist.

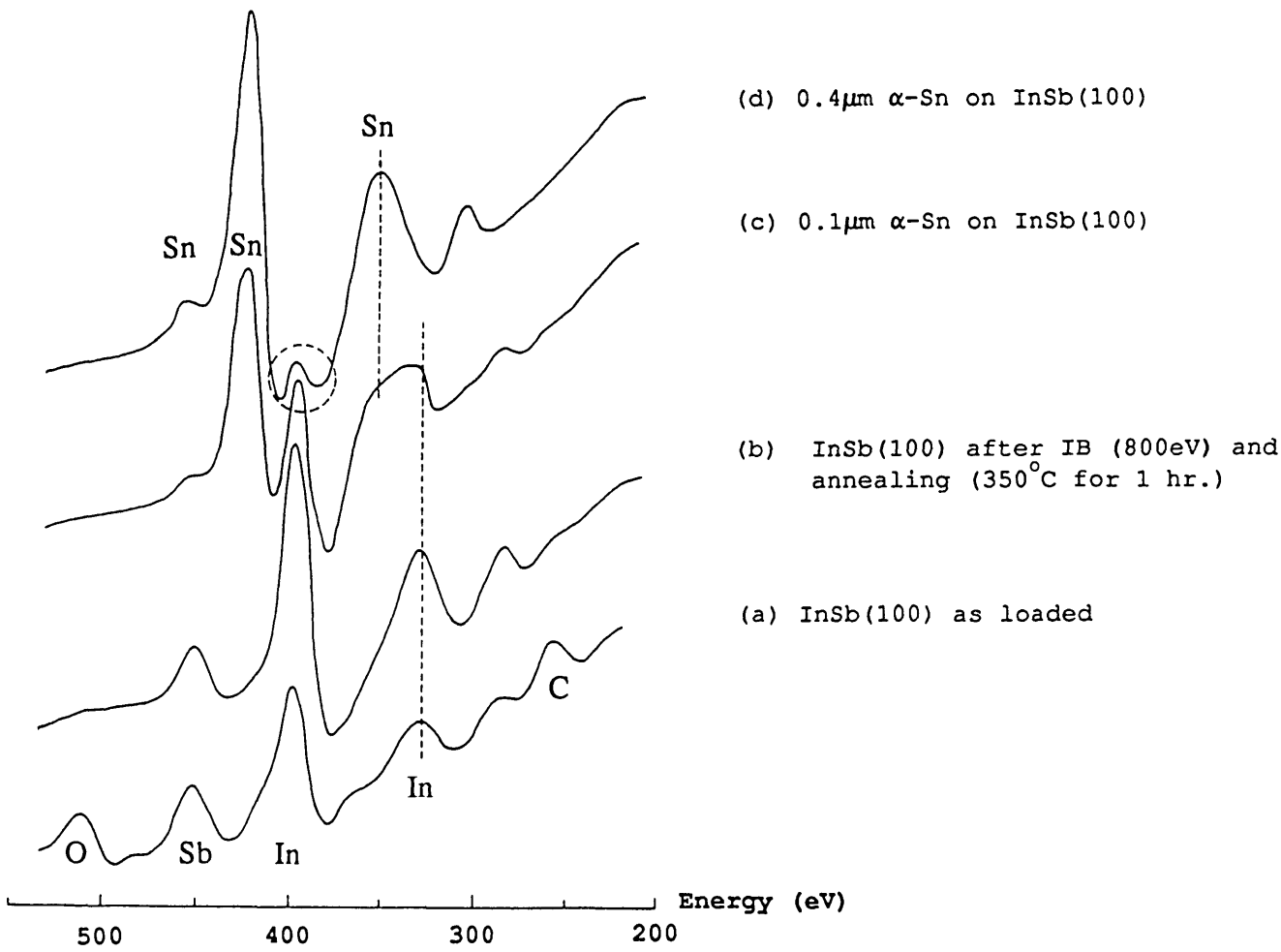


Fig. 4.16 Auger spectra of an ion-bombarded InSb(100) substrate before and after the growth of an α-Sn overlayer

ii) Thermally desorbed sample

After an Auger spectrum of the as loaded InSb substrate was obtained (Fig. 4.17a) and initial outgassing was completed, the sample was transferred to the growth chamber for further heat treatment. Starting from 350°C, the substrate temperature was slowly raised at approximately 10°C every 5 mins. with a waiting period of 10 mins. At the beginning, the RHEED pattern was very diffuse. With increasing temperature, the background intensity decreased and a series of discrete spots began to emerge. Gradually, these diffraction spots became elongated and faint streaks could be seen. At this point, the substrate temperature was frozen until a clear (4x2) surface reconstruction was revealed. Changes in the RHEED patterns recorded during the desorption process are shown in Fig. 4.18. Interpretation of RHEED patterns is the subject of chapter 6 (§ 6.4).

The sample was then cooled down to room temperature and transferred back to the preparation chamber for Auger analysis. After two cycles of heating at around 400°C, the oxygen and carbon peaks disappeared, leaving only In and Sb related peaks (Fig. 4.17b). There was also significant increase in the Sb/In peak ratio (~ 50%) compared with that treated by ion bombardment (Fig. 4.16b).

After depositing 0.15 μm of α-Sn, no trace of In could be seen in the Auger spectrum (Fig. 4.17c). This suggested that the In signal observed in Fig. 4.16c from the previous sample might indeed be caused by IB rather than an interfacial reaction. Unfortunately, unlike that sample, this one was very difficult to remove from the Mo-block after growth. The whole assembly had to be heated up to ~70°C before the sample could be removed. This temperature is dangerously close to the phase transition temperature of the α-Sn film and will inevitably degrade its quality. It is speculated that the Ga may have alloyed into the Mo-block during the high temperature annealing process. It seems that thermal desorption can only be used in the MBE growth of α-Sn on InSb if an alternative can be found to replace the Ga. One possibility may be to use a non-bonded heaters which is now commercially available.

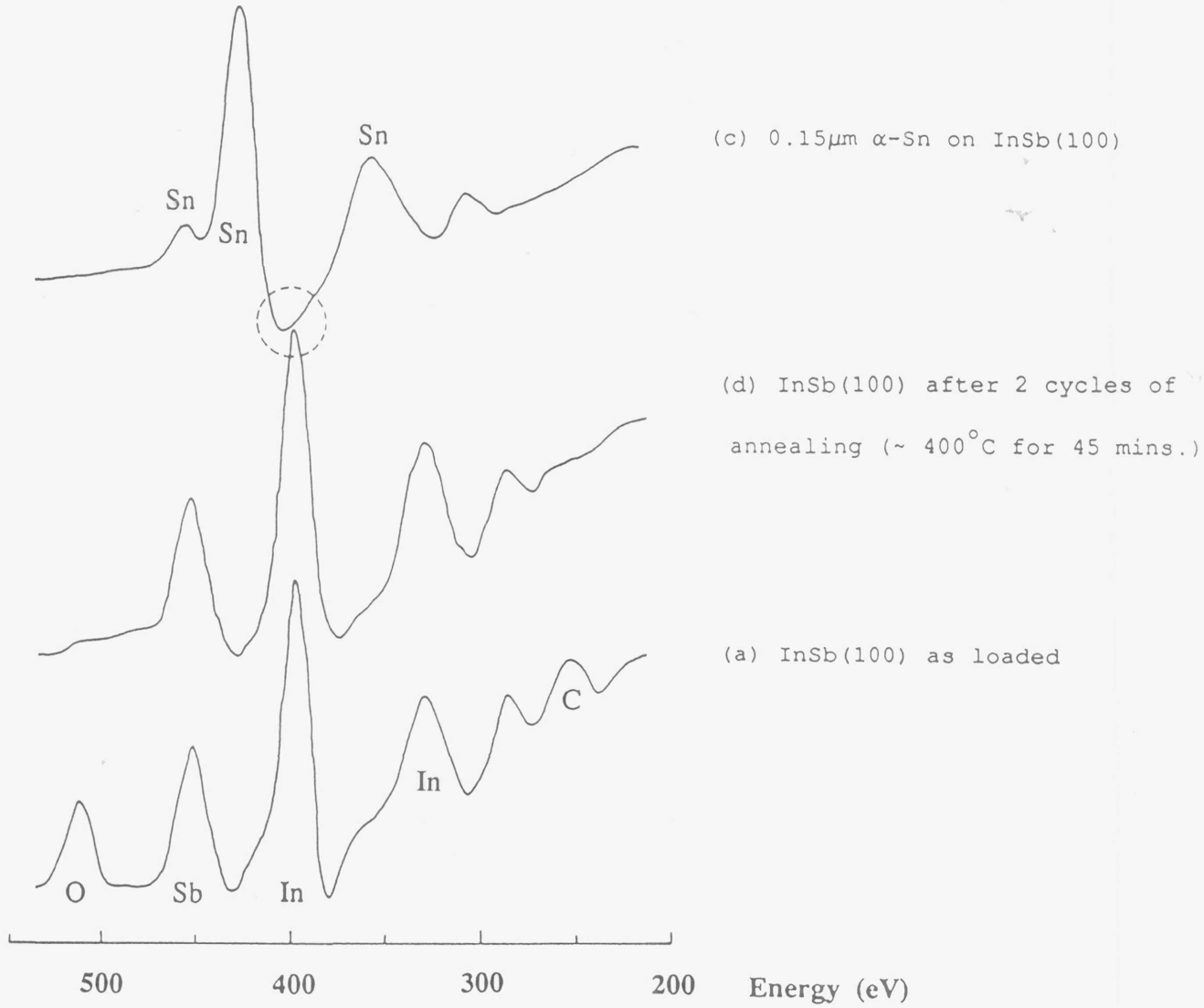


Fig. 4.17 Auger spectra of a thermally desorbed InSb(100) substrate before and after the growth of an α-Sn overlayer

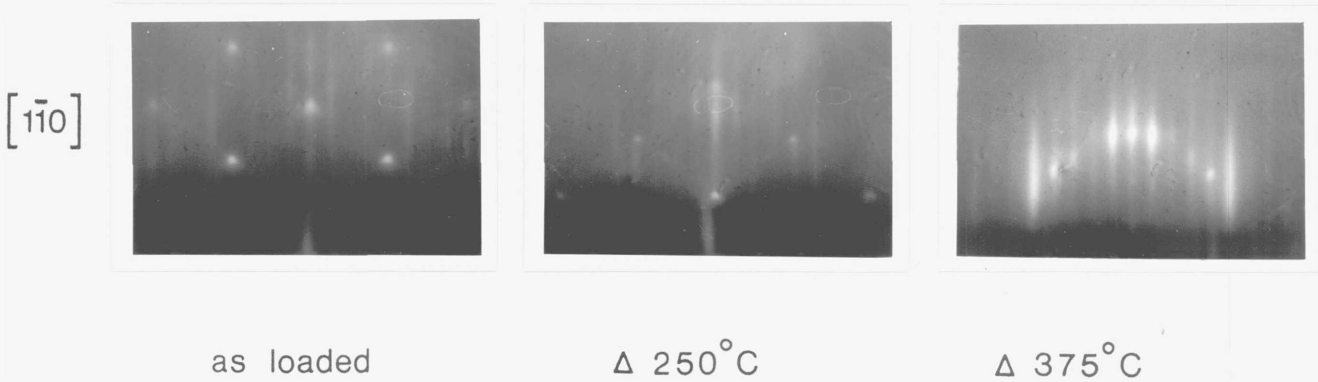


Fig. 4.18 RHEED patterns observed from an InSb(100) substrate surface during thermal desorption

iii) Low energy Ar^+ Ion Bombarded Sample

It is now obvious that for the MBE growth of α-Sn films, *in-situ* cleaning of the InSb substrates should not involve prolonged high temperature treatment nor high energy IB that would induce the formation of In droplets. To conform with these requirements, Ar^+ ion bombardment was conducted at a much reduced energy of 350eV for an hour. The substrate was then gradually heated up in the growth chamber to anneal the surface damage. Unlike the thermal desorbed sample, a clear (4x2) RHEED pattern could be seen as soon as the temperature reached ~ 275°C (see the inset of Fig. 4.19). The sample was left at this temperature for another hour before it was transferred back to the preparation chamber for Auger analysis. Using these parameters, only one cycle of IB and annealing was enough to remove all traces of carbon and oxygen. The Sb/In peak ratio was found to have increased by nearly 40% after this *in-situ* treatment (Fig. 4.19a and b).

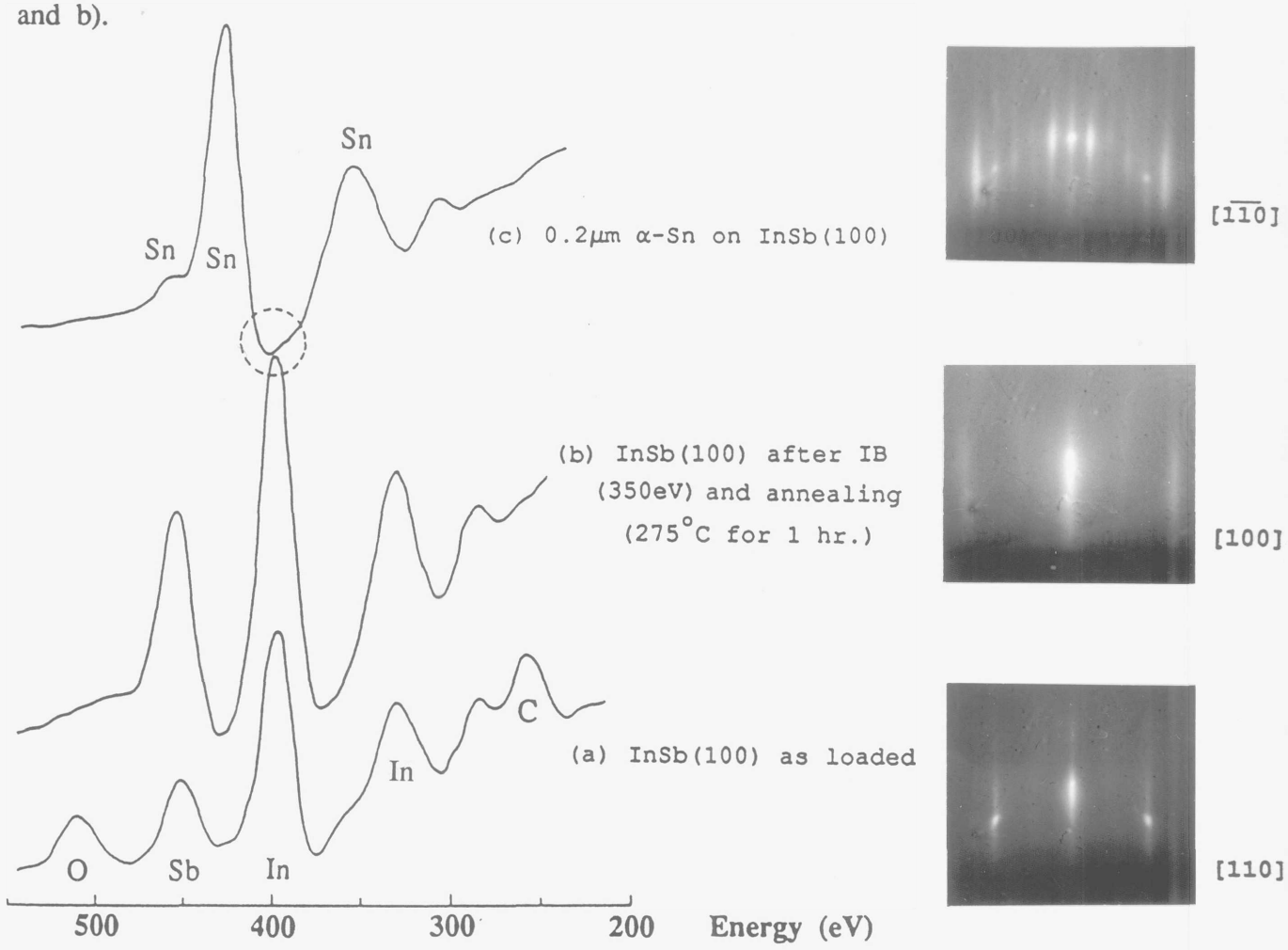


Fig. 4.19 Auger spectra of a low energy Ar ion-bombarded InSb(100) substrate before and after the growth of an α-Sn overlayer (inset : RHEED patterns of the cleaned substrate prior to growth)

After the growth of a 0.3 μm α-Sn film, no In peak was observed in the Auger spectrum (Fig. 4.19c) suggesting that the problem of In droplet formation has been surmounted by lowering the ion bombardment energy. By reducing the annealing temperature to ~ 275°C, alloying between Ga and Mo has also been avoided and the sample could be easily removed at temperatures below 40°C.

Besides the AES and RHEED results, both magneto-transport and X-ray diffraction measurements also indicate this to be the favoured cleaning method. Our Hall data indicated that InSb substrates prepared in this way retained their bulk electrical characteristics down to low temperature. Zheng *et. al.*[115] have recently observed a 2DEG exhibiting Shubnikov-de Haas (SdH) oscillations in a CdTe/InSb heterostructure. They suggested that the 2DEG actually arose from an IB-induced n^+ region in the p-type substrate since the SdH oscillations could be observed even without the CdTe overlayer. In contrast to their results, our substrate bombarded at 350 eV (as compared to the 500eV they used) did not show SdH effect at liquid helium temperature. Details of SdH and other magneto-transport results will be presented in chapter 7. In addition, the FWHMs of our InSb substrate peaks in double crystal X-ray rocking curves lie between ~ 17-19 arc. sec. for the (400) reflection.[38] These linewidths of InSb substrates are commonly assumed to indicate crystal perfection acceptable for MBE application and are among the best values reported for the growth of α-Sn.[5,106]

4.4 Conclusions

Several cleaning techniques for InSb(100) substrates have been investigated, with emphasis on their suitability for supporting MBE growth of high quality α-Sn films. The credibility of each method was assessed using several surface science techniques including XPS, AES, RHEED and Nomarski microscopy.

For *ex-situ* treatment, the surface morphology of the sample and the composition of the passivating oxide layer formed were of prime concern. Passivating layers containing large amounts of In oxide were found to be very difficult to remove. A modified CP4A etchant consisting of HNO_3 : CH_3COOH : HF : DI H_2O in the proportion 2:1:1:10 was found to be the

best choice. This etchant was found to produce a flat surface with low defect density and a passivating layer consisting mainly of easily removable Sb oxide.

Two of the most commonly used *in-situ* cleaning method namely, Ar^+ ion bombardment (employing energy in excess of 500 eV)[33,39,40,141] and thermal desorption (at temperature $\geq 415^{\circ}C$)[34] have both been found to be unsuitable for the α-Sn/InSb system. Instead, a combination of low energy ion bombardment (~ 350 eV) and low temperature desorption (~ $275^{\circ}C$) was found to produce the most satisfactory results.

CHAPTER 5 MBE GROWTH OF SUBSTRATE-STABILIZED α-Sn

5.1 Introduction

As discussed in the previous chapter, MBE is a growth technique involving reactions between thermal molecular beams and crystalline surfaces. The technique is distinctly characterized by its ability to control the growth precisely, for instance, by interrupting the incident atomic or molecular beam. This characteristic enables the growth of very complicated low-dimensional semiconductor structures. The success of the MBE technique, however, requires a clean ultra-high-vacuum (UHV) chamber; contamination-free evaporation sources; diagnostic tools for monitoring the growth as well as the provision of facilities for introducing samples into the system without breaking the vacuum and for substrate cleaning. Due to the stringent requirement for cleanliness and the complicated nature of the process, a commercial MBE system is very expensive (≅ £200 - £500K at the time of this work). Through the co-operation with Leisk Vacuum Co., we have assembled a MBE system at a much lower cost. This system is custom-designed (by Dr. W. T. Yuen of Physics Department, Imperial College) and embodies features distinct from "off-the-shelf" commercial machines. Details of the system configuration and the important components are given in § 5.2. Special emphasis are placed on the growth chamber and the design of the Knudsen cells. Where appropriate, the significance of the design aspects to the quality of the grown layers will be discussed. The performance of the system in terms of vacuum integrity and cleanliness are assessed and routine procedures for preparing the growth environment are outlined in § 5.3.

In the second half of this chapter, the growth of α-Sn films is described in detail. The effect of growth conditions such as substrate orientation, overlayer thickness, growth rate and substrate temperature on the quality and stability of the α-Sn films is studied. The $\alpha \rightarrow \beta$ phase transition temperature, as determined by optical microscopy, is used as a measure of stability. The quality of the α-Sn/InSb layers is assessed by reflection high energy electron diffraction (RHEED) and Auger electron spectroscopy techniques. Finally, the optimum growth conditions used for the growth of α-Sn thin films are presented.

5.2 System Configuration

The main building blocks of our MBE system are shown in Fig. 5.1 with the principal functions indicated. This system comprises three units separated by gate valves : a growth chamber, a preparation and analysis chamber and a sample introduction chamber (loadlock). It is important to note that the latter two chambers are positioned orthogonally so that the transfer rod "B" (see Fig. 5.1), which transfers samples between the preparation and growth chambers is never exposed to the ambient during a growth run.

Substrates are bonded to 3-pin molybdenum substrate-mounting blocks (Mo-block) by a liquid layer of Ga. The substrate assembly is introduced into the preparation chamber via the loadlock by means of a magnetically-driven transfer mechanism (transfer rod "A" in Fig. 5.1). Using the orthogonal transfer rod "B", samples can be parked at the outgassing stage in the preparation chamber or at the substrate manipulator in the growth chamber. Both of these rods are terminated with a sample holder cup which incorporates slots and bayonet fittings for retaining the Mo-blocks.

Substrate cleaning facilities such as heat treatment and ion beam bombardment as well as surface analysis equipment for LEED and AES studies are installed in the preparation chamber. Rough pumping, common to the whole system, is provided by four sorption pumps operated sequentially.

Reproducible growth of semiconductor structures is realized by utilizing effective automatic control over the various growth parameters. This entails the use of a real time computer control system to ensure synchronization of events throughout the growth process. An IBM-AT compatible computer is used to control the Knudsen-cell temperatures (i.e. molecular beam flux), the substrate temperature and the shutter status. The computer is also used to monitor the background pressure of each chamber and detect any sudden pressure upsurge.

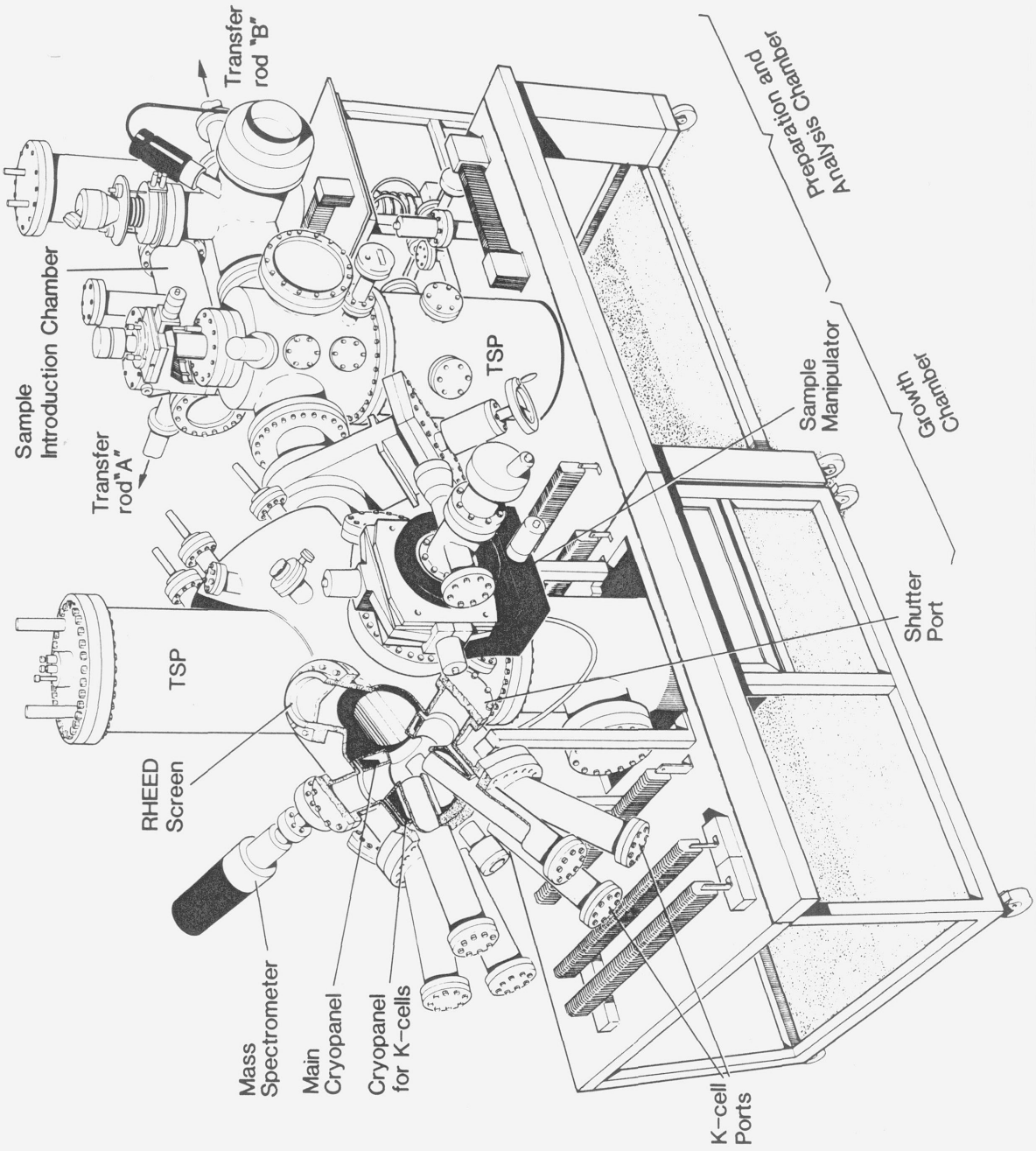


Fig. 5.1 Schematic drawing of the MBE system used in this work

5.2.1. Growth Chamber

The growth chamber is the most important compartment in the whole MBE system. It houses all the necessary components which enable controlled epitaxial growth to take place in an extremely clean environment. For our system, these include Knudsen effusion cells (K-cells) and the associated shutters; liquid nitrogen (LN_2)-filled cryogenic shrouds; a substrate manipulator with heating, translation and double-axis (angular and azimuthal) rotation facilities; a RHEED system consisting of a 5 KeV electron gun and a phosphor screen; a pressure control unit with a VG QX200 quadrupole mass spectrometer and several ion gauges. The schematic cutaway view of the growth chamber is presented in Fig. 5.1. Custom-designed features such as the geometry of the chamber, cryopanels, manipulator and Knudsen cells etc. will be discussed in the following sections.

a) Geometry of the Growth Chamber

The axis of the growth chamber is tilted at 26° to the horizontal in order to maximize the lifetime of the evaporation sources while at the same time preventing flakes of condensates from falling back into the Knudsen cells (K-cells). Six K-cell ports each subtending at 26° to the substrate surface are fitted radially on a 16-inch flange, giving an effective effusion distance (K-cell to substrate) of about 125mm. Chemical cross-contamination between adjacent cells is minimized by a baffle arrangement which thermally and chemically isolates each cell in their own LN_2-cooled baffle enclosures. Four cells loaded with In, Sb, Sn and Ge sources are housed in these ports and the arrangement is shown in Fig. 5.2. Among them, the Sn source has the highest consumption rate and is therefore placed in the lowest position so that the maximum amount of source material can be loaded into the crucible. The K-cell containing the high vapour pressure Sb source is placed diagonally with respect to the Ge cell which is operated at the highest temperature (up to ~ 1350°C during outgassing). The shutter ports were blanked throughout this study although pneumatically-controlled shutters using bellows have been designed and made with the co-operation of VSW Technology Ltd.. They will be installed into the system when the growth of InSb buffer layers and more complicated structures such as α-$Sn_{1-x}Ge_x$ superlattices commences. A view port at the centre of the K-cell flange is included for temperature measurement (e.g. by

using an infrared pyrometer). This port is also used to monitor the surface reflectance of the sample during growth. This is particularly useful for α-Sn growth since the α → β phase transition is accompanied by a colour change from grey to white.

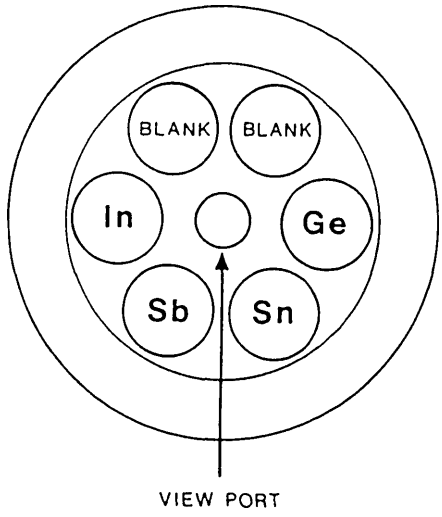


Fig. 5.2 Arrangement of K-cells containing different source materials used in this work

Primary pumping of the growth chamber is provided by two diode ion pumps (7.5KV) capable of producing a combined pumping speed of 280l/s. Secondary pumping in the near vicinity of the growth environment, essential for the production of high purity semiconductor material, is provided by a LN_2-baffled titanium sublimation pump (TSP). The cryopanel of the TSP, having an extra large surface area designed for pumping 1500 litres of N_2 per second, is positioned vertically above the growth region and securely supported by the filling ports.

b) Cryopanelling

To provide an optimum growth environment, two sections of cryopanel are used. The main cryopanel is essentially a cylindrical vessel employing a double skin reservoir design enclosing the growth region. A second cryopanel, thermally isolated from the main one, is dedicated to the hot evaporation sources (see Fig. 5.1). The cooling of the two cryopanels can be controlled independently. The advantage of this configuration is the resulting reduction of heat load into the growth region. This can minimize the creation of N_2 gas pockets in the main cryopanels and sudden eruptions of gas from its wall towards the growth region. In addition, the aperture

size of the main cryopanel is restricted such that only molecules that are directed at the substrate are allowed to pass through. This arrangement can reduce the amount of stray radiation or molecular flux hitting onto the cryopanels of the growth region and can thereby improve system cleanliness during growth.

c) Manipulator and Substrate Carousel

The requirements of angular as well as azimuthal motion, robust construction for holding large and bulky substrate mounting blocks, durable and precise motion control for sample transfer etc. mean that the standard manipulator design for surface science studies is unsuitable for MBE work. The substrate manipulator used in this system is modified from a Huntington PM-600-XYZT model and is shown in Fig. 5.3a. The item as purchased can provide linear motion in the X, Y and Z directions, 360° rotation along the primary axis and tilting up to 6° using a three-micrometer tilt system. In order to determine unambiguously the surface reconstruction of the sample, RHEED patterns along two or more azimuths have to be monitored (see § 6.3). Azimuthal motion can be realized by connecting an inner rotary shaft to the existing rotary drive.

To the end of the main shaft, a stainless-steel plate is attached to support a beam monitoring ionization gauge (BMIG) and a cylindrical gearbox which can drive two substrate holders (see Fig. 5.3b). The main substrate holder designed and made by Leisk has been used for the majority of the work presented here. Recently, the heater assembly has been modified to improve the uniformity of the heating profile. The new design consisted of a Ta wire (0.5mm dia.) wound non-inductively around a specially machined PBN (pyrolytic boron nitride) annulus with holes along its circumference (supplied by Fulmer CVD Ltd.) as shown on the left of Fig. 5.3b. The substrate holder as well as the BMIG can be rotated into and out of the beam flux using the angular motion drive.

A very basic requirement for MBE growth is that the epilayer should have uniform thickness and doping profile characteristics across the whole substrate. Substrate rotation, first used by Cho and Cheng,[147] has been proved to enhance significantly the thickness and composition homogeneity of the grown film. However, Farley *et. al.*[148] have recently shown that

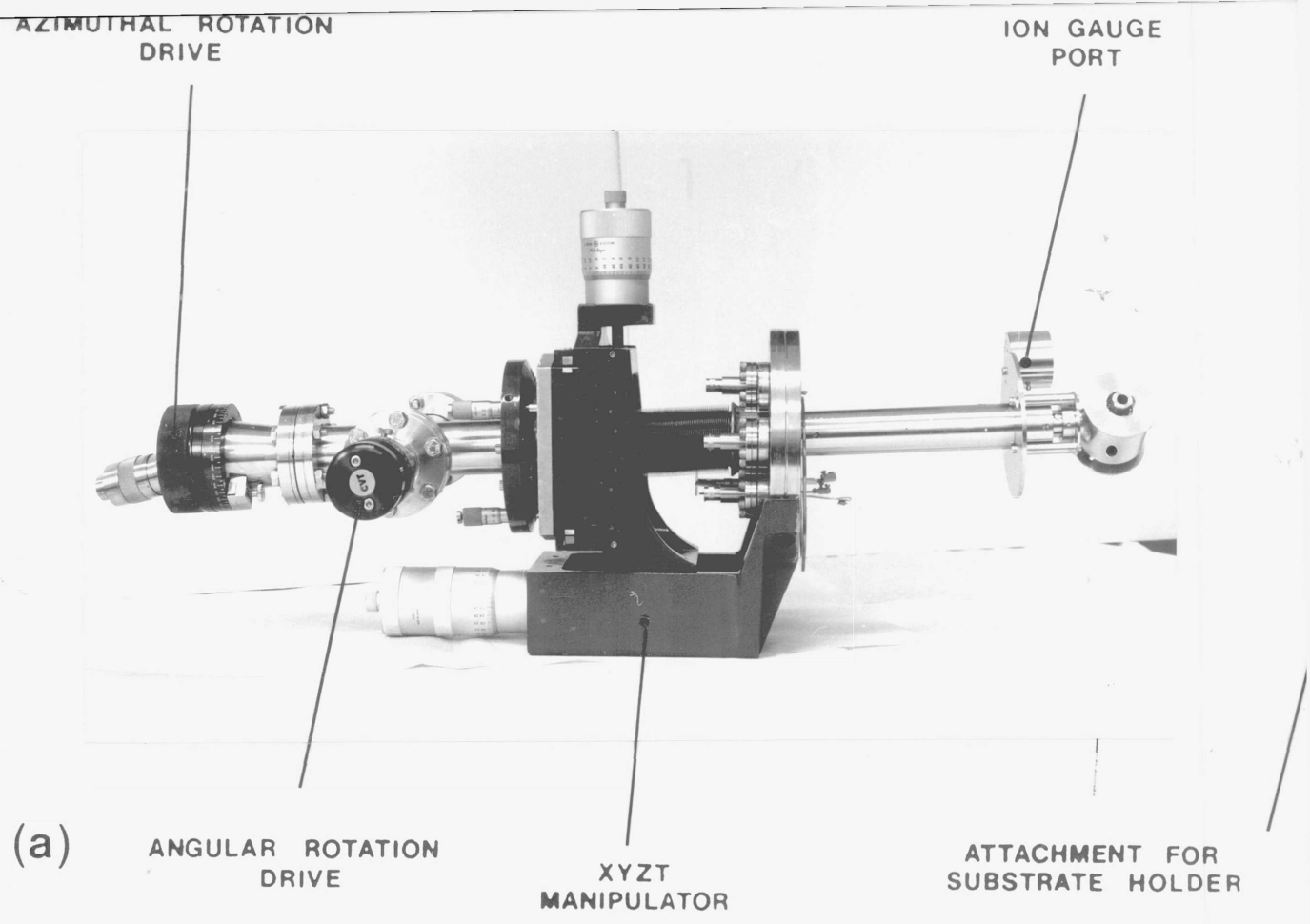




Fig. 5.3 Pictures of the modified substrate manipulator used in the growth chamber : a) Overall view (the substrate holder has been detached for clarity). b) Close-up view of the substrate carousel. The heater assembly inside the substrate holder is shown schematically on the left.

rotating the substrate may cause high levels of carbon-related contamination (e.g. C, CH_4, CO, CO_2 etc.) to be released and incorporated into the MBE layers. On a research level where only small substrates (1/4 of a 2-inch wafer) are used, as in our studies, sufficient uniformity can be achieved simply by the close proximity of the source cells.

d) Knudsen Effusion Cells (K-cells)

MBE growth of high quality epitaxial films requires evaporation sources to provide stable and ultrahigh purity molecular beams of appropriate intensity and uniformity. By far the most common method of flux generation is via thermal evaporation from resistively-heated furnaces, although other techniques such as electron beam evaporators, electrochemical cells and gas-cracking cells etc. have also been employed.[84,88] Charges of the source material are contained in an enclosure with a very small orifice which directs the flux to the substrate.

For the growth of α-Sn and α-Sn_xGe_{1-x} alloys, some of our K-cells have to be operated at temperatures as high as 1300°C. At these temperatures, decomposition of furnace fabrication material has been shown to cause contamination of the molecular fluxes.[149] Specifically, the choice of insulator material has proven to be critical in deciding the residual impurity level of the grown layers. Sintered alumina (Al_2O_3) was found to be unsuitable for use at temperature above 850°C[84,88,149] and the more chemically inert PBN is used as an insulator as well as crucible material in all our K-cells. A total of four K-cells of two different designs are currently installed. Both types are water-cooled since it is considered to be more efficient at dissipating heat than their LN_2-cooling counterparts.[88]

The first design is based on a spirally-wounded, two-zone heating configuration (supplied by VSW Technology Ltd.). The heating filaments are arranged in the form of a spiral supported at the side by thin PBN rods as shown schematically in Fig. 5.4a. The main drawback of this design is the use of lengthy PBN rods which are in intimate contact with the hot filament, thereby inducing unnecessary decomposition/outgassing of the PBN rods when the cell is at high temperature.[84,88] This K-cell is currently used to house the Sn source.

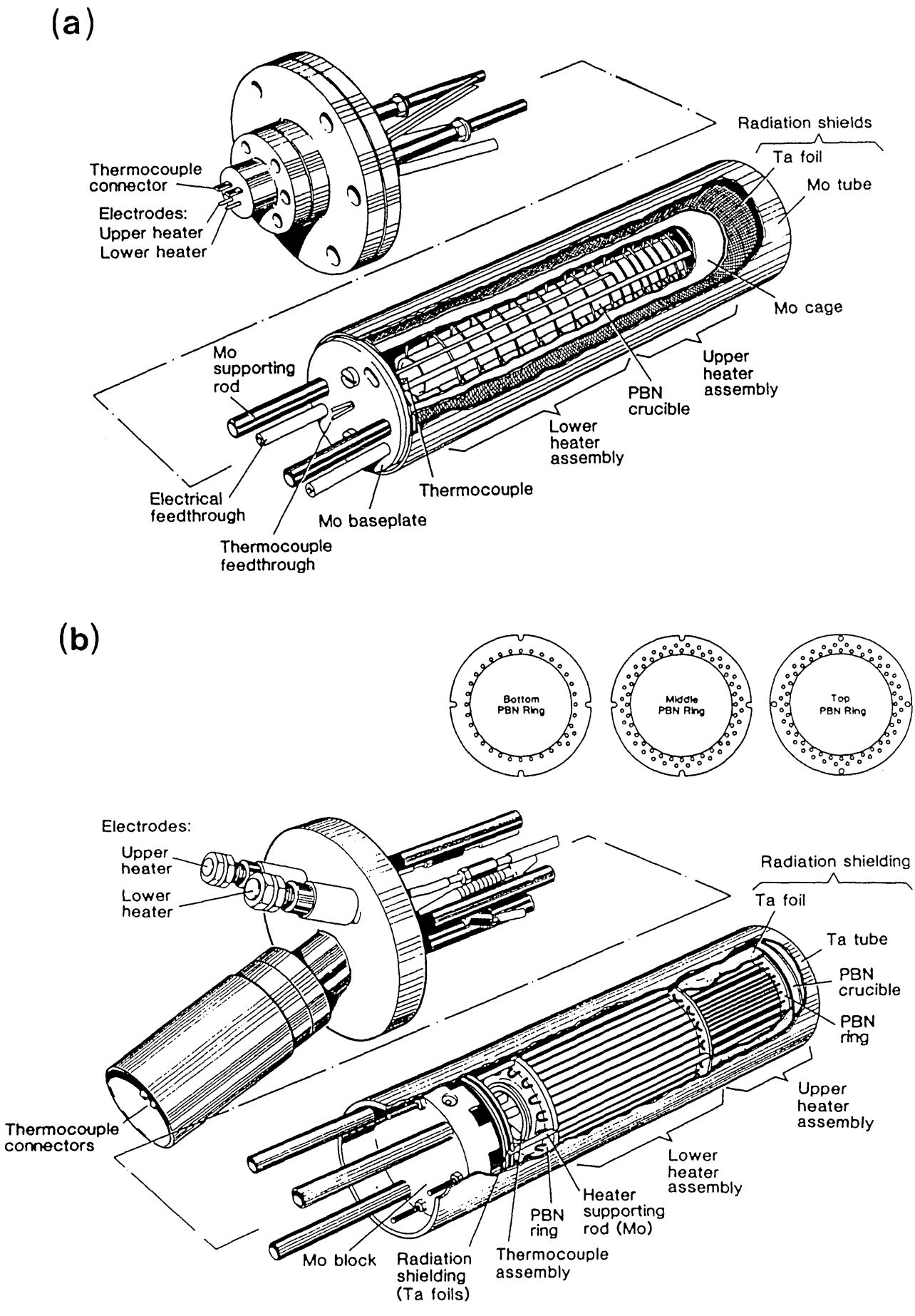


Fig. 5.4 Schematic drawings of the two K-cell designs used in this study :
a) Spirally-wound, two-zone heating K-cell supplied by VSW.
b) Home-designed K-cell. The three custom-made PBN annulus used for supporting the heater wires are shown at the top right hand corner.

The rest of the K-cells are home-designed (constructed with the co-operation of Leisk Vacuum Ltd.) and adopt a "up-and-down" configuration for the heater elements. A schematic representation of this type of K-cell is shown in Fig 5.4b. These cells are designed to operate at temperatures up to ~1300°C and sustain short outgassing sequences at ~ 1400°C as required for Ge evaporation.

The design of our K-cells is distinctly different from conventional versions which use massive amount of PBN tubings for electrical insulation. The high thermal mass of the PBN assembly together with the inevitable decomposition of the PBN at high temperatures (≥ 1400°C)[84,88] has limited the applicability of the "up-and-down" configuration for high temperature K-cells (e.g. for evaporating Ge in our case). As an alternative, our heater assembly is made up of a Ta wire (0.5mm dia.) wound non-inductively from end to end through three custom-made ultra-thin PBN annuli (Fulmer CVD Ltd.) as depicted at the top of Fig. 5.4b. Note that the amount of PBN used is minimal.

As shown in Fig. 5.4b, a two-zone heating configuration is formed which minimizes radiation heat loss and large temperature drop in the vicinity of the orifice. The temperature difference between the base and orifice of the crucible is less than 30°C as measured by an optical pyrometer. Stable temperature control is provided by proportional-integral-derivative (PID) controllers (Eurotherm) and thermocouple feedbacks. A W-Re (5-26% Re) thermocouple is spring-loaded to the recess of the crucible base. Each furnace is surrounded by multiple Ta radiation shields to improve both the temperature stability and thermal efficiency.

5.2.2 Preparation and Analysis Chamber

It is well known that the quality of substrates can influence the properties of films to a very large extent.[105] *In-situ* cleaning of the substrates, mainly by ion cleaning and heat treatment, is thus a very important stage in the MBE process. In addition, it is often useful to have surface analysis capabilities to check the quality of the substrates prior to growth, and also of the grown layers. Several *in-situ* cleaning and analytical instruments are housed in our preparation and analysis chamber. These include i) an ion cleaning unit comprising a VG LEG2 ion gun, Ar gas

line and several controlling valves; and ii) surface science equipment including two electron guns (one at normal and the other at glancing angle) and a retarding field analyzer based on 3-grid optics for LEED and Auger analysis. The chamber is pumped by a LN_2-trapped diffusion pump backed by a rotary pump (Edward Vacuum Ltd.). Secondary pumping is provided by a TSP situated at the bottom of the chamber. Samples are retained in an outgassing stage fitted to the end of a high precision manipulator (VG HPT205). The heating assembly is similar to that installed in the growth chamber. Sample transfer between the preparation chamber and the loadlock (i.e. from transfer rods "A" to "B" as shown in Fig. 5.1 and vice versa) takes place inside an intermediate chamber. This chamber is an extension of the preparation chamber and is isolated from the loadlock by a plate valve. It houses another high precision manipulator (Huntington PM-600-XYZT) where a saddle stage mounted with two substrate cups for parking samples is fitted.

5.2.3. Sample Introduction Chamber (Loadlock)

The loadlock comprises a low volume chamber with a rapid access entry lock. The chamber houses a K-cell outgassing port and a two-cup saddle stage which allows a total of three substrates to be loaded into the system at one time. Like the preparation chamber, the loadlock is also pumped by a diffusion pump unit.

5.3 System Operation

5.3.1 Attainment of UHV Conditions

After the MBE system was installed, a prolonged bakeout (230°C for 3 weeks) of the machine was carried out to ensure the elimination of residual solvents which were used for cleaning the stainless-steel chambers. The K-cells were then outgassed briefly in the outgassing port. Further outgassing of the K-cell crucibles (at 1300°C) was carried out in the growth chamber after the system has been baked for another week at 200°C. Finally, high purity sources were loaded into the K-cell and the whole system was baked for a further 10 days at around 200°C before it was ready for use. Ultrahigh vacuum with a base pressure in the low 10^{-11} Torr range is now routinely achieved throughout the whole system. The pressure of the growth

chamber often reaches the x-ray detection limit of the ionization gauge ($\leq 1 \times 10^{-12}$ Torr) when the cryopanels are filled with liquid nitrogen.

A residual gas analysis (Fig. 5.5) shows that at these low pressures the predominant species inside the growth chamber is H_2. In particular, residual hydrocarbon peaks are below the detection limit of the mass spectrometer (1×10^{-14} Torr). Traces of residual H_2O, CO and N_2 are also found. The latter comes mainly from the PBN crucibles during outgassing and is believed to have no deleterious effects on overlayer quality. [84]

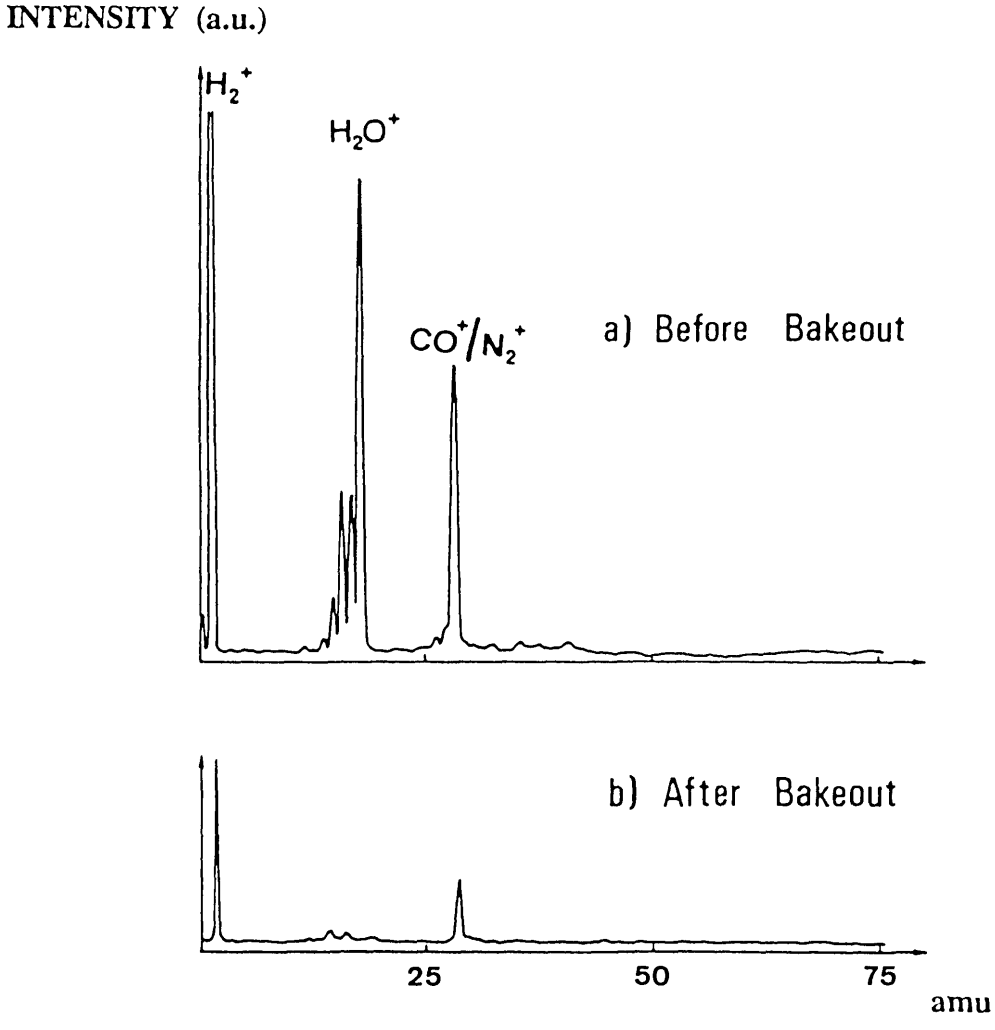


Fig. 5.5 Mass spectra showing the gaseous species inside the growth chamber a) before and b) after bakeout

5.3.2 Growth Procedures

For normal growth operations, the cryopanels are cooled to liquid nitrogen temperature. The Sn K-cell and substrate stage are then ramped to 50°C above the growth temperature (T_k) and 375°C respectively. They are kept at these temperatures for at least 2 hours while the substrates are being cleaned in the preparation chamber. This outgassing procedure is necessary in order to reduce the amount of carbon and oxygen in the growth region which may be detrimental to the overlayer quality. The cleaned substrate is then transferred to the growth chamber for a final annealing at around 275°C, after which a sharp (4x2) RHEED pattern can be observed. Growth can commence when the desired substrate temperature (T_s) is reached and the K-cell temperature and the corresponding beam equivalent pressure (BEP) is stabilized. During growth, the TSP, BMIG and mass spectrometer are all switched off to avoid contamination. When the growth sequence is completed, the sample is transferred back to the analysis chamber where its composition can be checked by the Auger technique.

Immediately after the sample is taken out from the MBE system, the Ga solder is stripped from the back surface of the substrate. The sample is etched in HCl with the surface protected by a layer of G-varnish which can later be removed by acetone. It is extremely important to strip off the Ga as soon as possible since it can creep up to the sample surface along the edges. Due to the high diffusion rate of Ga in Sn, the overlayer quality will easily be degraded in this way.

5.4 Growth Studies

In this section, the effect of growth conditions on the stability and quality of the α-Sn overlayers is examined. The specific growth parameters considered are substrate orientation, overlayer thickness, substrate temperature (T_s) and growth rate. The purpose of this study is to determine the optimum set of parameters for the growth of α-Sn films. The onset of α → β phase transition provides a convenient means of assessing the stability of the α-Sn overlayers. Since pure α and β-Sn are grey and white in colour respectively,[1] the α → β phase transition is accompanied by a colour change which can be easily detected. Fig. 5.6 is a real time recording of the phase

transformation observed through a Nomarski microscope. Note that β-Sn nucleated at defect sites (encircled in Fig. 5.6c) and the phase transformation was found to proceed by ledge propagation along the <110> directions (Fig. 5.6e). According to Asom *et. al.*,[42] the α → β phase transformation occurs by a martensitic lattice shear mechanism. The step-like motion of the interface is believed to be caused by the 26% volume difference between α and β-Sn. This produces a long-range tensile strain field which stalls the transformation when two parallel fronts approach each other (Fig. 5.6e). Reaction proceeds following a fluctuation which breaks the mirror symmetry and the two fronts eventually join at a corner (Fig. 5.7f). The highly faceted and step-wise motion of the α/β interface strongly suggests that the solid-solid transformation is diffusionless and, thus, martensitic.[42]

Information concerning the phase of the overlayer can also be determined from RHEED patterns. Due to the large decrease in volume associated with the α → β transition, well-ordered reconstruction patterns observed in epitaxial α-Sn films will become diffuse when β-Sn begins to form. In the extreme case, ring patterns characteristic of polycrystalline β-Sn can be observed.[5] The quality of the α-Sn layers can thus be assessed by the sharpness of the RHEED patterns.

The change of the Auger intensities of substrate and overlayer constituents with overlayer thickness can also provide information about the interfacial quality of the sample. Homogeneous film growth is characterized by an exponential decrease in the Auger intensity of all the substrate elements.[150] Any segregation or diffusion across the interface can thus be detected by analyzing the Auger composition profile. The peak-to-peak height of the Auger lines for Sn(430eV), In(410eV) and Sb(454eV) were taken as a measure of the intensity of the Auger transitions. Details of the Auger and RHEED techniques can be found in chapters 4 and 6 respectively and will not be repeated here.

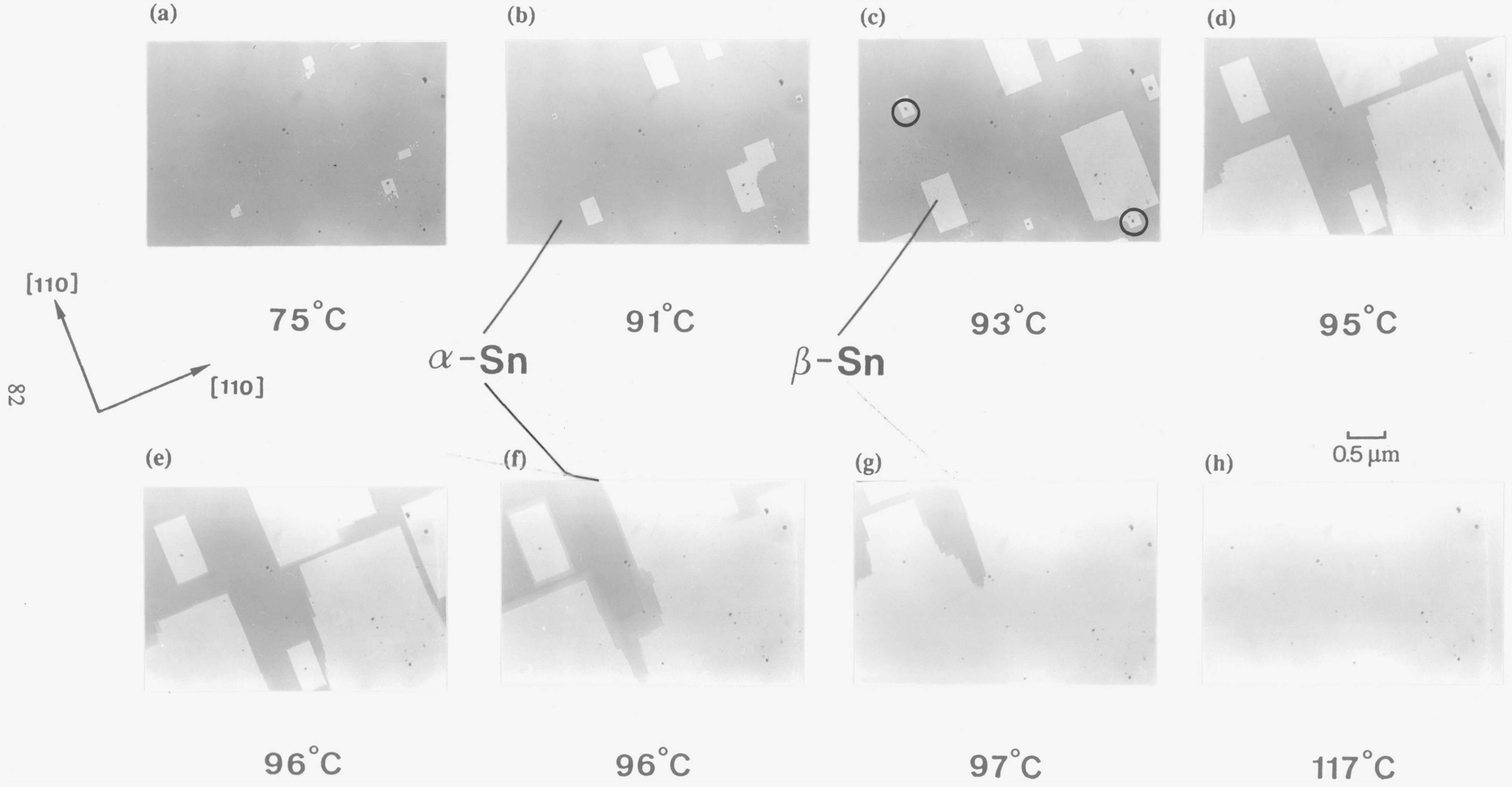


Fig. 5.6 Nomarski micrographs showing the time-dependent distribution of α and β-Sn (lighter colour) on an α-Sn/InSb sample undergoing heat treatment. Note that β-Sn always originate at defect sites and the α → β phase transformation proceeds by legde propagation along the <110> directions.

5.4.1 Effect of Substrate Orientations

Three InSb orientations : (100), (110) and $(\overline{111})$ were used in this study. All these substrates were subjected to the same cleaning procedure discussed in chapter 4. α-Sn layers were grown on each of the substrates at a growth rate of ~ 1.5Å/s (corresponds to BEP = 2×10^{-7} Torr, T_k= 1130°C) with the substrate kept at room temperature. α-Sn films grown on all three orientations were found to exhibit distinct thickness-dependent surface reconstructions. For the α-Sn/InSb(100) sample, two-domain (2x1), (2x2) and c(4x4) reconstructions as well as atomic step structures can be observed.[38] A detailed study on the structural properties of this system will be given in the next chapter. The RHEED patterns for the other two orientations are much simpler. Using the $(\overline{111})$ orientation, a bulk (1x1) pattern is observed for the first 20Å of growth and then a (3x3) structure takes over until the film thickness exceeds 1000Å. Further growth reduces the intensity of the 1/3-order streaks along the <211> azimuths and a (3x1) pattern begins to develop as the film thickness approaches 1200Å.[47] The observation of the (3x3) structure agrees with that reported by Kasukabe *et. al.*[46] but differs from the (1x1) structure observed by Höchst *et. al.*.[45] For the α-Sn/InSb(110) sample, the surface reconstruction changes from a (1x1) to a weak (2x1) structure for films thicker than 20Å. At some critical thickness, different for each orientation, the RHEED patterns become very diffuse and white specks of β-Sn can be observed on the sample surfaces. The variation of critical thickness with substrate orientation is summarized in Table 5.1.

TABLE 5.1

Sample	InSb Substrate Orientation	Maximum Overlayer Thickness (Å)
Sn-42p	(100)	4000
Sn-31p	$(\overline{111})$	1500
Sn-53p	(110)	200
Growth conditions : T_s = 25°C, G.R. ≃ 0.6 Å/s		

Note that the onset of $\alpha \rightarrow \beta$ transitions was judged visually and these results may therefore not be conclusive quantitatively. However, they do indicate that α-Sn films grown on InSb(100) are much more stable and much thicker films can be grown in this orientation. InSb(100) substrates will thus be used exclusively in the following studies.

5.4.2. Effect of Overlayer Thickness

Another parameter that can affect the stability of the α-Sn film is the overlayer thickness. A series of α-Sn films was grown on InSb(100) substrates under the same conditions (T_s = 25°C, growth rate ≃ 0.6Å/s) except for the overlayer thickness. In all cases, the RHEED patterns of the samples remained sharp and well-ordered when the desired thicknesses were reached. Overlayer thickness was determined by an *ex-situ* method. Thin sheets of tantalum were spot-welded onto the edge of the substrate blocks to produce a step on the grown layer. This step height, which is equivalent to the overlayer thickness, was then measured by a talystep. In order to determine the transition temperature of the α-Sn films, the sample were heated inside a Bio-Rad Polaron reaction chamber. Temperature calibration was checked against the melting point of In. The samples were gradually heated to 50°C in about 10 mins., after which the heating rate was reduced to ~ 1°C/min.. The sample surfaces were constantly monitored with an optical microscope. Since the $\alpha \rightarrow \beta$ phase transition is accompanied by a colour change, the transition temperature can be found easily. Using different pieces from the same sample, the transition temperature determined in this way was reproducible to within 3°C.

The results listed in Table 5.2 show that thinner samples have a higher transition temperature than thicker ones. Such behaviour is expected since the substrate-stabilization effect which raises the transition temperature of α-Sn films beyond the bulk value of 13.2°C will be reduced as the overlayer thickness increases. This trend has also been observed in α-Sn films grown on CdTe substrates.[58] The higher transition temperature attainable in thinner films offers the possibility of growing α-Sn/InSb superlattices that would be stable enough for device applications.

TABLE 4.2

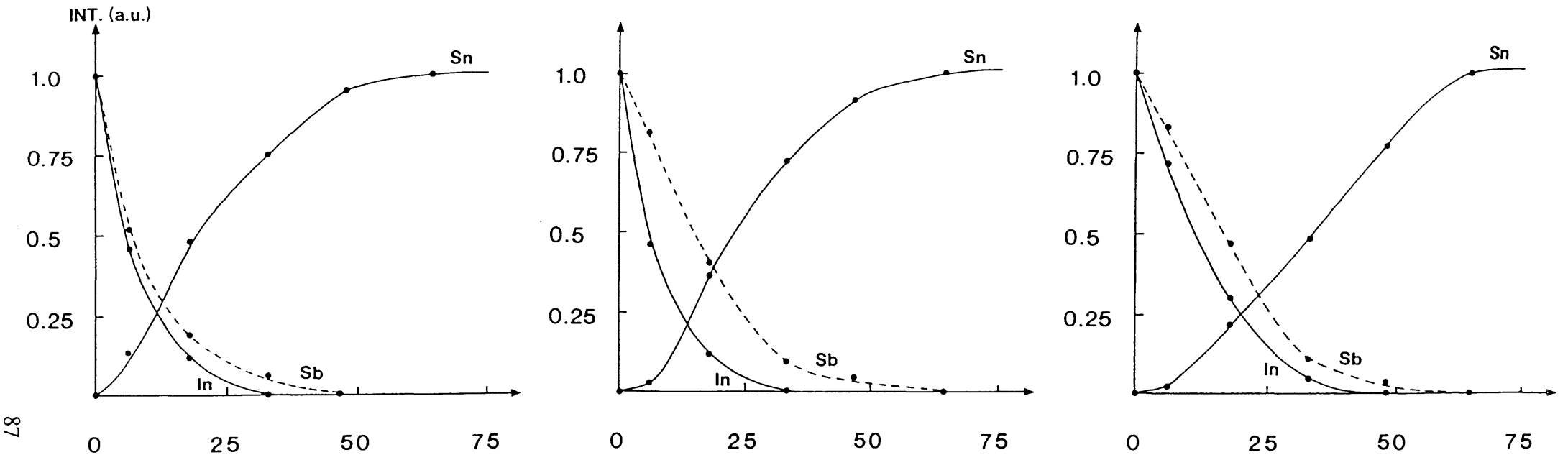
Sample	Overlayer Thickness (Å)	$\alpha \rightarrow \beta$ Phase Transition Temperature ($^{\circ}$C)
Sn-48p	200	132
Sn-39p	1500	106
Sn-35p	2000	97
Sn-41p	3000	94
Sn-42p	4000	93
Growth conditions : T_s = 25°C, G.R. $\simeq$ 0.6 Å/s		

5.4.3. Effect of Substrate Temperature and Growth Rate

While observing the $\alpha \rightarrow \beta$ phase transformation under the microscope, it was noticed that β-Sn originated at defect sites in the film as previously reported by other workers.[5,34,58] It was therefore reasonable to expect that if the number of such defects could be lowered, the transition temperature should increase. From double crystal X-ray diffraction measurements, Satoh and Kimata[34] concluded that the quality of α-Sn films could be improved by using an elevated substrate temperature for growth. Reno and Stephenson[58] also reported that the quality of their α-Sn films grown on CdTe substrates could be increased by raising the substrate temperature to about 75°C and lowering the growth rate. In order to test this theory on the α-Sn/InSb(100) system, several samples were grown using different growth rates and substrate temperatures. Growth rates were inferred from the measured thickness of the overlayers and the growth time. Rates ranging from 0.35Å/s to 1.5Å/s could be achieved by varying the K-cell temperature from 1080 to 1130°C (corresponding to BEP values of 1.2 to 2.1 x 10^{-7} Torr). The substrate temperatures quoted in this work were readings from the thermocouple attached to the substrate heating block. Note that the lowest substrate temperature actually attainable in this system is about 25°C due to radiation from the K-cell. Coherent α-Sn films (with no noticeable ß-Sn specks) thicker than 1500Å can be grown at substrate temperatures as high as

200°C. Judging from the sharpness of the RHEED patterns observed in films more than 1500Å thick, higher surface quality was indeed achieved using elevated temperatures and low growth rate. Under these conditions, surface ordering and flatness were improved due presumably to the enhanced surface migration of surface adatoms.

Another factor affecting the interfacial quality of the α-Sn/InSb layers can be seen from the Auger composition profiles shown in Fig. 5.7. With the substrate set at 15°C, the Auger intensities of both In and Sb were found to decrease exponentially (Fig. 5.7a). On the other hand, a much slower decrease of the Sb signal with respect to that of In was observed in the sample grown at 100°C (Fig. 5.7b). This deviation is believed to be the result of a preferential diffusion of Sb into the α-Sn overlayer.[150] Note that the Sb signal is detectable for Sn coverages up to ~ 60Å at this temperature. Sb diffusion was found to be more severe (i.e. the decay of the Sb signal is slower) when even higher substrate temperatures were used. Similarly, the composition profiles were found to vary with growth rate (compare Figs. 5.7a and c). However, within the range of growth rates used in this study, the difference is much less than that observed by varying the substrate temperature. In addition, the reduction of the Sb signal as well as the rise of the Sn signal were found to be more gradual when a slower growth rate was used. In general, lowering the growth rate would cause a larger amount of Sb diffusion into the overlayer. In terms of interface quality, therefore, low substrate temperature and moderate growth rate is preferred. At first sight, this seems to contradict the RHEED results discussed previously. However, it should be noted that the RHEED technique was used to assess the surface quality of relatively thick films (≥ 1500Å) whereas the Auger composition profiling analysis yielded information regarding the interfacial quality of the α-Sn/InSb sample (overlayer thickness ≤ 100Å).



a) T_s = 15°C, G.R. = 0.6Å/s (BEP = 2.1×10^{-7} Torr)

b) T_s = 100°C, G.R. = 0.6Å/s

c) T_s = 15°C, G.R. = 0.35Å/s (BEP = 1.2×10^{-7} Torr)

Fig. 5.7 Auger composition profiles showing the change in overlayer (Sn) and substrate (In and Sb) signals with respect to overlayer thickness for three different growth conditions

5.4.4 Conclusions

The effect of growth conditions on the quality and stability of α-Sn films grown on InSb was examined. The growth of α-Sn films thicker than 1500Å can only be sustained on InSb substrates with the (100) orientation. The α → β phase transition temperature, used as a measure of the stability of the α-Sn film, shows a dependence on the overlayer thickness. Thinner films were found to have a higher transition temperature than thicker ones. β-Sn was found to originate from defect sites and the phase transition proceed by ledge propagation along the <110> directions. The surface quality of α-Sn films was found to be improved by lowering the growth rate and raising the substrate temperature for growth due to enhanced migration of surface adatoms. This in turn should increase the phase transition temperature of the films. On the other hand, significant diffusion of Sb into the α-Sn overlayer was detected in samples grown at slow growth rates and high substrate temperatures. Therefore, in the growth of α-Sn/InSb, there exists an optimum combination of growth rate and substrate temperature due to the competing effects of surface ordering and Sb diffusion. In our case, growth rates in the range of 0.5 - 0.7Å/s and substrate temperatures between 10 to 50°C will produce a well-ordered α-Sn film without any significant Sb diffusion. The transition temperature of such films were found to be higher than 90°C even for films as thick as 3500Å. This set of growth conditions will be used exclusively in all subsequent work.

CHAPTER 6 STRUCTURAL PROPERTIES OF α-Sn : A RHEED STUDY

6.1 Introduction

The classic experiments of Davisson and Germer[151] (1927) on the diffraction of low energy electrons and the almost simultaneous demonstration by Thomson and Reid[152] of the diffraction of high energy electrons transmitted through thin foil laid the foundation for electron diffraction techniques employed in the examination of surfaces and thin films. Reflection high energy electron diffraction (RHEED) was first demonstrated by Nishikawa and Kikuchi[153] in 1928 when diffraction was obtained from the surface of a calcite crystal using a beam of high energy electrons at grazing incidence. These early work verified the wave-particle nature of electrons as postulated by de Broglie in 1924.[154]

This chapter starts with a brief review on some simple electron diffraction theories and the RHEED technique. Diffraction patterns are analyzed using a purely kinematic treatment based on Ewald's sphere and reciprocal lattice concepts. The importance of multi-azimuthal analysis is also explained. RHEED patterns recorded at various stages of α-Sn growth are presented and the structural information extracted is discussed. Finally, the structure of the α-Sn(100) surface is compared with that of the well known Si(100) surface and a growth model is proposed for the α-Sn/InSb(100) system.

6.2 Fundamentals of RHEED

Electron diffraction techniques are based on the wave nature of electrons and their strong interaction with matter. Incorporating the relativistic correction, the wavelength associated with electrons with energy E in vacuum is given by :

$$\lambda = \frac{h}{\sqrt{2m_o eE\left(1 + \frac{eE}{2m_o c^2}\right)}} \qquad (6.1a)$$

where m_o is the electron rest mass, e the electronic charge, h the Planck's

constant and c the speed of light. Numerically,

$$\lambda = \frac{12.26}{\sqrt{E\,(\,1 + 0.9788 \times 10^{-6}\,E\,)}} \qquad (6.1b)$$

where λ is in Å and E in eV. In RHEED, the energy of the electrons is typically between 5 to 100 keV. This corresponds to wavelengths between 0.17 to 0.037 Å which are much smaller than the lattice spacing of typical semiconductor crystals.

A typical experimental RHEED system is shown schematically in Fig. 6.1. A beam of high energy electrons is directed towards the crystal surface at grazing incidence (usually 1-3°). Since the incident electron momentum normal to the surface is very small, the diffraction pattern observed on the fluorescent screen will be characteristic of the surface atomic structure. The RHEED technique is thus extremely useful for continuous assessment of the surface during growth because of its favourable grazing incidence geometry and non-destructive nature. Information obtainable from RHEED analysis includes :

1) symmetry and periodicity of the surface layer (from the existence and location of diffraction spots or streaks).
2) surface structure and topography including defects and disorders (from the geometries of the diffraction features).
3) position of the atoms within the unit cell (from the intensity distribution within the diffraction pattern).

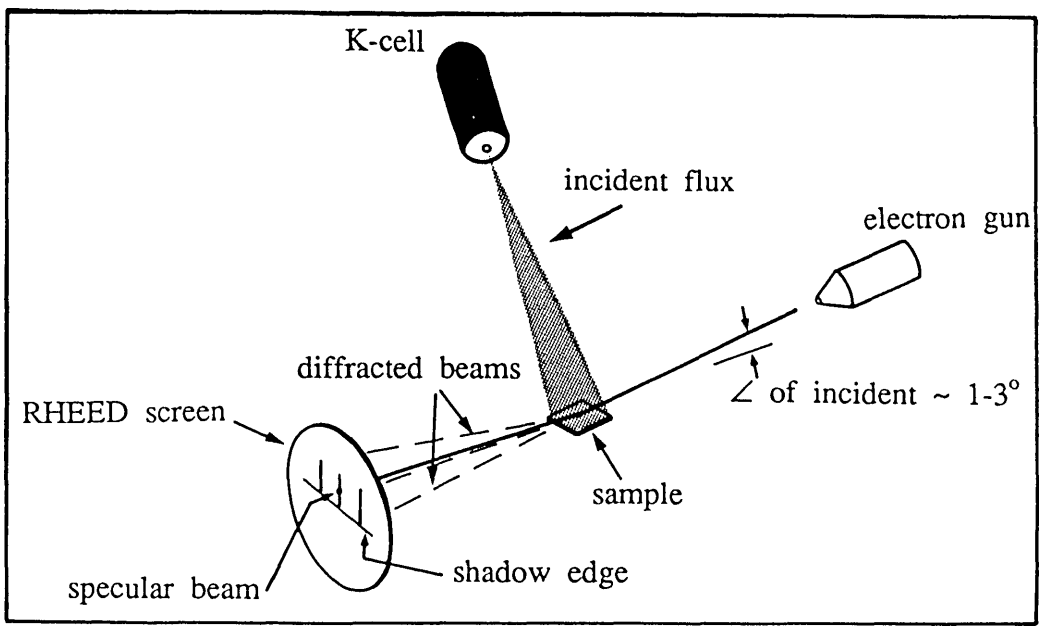


Fig. 6.1 Schematic diagram of a typical experimental RHEED system

6.2.1 Geometric Theory

In this section, reflection electron diffraction of a plane wave by a single crystal is discussed using only geometric considerations and neglecting the interaction mechanism between the wave and the crystal.

When a plane wave with wave-vector $\mathbf{k}_o$ is incident on the parallel planes of atoms in a crystal, constructive interference of diffracted beams from successive planes occurs when the Bragg condition :

$$2d\sin\vartheta = n\lambda \qquad (6.2)$$

is satisfied. Here d is the interplanar distance, ϑ the angle of incidence and n is an integer.

6.2.2 Reciprocal lattice and Ewald's Sphere Construction

In the discussion of periodic structures, it is useful to introduce the ideas of reciprocal space and reciprocal lattice which are representations of the spatial properties of a crystal in Fourier space.[96] For a perfect single crystal which is a three-dimensional (3-D) repetition of identical building blocks, the corresponding reciprocal lattice is an infinite periodic 3-D array of points whose spacings are inversely proportional to the distances between planes in the real lattice.

If **a**, **b** and **c** are the primitive translational vectors of a space lattice in real space, the corresponding primitive vectors in the reciprocal space can be defined as :

$$\mathbf{a}^* = 2\pi\frac{\mathbf{b}\times\mathbf{c}}{\mathbf{a}\cdot\mathbf{b}\times\mathbf{c}} \qquad \mathbf{b}^* = 2\pi\frac{\mathbf{c}\times\mathbf{a}}{\mathbf{a}\cdot\mathbf{b}\times\mathbf{c}} \qquad \mathbf{c}^* = 2\pi\frac{\mathbf{a}\times\mathbf{b}}{\mathbf{a}\cdot\mathbf{b}\times\mathbf{c}} \qquad (6.3)$$

which satisfy the relations :

$$\left.\begin{aligned}\mathbf{a}\cdot\mathbf{a}^* = \mathbf{b}\cdot\mathbf{b}^* = \mathbf{c}\cdot\mathbf{c}^* = 2\pi \\ \mathbf{a}\cdot\mathbf{b}^* = \mathbf{b}\cdot\mathbf{c}^* = \mathbf{c}\cdot\mathbf{a}^* = \mathbf{a}\cdot\mathbf{c}^* = 0\end{aligned}\right\} \qquad (6.4)$$

Provided that scattering is elastic so that there is no change in the magnitude of the wave-vector, the Bragg condition can be rewritten as :

$$\Delta \mathbf{k} = \mathbf{k} - \mathbf{k}_o = \mathbf{G}_{hkl} \qquad (6.5)$$

where $\mathbf{k}$ and $\mathbf{k}_o$ are the diffracted and incident wave-vectors, and $\mathbf{G}_{hkl} = h\mathbf{a}^* + k\mathbf{b}^* + l\mathbf{c}^*$ is a reciprocal lattice vector perpendicular to the (hkl) plane. This gives rise to the well known Laue conditions for diffraction :

$$\mathbf{a}\cdot\Delta\mathbf{k} = 2\pi h \qquad \mathbf{b}\cdot\Delta\mathbf{k} = 2\pi k \qquad \mathbf{c}\cdot\Delta\mathbf{k} = 2\pi l \qquad (6.6)$$

It is thus possible to envisage a geometrical construction in reciprocal space which would simulate the diffraction process. Suppose the wave-vector $\mathbf{k}_o$ of the incident beam is drawn as a vector which terminates at a reciprocal lattice point denoted as the origin of the reciprocal space. From the other end of $\mathbf{k}_o$, a sphere can be drawn with radius $|\mathbf{k}_o| = 2\pi/\lambda$. Whenever a reciprocal lattice point intersects the surface of this sphere, the Bragg condition for elastic scattering (Eqn. 6.5) is satisfied and diffraction occurs. The scattered beam is represented by the wave-vector $\mathbf{k}$ as shown in Fig. 6.2. This construction, known as the Ewald's sphere construction will be used extensively for interpreting diffraction patterns in the following sections.

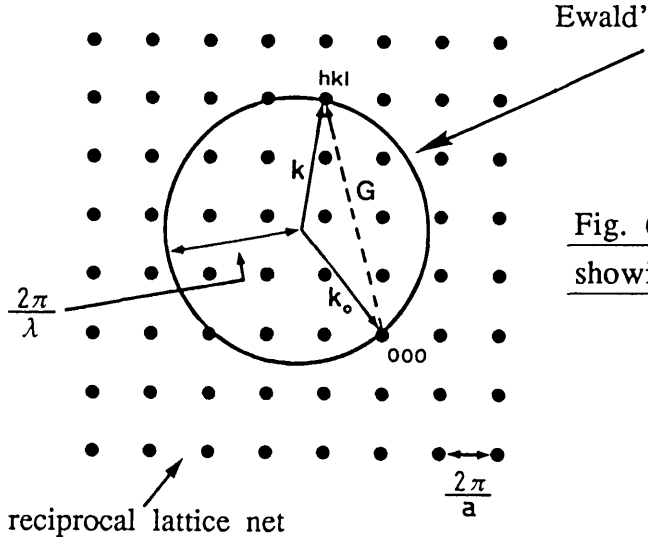


Fig. 6.2 Ewald's sphere construction showing the Bragg diffraction condition

6.2.3 General Diffraction Theory

Most of the existing theories of electron diffraction are based on the general scattering formalism with varying degrees of approximations. The incident and scattered electrons are represented by plane and spherical waves respectively. The mutual interaction between the incident electrons

and the crystal can be described by an effective crystal potential $U(\mathbf{r})$ and a differential equation of the form :[96]

$$[\nabla^2 + \mathbf{k}^2 - U(\mathbf{r})]\ \Psi(\mathbf{r}) = 0 \qquad (6.7)$$

In electron diffraction, only the values of $\Psi(\mathbf{r})$ where the distance $|\mathbf{r}|$ is large compared to the dimensions of the crystal are considered. In terms of the incident plane wave $\Psi_o = e^{i\mathbf{k}_o\cdot\mathbf{r}}$, Eqn. 6.7 can be written in an integral form :

$$\Psi(\mathbf{r}) = e^{i\mathbf{k}_o\cdot\mathbf{r}} - \frac{e^{i\mathbf{k}r}}{\mathbf{r}}\ \frac{1}{4\pi}\int e^{i\mathbf{k}\cdot\mathbf{r}'}\ U(\mathbf{r}')\ \Psi(\mathbf{r}')\ d\mathbf{r}' \qquad (6.8)$$

i.e. the scattered wave can be considered as a spherical wave with a complex scattering amplitude $f(\mathbf{k})$ given by :

$$f(\mathbf{k}) = -\frac{1}{4\pi}\int e^{-i\mathbf{k}\cdot\mathbf{r}'}\ U(\mathbf{r}')\ \Psi(\mathbf{r}')\ d\mathbf{r}' \qquad (6.9)$$

6.2.4 Kinematic Theory

In the kinematic theory, it is assumed that the scattered wave amplitude is much smaller than that of the incident wave. The wave function $\Psi(\mathbf{r})$ in Eqn. 6.8 can therefore be approximated by the incident wave (Born approximation) and the scattering amplitude can be written as :[96]

$$f(\Delta\mathbf{k}) = -\frac{1}{4\pi}\int e^{-i\Delta\mathbf{k}\cdot\mathbf{r}'}U(\mathbf{r}')\ d\mathbf{r}' \qquad (6.10)$$

with $\Delta\mathbf{k} = \mathbf{k} - \mathbf{k}_o$. Therefore under the kinematic approximation, the scattering amplitude is the Fourier transform of the effective crystal potential.

For a crystal with translational vectors **a**, **b** and **c**, the presence of crystal symmetry can further simplify Eqn. 6.10 into :

$$f(\Delta\mathbf{k}) = \underbrace{-\frac{1}{4\pi}\int e^{-i\Delta\mathbf{k}\cdot\mathbf{r}'}U(\mathbf{r}')\ d\mathbf{r}}_{F(\Delta\mathbf{k})} \cdot \underbrace{\sum_{m=0}\sum_{n=0}\sum_{v=0} e^{-i\Delta\mathbf{k}(m\mathbf{a}+n\mathbf{b}+v\mathbf{c})}}_{G(\Delta\mathbf{K})}$$

$$\Rightarrow\ f(\Delta\mathbf{k}) = F(\Delta\mathbf{k}) \cdot G(\Delta\mathbf{K})$$

or

$$|f(\Delta\mathbf{k})|^2 = |F(\Delta\mathbf{k})|^2 \cdot |G(\Delta\mathbf{k})|^2 \qquad (6.11)$$

where m,n,v are integers and the integral is over a unit cell.

$|F(\Delta\mathbf{k})|^2$ is called the 'structure factor' which contains all information on the scattering properties of a single atom. $|G(\Delta\mathbf{k})|^2$, known as the 'lattice factor', is just due to the repetition of identical units. Under the Bragg condition of constructive interference (Eqn. 6.5), the lattice factor has appreciable values only around a reciprocal lattice point. In addition, since $|F(\Delta\mathbf{k})|^2$ varies only slowly with $\Delta\mathbf{k}$ as compared to $|G(\Delta\mathbf{k})|^2$, the existence of a diffraction feature and its geometry can be completely explained by the lattice factor.[155,156] On the other hand, the intensity of the diffraction features and hence the content of the unit cell may not be interpreted without the evaluation of $|F(\Delta\mathbf{k})|^2$. Since this 'structure factor' describes the outgoing waves, it also has to include the effect of multiple scattering. This effect is unaccounted for in the kinematic theory which is based on the assumption that the interaction between electrons and the crystal is weak. Therefore, a more advanced dynamic theory is required for the quantitative interpretation of RHEED intensities. Since we are only interested in the structural properties of the surface, all the discussions that follow will be exclusively concerned with the geometric aspects of the RHEED patterns which can be interpreted within the kinematic approximation framework.

6.3 Multi-azimuthal Analysis

In order to obtain unambiguous information on the overall surface structure from RHEED, it is important to analyze the diffraction patterns at several different azimuths. The need for such a multi-azimuthal analysis is supported by the following arguments :

1) Diffraction streaks are the most prominent features observed in RHEED patterns arising from single crystal semiconductor surfaces. Very often these streaks exhibit very little or no modulation along their lengths.[157] This makes it extremely difficult to determine the surface symmetry completely and unambiguously from one single azimuth. For example, (2x1), 2-domain (2x1), (2x2), c(4x2) and c(4x4) reconstructions on a (100) surface will all produce integral and 1/2-order streaks in the first Laue zone along the [110] azimuth. In the case of 2-domain (2x1), (2x2) and c(4x4) structures, all of which exhibit a 2x pattern along the orthogonal [$\bar{1}$10] azimuth, a third

azimuth is needed to distinguish them (refer to Fig. 6.4 in § 6.4.1).

2) 1-D disorder boundaries (depending on its orientation with respect to the incident beam) can give rise to curved diffraction streaks in certain azimuths whereas only a homogeneous increase in the background intensity can be found in others.[157] This effect will be demonstrated in § 6.4.3. This led Joyce *et. al.*[157] to conclude that any 1-D or 2-D disorder in the surface can only be detected and analyzed by using several azimuths.

3) Neave and Joyce[158] pointed out that a streaked pattern in a given azimuth is only a necessary but not sufficient condition to define a smooth surface. A classical example is given by a (4x2) GaAs surface grown with excess Ga flux. Whereas the streaked pattern along [1$\bar{1}$0] suggests a comparatively flat surface, the orthogonal [11̄0] diffraction pattern reveals slanted streaks and extra reflections from twins.[158] Therefore, analysis of RHEED pattern at a single azimuth can produce misleading information on the topography of the surface.

Based on the analysis of diffraction features belonging to intermediate Laue zones, Hernández-Calderón and Höchst[35] claimed that one single RHEED pattern along a given azimuth can provide enough information to determine in a definite way the reconstruction of the surface. This seems to contradict the multi-azimuthal arguments mentioned above. However, it should be noted that the separation between Laue zones may be very large (depending on the lattice spacing and the energy of the electrons) and the intensity of the diffraction features in fractional-order Laue zones is often very weak. This means that it may be quite difficult to record these features through the fluorescent screen for analysis and thereby hamper the usefulness of their method.

6.4 Interpretation of RHEED Patterns

In this section, we will show how information on surface morphology, disorder and topography can be extracted from RHEED patterns through a simple extension of the reciprocal lattice-Ewald's sphere construction. The importance of multi-azimuthal analysis will also be pointed out in the relevant sections.

6.4.1. Streak Patterns

The origin of streaks in diffraction patterns is still very controversial. Qualitatively, it is generally believed that streaked patterns are indicative of a flat, well-defined single crystal surface.[105] Streaking is also enhanced by refraction of the electron beam as it enters into the crystal at low angles.[105] There are some workers who believe that streaks occur in crystals that exhibit a considerable degree of 1-D disorder which may be produced by stacking faults or can be found in layer lattices.[96,159] Such defects cause extension of reciprocal lattice points in the direction perpendicular to the fault plane and produce more or less continuous streaks in RHEED patterns. Alternatively, it has been proposed that poorly collimated and mononchromatized electron beam can result in streaked patterns.[160] On the other hand, these streaks must have an intrinsic origin if they are to be observed from a perfect surface using an ideal instrument. There are sound theoretical reasons (though not substantiated experimentally) for believing that streaks may arise from a thermal diffuse scattering mechanism.[161] In considering real surfaces, the observation of streaked patterns can be readily explained using the reciprocal lattice-Ewald's sphere construction. Any contribution to streaking from the non-ideality of the instrument is assumed to be small.

Under conditions of grazing incidence employed in RHEED, the periodicity along the surface normal is lost and the reciprocal lattice becomes a 2-D set of infinitely long rods normal to the surface, i.e. the third Laue condition is relaxed.[157,162] Since the radius of the Ewald's sphere (~ $40Å^{-1}$ at 5keV used in our system) is large compared with the reciprocal lattice spacings (~ $1Å^{-1}$ for the (100) surfaces of InSb and α-Sn), it will cut the reciprocal lattice rods along their length as indicated in Fig. 6.3a. The RHEED patterns of a flat surface will therefore consist of short, intense and well-defined streaks normal to the shadow edge of the sample. It should be noted that if there are any asperities on the surface, the electron beam will be diffracted by the 3-D atomic arrangement within these asperities. As a result, a series of discrete spots will be seen in the diffraction patterns.

It is well known that semiconductor surfaces undergo reconstructions for energy minimization purpose. Surface reconstructions can be determined

by measuring the separation of streaks in the RHEED patterns.[35] As illustrated in Fig. 6.3, the intersection of each row of reciprocal rods perpendicular to the incident beam will be projected on a screen over arcs of circumference - the **Laue zones**. With the incident beam parallel to $\mathbf{b}^*$ (as shown in Fig. 6.3b), the separation between streaks on the same Laue zone will give information of the periodicity in the orthogonal $\mathbf{a}^*$ direction. Since a^*, $b^* \ll |\mathbf{k}_o|$, the following relation can be obtained from the geometry of Fig. 6.3b :

$$a \cdot t = L \cdot \lambda \tag{6.12}$$

where $a = 2\pi/a^*$ is the interatomic in real space, L is the camera length of the RHEED system and $\lambda = 2\pi/|\mathbf{k}_o|$ is the wavelength of the incident electrons. To obtain the periodicity along $\mathbf{b}^*$, the same procedure can be used to analyze the RHEED pattern recorded with the incident beam parallel to $\mathbf{a}^*$. Alternatively, this periodicity can be determined from the separations between different Laue zones.[35] From Fig. 6.3, the distance b^* in reciprocal space between the 00 rod and any given rod can be calculated by using :

$$b^* = \frac{2\pi}{\lambda} \left\{ \cos\vartheta - \left[\left(\frac{D}{L} - \tan\vartheta \right)^2 + 1 \right]^{-1/2} \right\} \tag{6.13}$$

where D is the distance between the incident spot I and the projection of a given rod on the screen. Different kinds of surface reconstructions can thus be distinguished by comparing these interatomic distances with that of the ideal unreconstructed surface.

The real space and reciprocal space representations for several surface reconstructions relevant to the α-Sn/InSb(100) system are shown in Fig. 6.4. In the same diagram, schematics of the theoretical RHEED patterns expected from these reconstructions are also shown for the [1$\bar{1}$0], [100] and [110] azimuths and the results are summarized in Table 6.1.

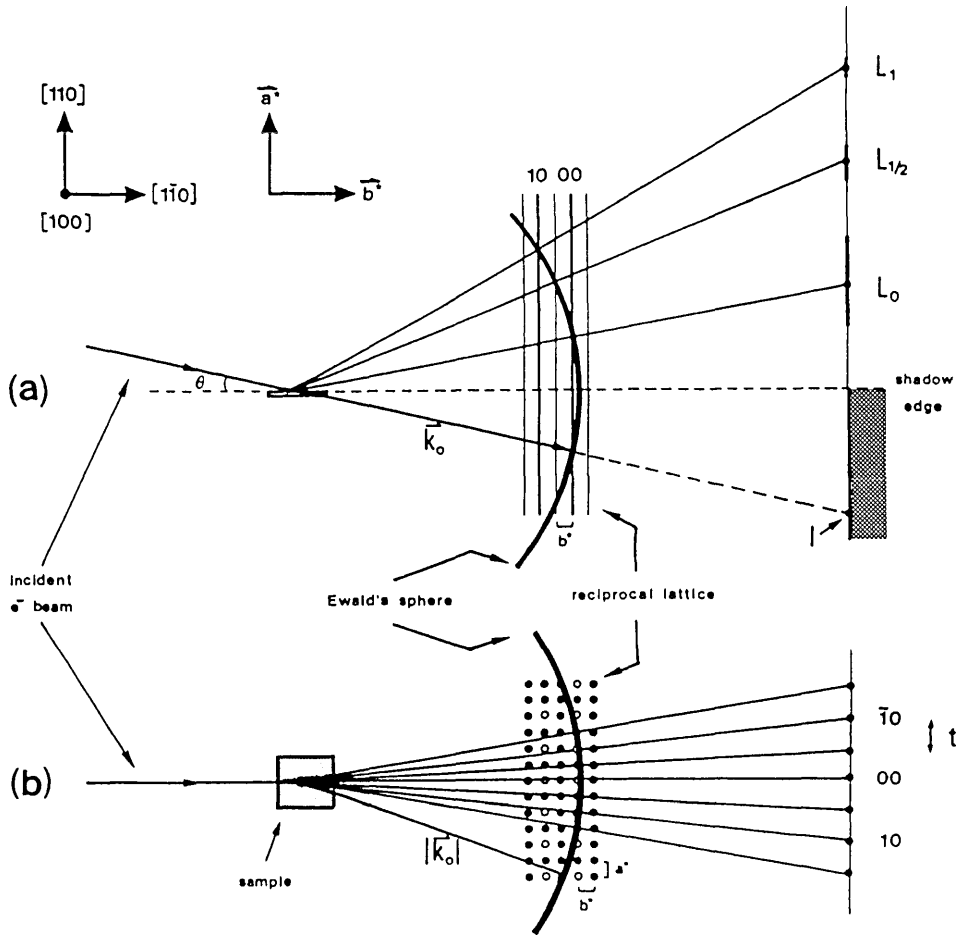


Fig. 6.3 Schematic diagrams illustrating the correlation between the reciprocal lattice and the observed RHEED patterns (from Ref. 35)

TABLE 6.1

Reconstructions	Azimuths		
([1$\bar{1}$0] x [110])	[1$\bar{1}$0]	[100]	[110]
(4x2)	2	2	4
c(8x2)	1	2	4
two-domain (2x1)	2	1	2
two-domain c(4x2)	2	1	2
(2x2)	2	2	2
c(2x2)	1	2	1
c(4x4)	2	4	1

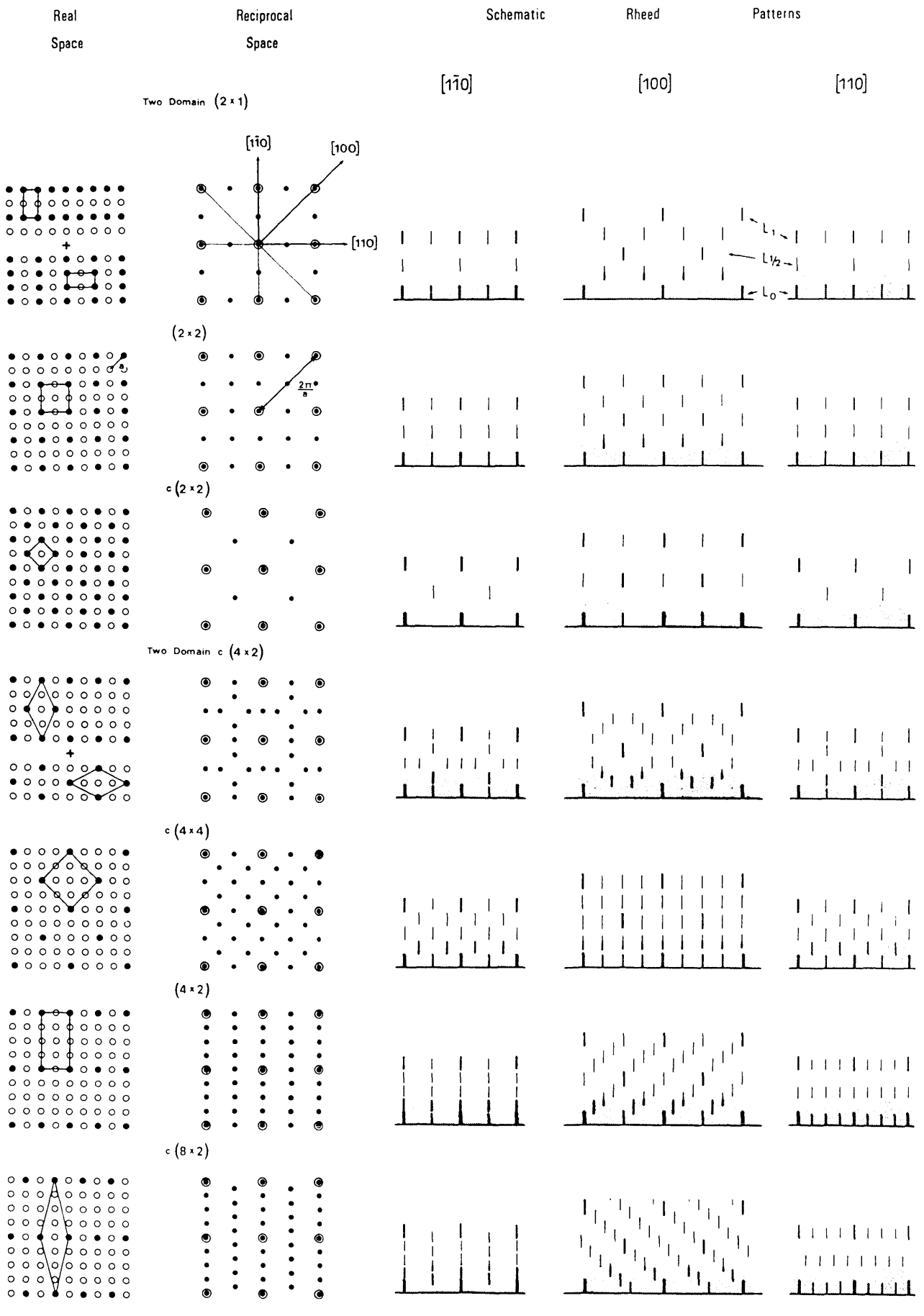


Fig. 6.4 Schematic RHEED patterns and the corresponding real and reciprocal space representations for surface reconstructions relevant to the α-Sn/InSb(100) system

(A solid circle represents a surface atom and an open circle represents a bulk atom)

(RHEED patterns which can be observed from our system are shaded)

6.4.2 Streak Broadening and Lengthening

The Fourier relationship between real and reciprocal space means that any lack of perfect ordering in a particular direction which restricts the average size of the ordered regions on the crystal surface will lead to the reciprocal lattice rod becoming two-dimensional, forming solid ellipsoidal cylinders.[157] The case where the domains are extensive in one direction and restricted in the orthogonal one is illustrated in Fig. 6.5. With the electron beam along the short domain side, the diffraction streaks are long and narrow (Fig. 6.5a). When the beam is parallel to the long domain side, short and broad streaks are produced (Fig. 6.5b). This situation occurs in clean InSb(100) surfaces where (4x2) and c(8x2) domains can co-exist and will be discussed in detail in § 6.5.2a (see Figs. 6.9 and 6.10).

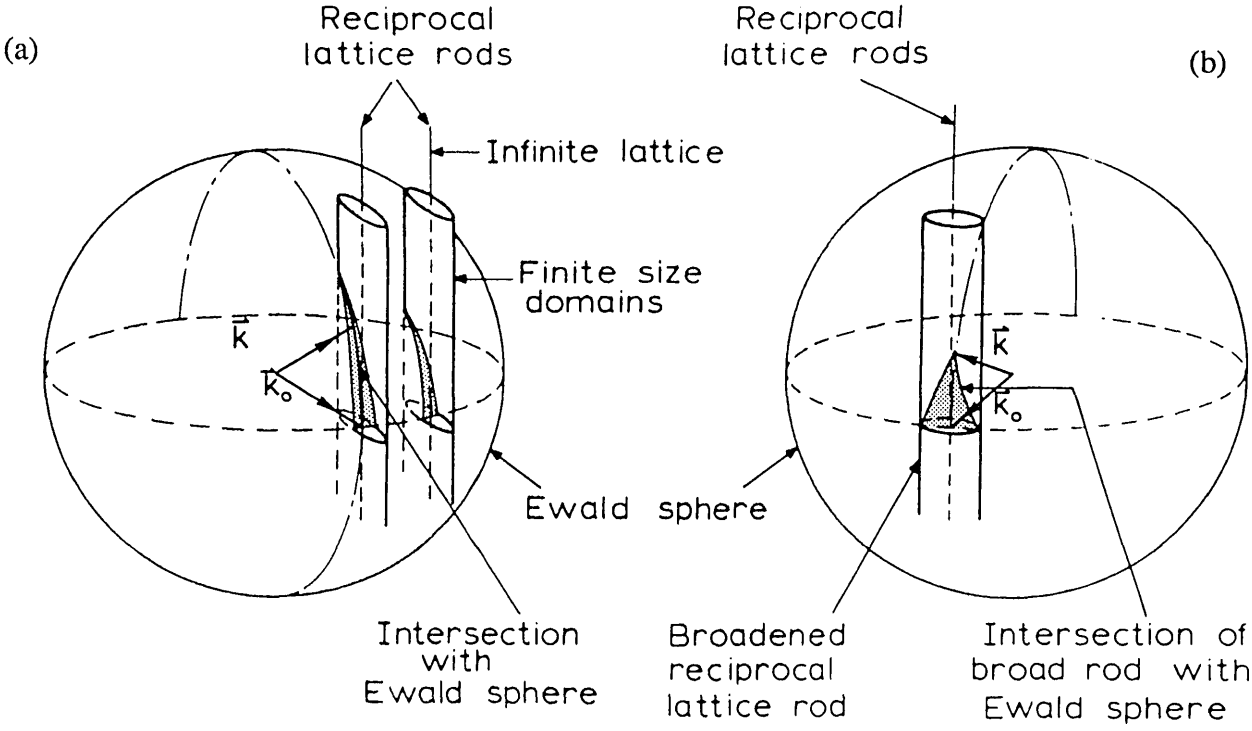


Fig. 6.5 Reciprocal space - Ewald sphere construction showing the broadening and lengthening of diffraction streaks (from Ref. 157)

6.4.3 Curved Streaks

Curved streaks in diffraction patterns may arise from randomly distributed 1-D features which can be caused by domain boundaries between co-existing structures randomly dispersed on the surface. In reciprocal space, these boundaries give rise to 2-D planes. Projections of the

intersections of these disorder planes with the Ewald's sphere onto the RHEED screen will generate curved diffraction streaks in the appropriate directions. For example, the co-existence of (4x2) and c(8x2) domains, commonly observed in GaAs(100) surfaces, produces curved streaks along <100> at the 1/2-order positions. It is important to note that the directions of the curved streaks depend not only on the orientations of the 2-D planes, but also the direction of the incident electron beam (Fig. 6.6). For instance, plane A along [110] can generate streaks along [100] and [010] curving in opposite directions. On the other hand, when the electron beam is parallel to the disorder boundaries (i.e. along <110>), the reciprocal lattice plane is tangential to the Ewald's sphere and only an increase in background intensity can be observed. Thus the directions of the curved streaks along different azimuths can, unambiguously, indicate the orientation of the 1-D disorder boundaries in real space and the need for multi-azimuthal analysis is clearly demonstrated. The co-existence of (4x2) and c(8x2) domains in InSb(100) surfaces will be discussed in § 6.5.2 where examples of such curved streak patterns will be shown in Fig. 6.9.

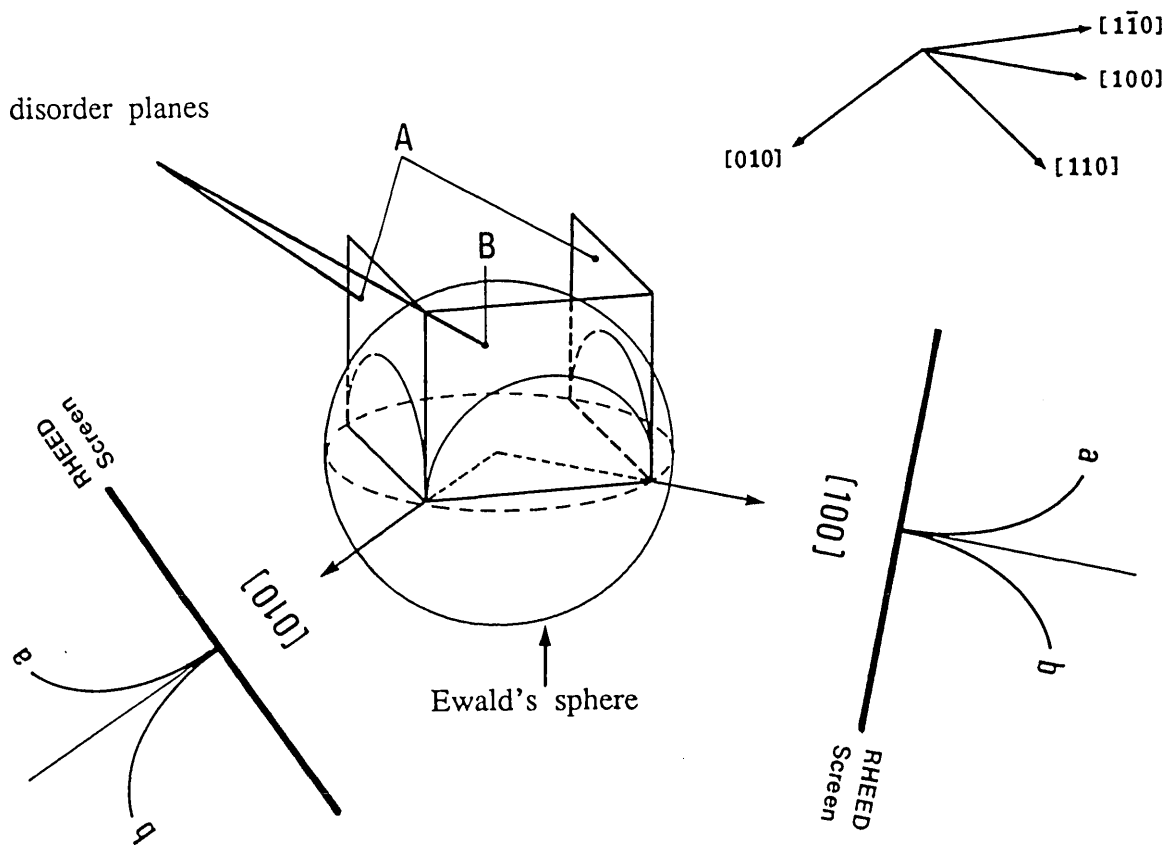


Fig. 6.6 Reciprocal space - Ewald sphere construction showing the origin of curved diffraction streaks

6.4.4 Split or Modulated Streaks

The existence of an ordered array of atomic steps forming a vicinal surface is revealed by the modulation and/or splitting of the diffracted beams in a form characteristic of the orientation and spacing of the steps. The effect of step array on diffraction patterns has been analyzed extensively by Hottier *et. al.* (RHEED)[163] and Henzler (LEED).[164]

The periodic structure of a vicinal surface can be considered as the convolution of a single diffracting unit (one step) by a periodic function (the periodic repetition of this single step that gives rise to the vicinal surface).[163] Reciprocal lattice for a (100) vicinal surface having a simple regular step array can then be constructed as shown schematically in Fig. 6.7. A single step has a reciprocal lattice made of rods centred at the same position as an infinite lattice along the [100] direction. These rods are narrow when viewed in the direction perpendicular to the infinite dimension of the steps (i.e. normal to the plane of the paper) and are broad when viewed in the direction perpendicular to the finite dimension of the step. In this figure, the reciprocal lattice rods are shown in the azimuth perpendicular to the finite dimension. This streak broadening effect has already been described in § 6.4.2. On the other hand, the reciprocal lattice associated with the periodic arrangement of the steps is a set of rods perpendicular to the direction of the macroscopic surface plane. The resulting reciprocal lattice for the whole structure is given by the intersection of these two sets of rods. This is shown as heavy lines in Fig. 6.7 which is a direct view of the RHEED pattern in the azimuth where the incident electron beam is parallel to the edges of the steps (i.e. along the infinite dimension). The broadened rods arising from the low index (100) plane are split into streaks perpendicular to the macroscopic surface. Information about the inclination of the vicinal plane and the dimensions of the underlying steps can be obtained by measuring the misorientation angle and the separation of the split streaks in the diffraction pattern.[163,164]

Using the same principle, diffraction patterns for irregular step arrays can be deduced. In general, the background intensity of the resulting RHEED patterns will be very strong and diffraction spots can be observed due to the 3-D nature of these step arrays. Since the growth rate in MBE is well controlled, the height of most surface steps on a semiconductor film grown

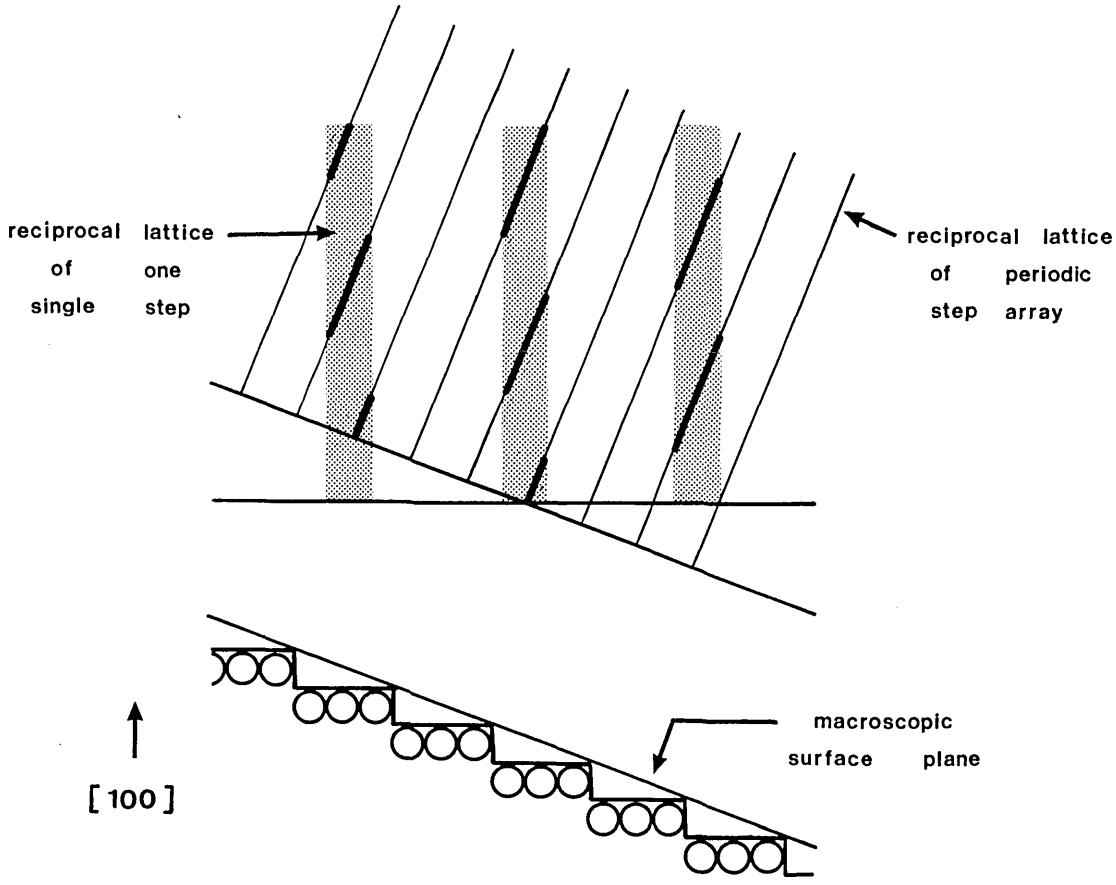
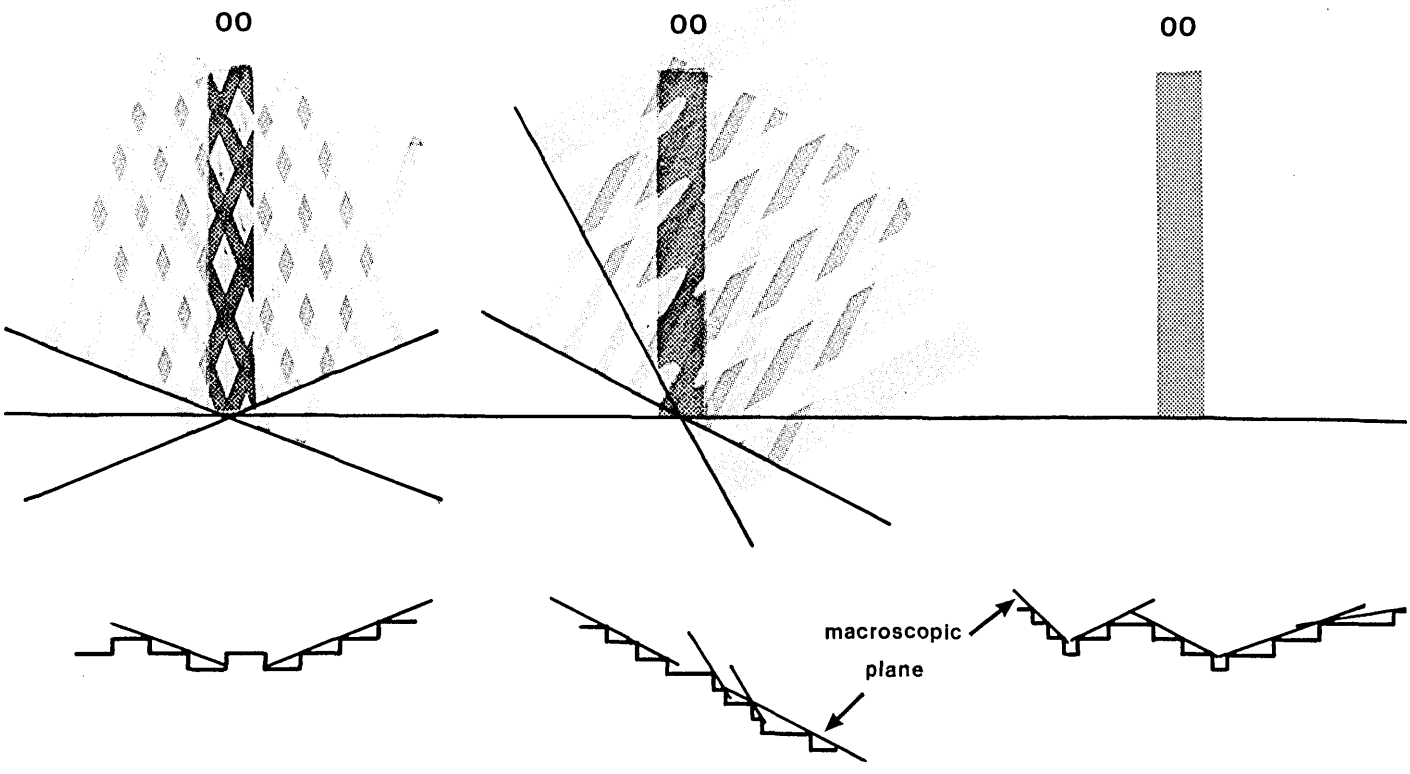


Fig. 6.7 Reciprocal and real space representations of a regular step array on an (100) vicinal surface (from Ref. 163)



(a) fixed terrace width, irregular step direction

(b) irregular terrace width, monotonic step direction

(c) irregular terrace width and step direction

Fig. 6.8 Reciprocal and real space representations for irregular step arrays

by this technique are found to be constant whereas the terrace width and/or edge orientation can vary considerably. In the following discussion, three step array arrangements with constant step height are considered.

a) Terrace width is fixed but the step direction is irregular :

In this case, the reciprocal lattice rods due to the low index plane are modulated along its length. The modulated structures are enclosed by slanted rods arising from macroscopic planes characteristics of the various step directions. An example is shown in Fig. 6.8a where the reciprocal rod is modulated into a series of parallelograms. Note that the intensity profile within the parallelograms is not homogeneous. The intensity of the envelope is much stronger than that in the centre. In cases where the separation between atoms along the facet planes are small, only arrow-head features can be seen.

b) Monotonic step sequence with irregular terrace width :

In this arrangement, the 00 rod is modulated asymmetrically along its length as depicted in Fig. 6.8b. Due to the monotonic nature of the step direction, the modulated structures are preferentially slanted towards one direction (towards the right in this figure). Since a large number of facet planes can arise due to irregular inclinations between terraces with different widths, well-defined macroscopic planes cannot be found. The intensity profile within the modulated structure will thus be more uniform than that in case (a) although its shape will depend on the exact arrangement of surface steps.

c) Both terrace width and direction of steps are irregular :

This can be treated as a convolution of the previous two arrangements and in most cases only broadened rods with more or less homogeneous intensity are produced (Fig. 6.8c).

It is found that the RHEED patterns for α-Sn(100) films with thickness around 1000Å exhibit similar features and will be discussed in a later section (§ 6.5.2b).

6.5 Experimental

6.5.1 Background

In the past, the study of α-Sn thin films has been hampered by the intrinsic difficulty in sample preparation (§ 2.1). Following the pioneering work by Farrow *et. al.*[5] who successfully grew thin films of α-Sn on InSb by MBE, there is still very little progress in the study of the structural properties of this system.

Using RHEED, Farrow *et. al.*[5] reported the observation of a (2x2) pattern from a 0.2μm α-Sn film grown on an InSb(100) substrate. On the other hand, Woodruff *et. al.*[37] demonstrated unambiguously, using LEED, that a 50Å α-Sn overlayer exhibited a two-domain (2x1) pattern. This result agrees with that obtained by Hernández-Calderón and Höchst[35] who used a single azimuth to determine the surface symmetry. Recent photoemission and RHEED studies concerning interface formation of α-Sn on InSb(100)-(4x2) In-stable and c(4x4) Sb-stable surfaces confirmed the existence of a two-domain (2x1) structure for α-Sn films about 200Å thick.[36] There has, however, been no systematic investigation of the surface structure and morphology of α-Sn/InSb(100) surfaces and the following work is an attempt to provide such information. It is believed that such studies are essential for the understanding of the fundamental properties of this group IV semiconductor which is of potential technological importance.[38]

All of the following RHEED experiments are carried out in the growth chamber of our MBE system using a VG Scientific LEG31 electron gun. The angle of incidence is normally set between 1 to 3°. The electron gun is capable of producing an electron beam up to 5keV with a minimum spot size of about 1mm. RHEED patterns recorded along the [100] and the two orthogonal <110> azimuths will be shown.

6.5.2 Results

a) clean InSb(100) substrate

Our *in-situ* cleaned InSb(100) substrates (see § 4.3) always produce sharp RHEED patterns as shown in Fig. 6.9. The surface reconstruction of the

InSb(100) surface can be simply determined by comparing the orders of the streaks in the zeroth-order Laue zone (L_o) of the observed patterns with that shown schematically in Fig. 6.4. The occurrence of the 1/4-order streaks along [110] and the 1/2-order streaks along [$1\bar{1}0$] and [100] directions suggest that the reconstruction is predominantly (4x2).

However, the most important features in the RHEED patterns are the 1/2-order streaks which are curved towards opposite directions along the two orthogonal <100> azimuths. The origin of curved streaks and the dependence of their curvature have already been discussed in § 6.4.3. Whereas curved streaks are commonly observed in GaAs(100) surfaces due to the co-existence of (4x2) and c(8x2) domains,[157,165] this effect has never been reported for the isoelectric InSb(100) surface. Since the (4x2) and c(8x2) reconstructions are simply related by random positioning in the direction of the two-fold periodicity[157] (see Fig. 6.10) and are therefore readily interchangeable, it is believed that these two structures can also co-exist in InSb(100), giving rise to the formation of 1-D disorder boundaries along [110]. From Fig. 6.10, it is clear that boundaries between these two domains will produce streaks curving to the right in the [100] azimuth. Since the periodicity is random only in the two-fold reconstruction direction and that the (4x1) lattice order is maintained, the disorder reciprocal lattice lattice planes will not pass through the origin and curved streaks are only present in the 1/2-order positions.

On the other hand, streaks remain vertical in the <110> azimuths which are either parallel or perpendicular to the disorder boundaries (see § 6.4.3). Note that streaks in the [$1\bar{1}0$] azimuth are much longer than that in the orthogonal direction and nearly merge with that in the 1/4-order Laue zone ($L_{1/4}$). As discussed in § 6.4.2, this is evidence of the presence of domain structures on the surface with the 'short' domain side parallel to the [$1\bar{1}0$] direction. This is consistent with the situation depicted in Fig. 6.10. It can therefore be concluded that our atomically clean InSb(100) surfaces consist of predominantly (4x2) structures with a small amount of c(8x2) domains.

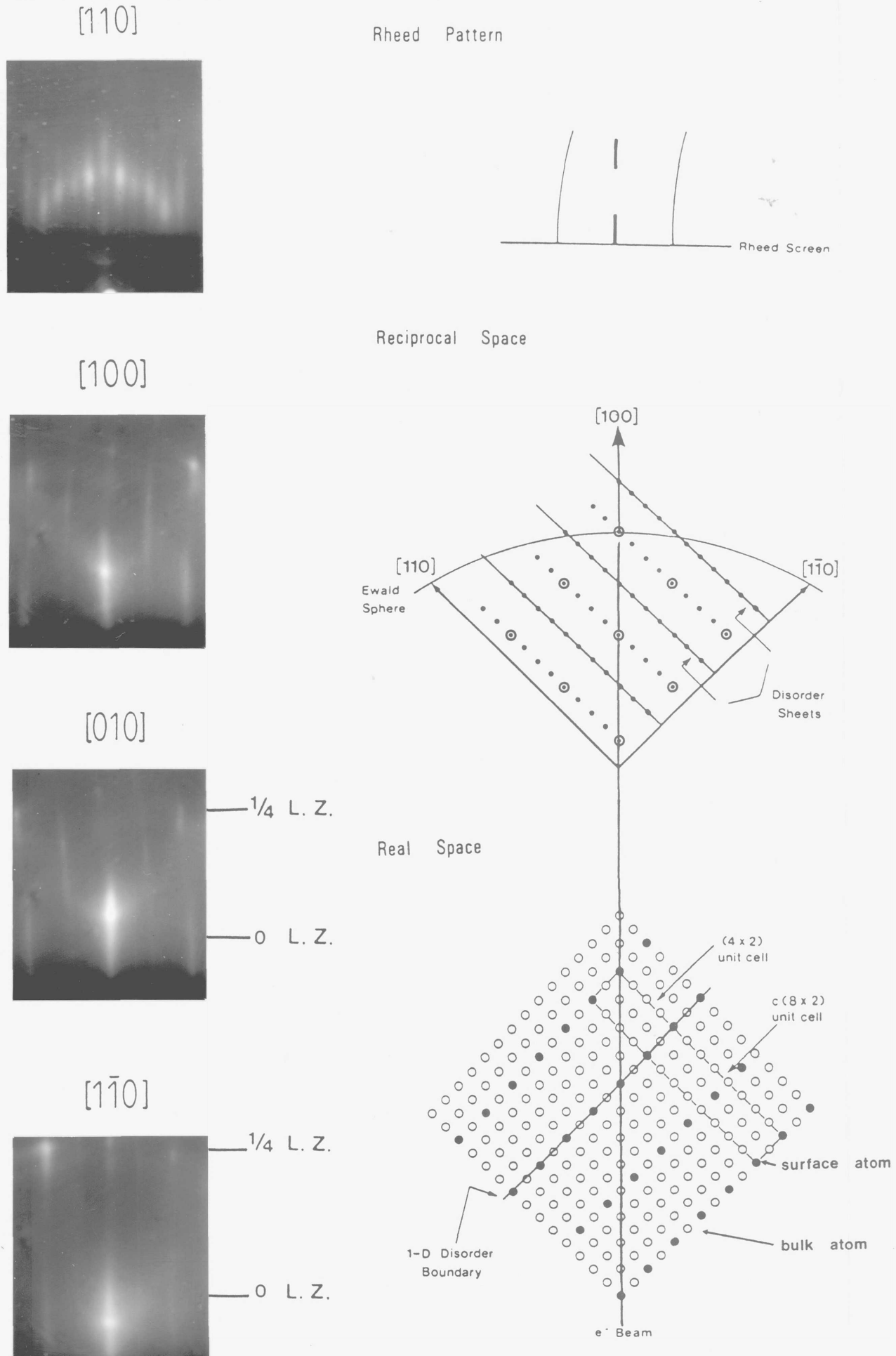


Fig. 6.9 RHEED patterns observed from clean InSb(100) substrate surface prior to growth

Fig. 6.10 Schematic illustrations of curved diffraction streaks arising from the co-existence of (4x2) and c(8x2) domains

b) α-Sn(100) thin films

i) below 200Å coverage

As soon as growth is initiated, the (4x2) superstructure of the substrate pattern is quenched to the bulk structure with a strong background. After about 20Å of Sn have been deposited, 1/2-order streaks begin to appear in the <110> azimuths while the bulk structure is retained along <100>. Whereas $L_{1/4}$ of the clean InSb surface along [1$\bar{1}$0] can be clearly observed, coverage of α-Sn causes it to fade into the background. During this stage, the diffraction patterns exhibit weak intensity oscillations where the frequency is observed to increase with growth rate. This set of RHEED patterns and hence the surface reconstructions remain the same until the overlayer thickness approaches 200Å when the streaks start to broaden slightly (Fig. 6.11).

By considering the zeroth-order Laue zone (L_0) alone, the diffraction patterns shown in the figure exhibit very weak 1/2-order streaks along the [100] direction. In contrast, well-defined 1/2-order streaks along <110> are observed. According to Fig. 6.4, this set of RHEED patterns suggests the existence of 2-domain (2x1) and/or 2-domain c(4x2) structures which may be accompanied by very weak secondary diffraction from c(2x2) or p(2x2) structures. The latter two secondary structures would contribute weak 1/2-order streaks in L_0 along the [100] azimuth. However, since this 1/2-order streak as shown in Fig. 6.11 is almost unobservable, the proportion of these two structures in the surface, if present at all, must be extremely small.

To proceed further, consider the streaks in $L_{1/4}$ along the [100] azimuth. Some weak 1/4- and 3/4-order streaks can be seen in this Laue zone which may correspond to either 2-domain (2x1), p(2x2) or 2-domain c(4x2) structures. However, since the 1/8-order Laue zone in Fig. 6.11 which should be located between $L_{1/4}$ and L_0 is featureless, the possible existence of the latter structure, namely the 2-domain c(4x2) structure can be ruled out. Therefore, we may conclude that the surface of the 200Å thick α-Sn layer is dominated by 2-domain (2x1) structures and perhaps accompanied by a very small amount of p(2x2) and/or c(2x2) structures.

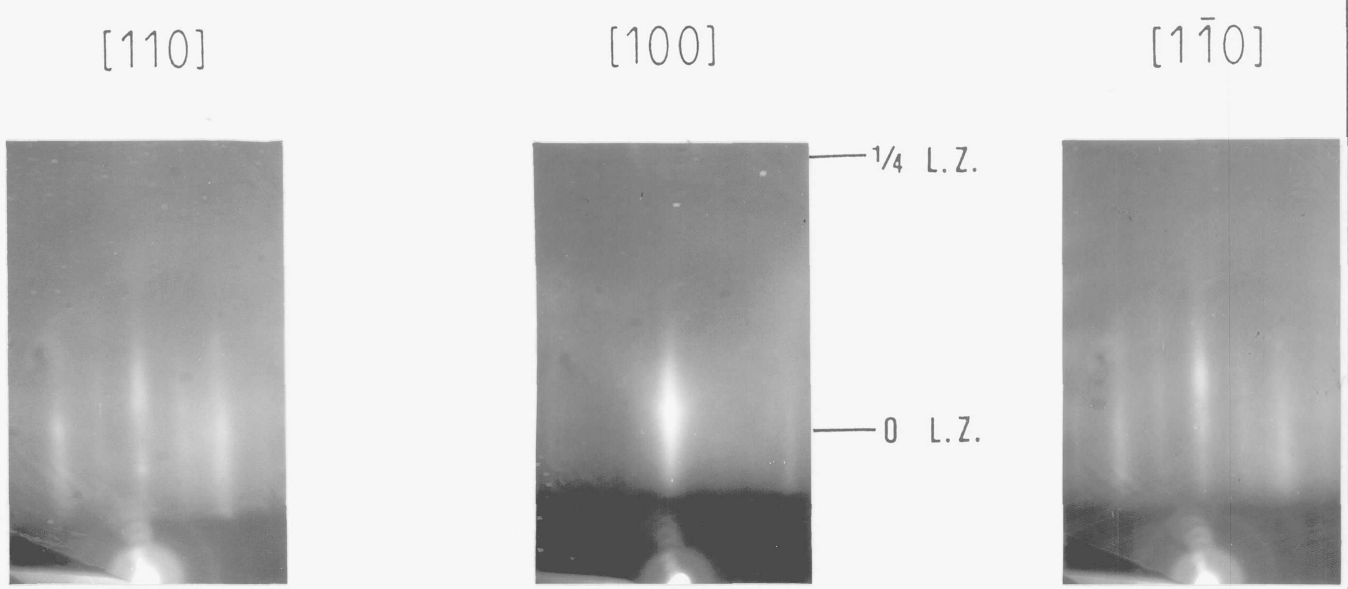


Fig. 6.11 RHEED patterns from the surface of a 200Å thick α-Sn film

This structural determination is indirectly supported by the following two observations :

1) In comparison with the InSb(100)-(4x2) In-stable surface, the background intensity of the α-Sn RHEED patterns are much stronger and the 00 rods are broader. These observations suggest the presence of disorder in the α-Sn surface which may result from the co-existence of several surface structures forming many domain boundaries. Alternatively, disorder can occur due to atomic rearrangement for charge neutralization at the non-polar/polar interface of the α-Sn/InSb(100) system or the formation of defects such as vacancies.

2) For overlayer thicknesses ranging from 20 to 200Å, the diffraction patterns, in particular the 00 beam and the 1/2 order streaks, exhibit very weak intensity oscillations similar to those reported by John *et. al.*.[36] It is found that the intensity oscillation of the 00 beam decays rapidly while that of the 1/2-order streaks persists until the thickness exceeds 200Å. Note that any change in the concentration of the (2x1) and (1x2) domains may induce an intensity alternation of the 1/2-order streaks along the [110] and [1$\bar{1}$0] azimuths and oscillations can thus be observed in these positions. The persistence of these 1/2-order streaks along <110> throughout this range of film thickness may indicate the co-existence of orthogonal (2x1) and (1x2) structures. On the other hand, the intensity oscillation of the

specular beam (in contrast to that of the 1/2-order streaks) may be indicative of a layer-by-layer growth mode.[80] This picture is similar to that observed on Si(100) surfaces where growth proceeds layer by layer but with the second layer starting to grow before the completion of the first.[81] Note that the frequency of the intensity oscillation increases with growth rate.

ii) 500 - 1000Å coverage

As growth proceeds, the intensities of the half and integral order streaks become more intense. For α-Sn films with thicknesses greater than 200Å, the intensities of the 1/2-order streaks along <110> increase significantly and at about 500Å coverage, weak 1/2-order streaks are also observed along the [100] direction (Fig. 6.12). Note that the 00 beam along [100] is broader and longer than that observed for lower coverage. When the overlayer thickness approaches 1000Å, the RHEED pattern exhibits a very complex structure (Fig. 6.13) : parallelograms enclosed by two sets of parallel slanted streaks can be seen along the integral rods, in particular the 00 rod in the [100] azimuth (refer to the schematic representation at the bottom of the figure). These changes are accompanied by the emergence of weak 1/4-order streaks and much stronger 1/2-order beams in L_0 along [100]. By using a smaller diffraction vector perpendicular to the surface ($\mathbf{k}_\perp$), i.e. a smaller angle of incidence, a new ring with streaks at 1/4 and 3/4 positions and very faint streaks at half and integral positions are just observable above L_0 along the [100] azimuth. Moreover, the streaks in L_0 are further elongated and almost overlap with this new zone. When the diffraction vector ($\mathbf{k}_\perp$) is increased, modulated structures (the parallelogram-like features) along the integral rods can be clearly observed (shown in Fig. 6.13 along the [$\bar{1}$10] azimuth).

The structure of the α-Sn surface within this intermediate coverage of 500 - 1000Å is characterized by the increasing intensities of the 1/2-order streaks in L_0 along [100]. This observation suggests that an increasing amount of either the p(2x2) or the c(2x2) structures begins to appear on the α-Sn surface. In addition, a 1/4-order Laue zone ($L_{1/4}$) begin to emerge along [100] with streaks in the 1/4- and 3/4-order positions and faint streaks at the 1/2-order position when coverage approaches 1000Å. The difference in intensities of these two sets of features indicates the

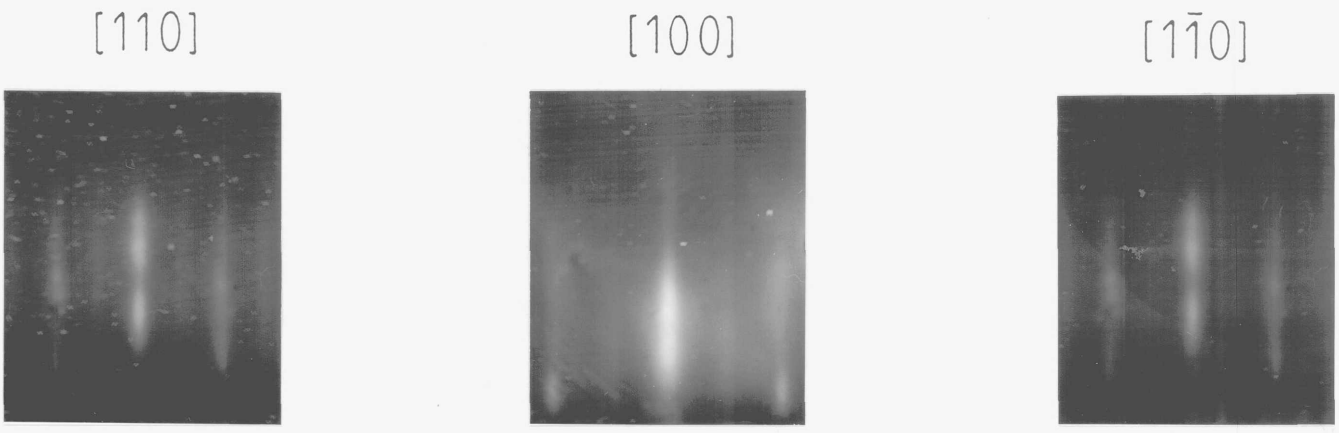


Fig. 6.12 RHEED patterns from the surface of a 500Å thick α-Sn film

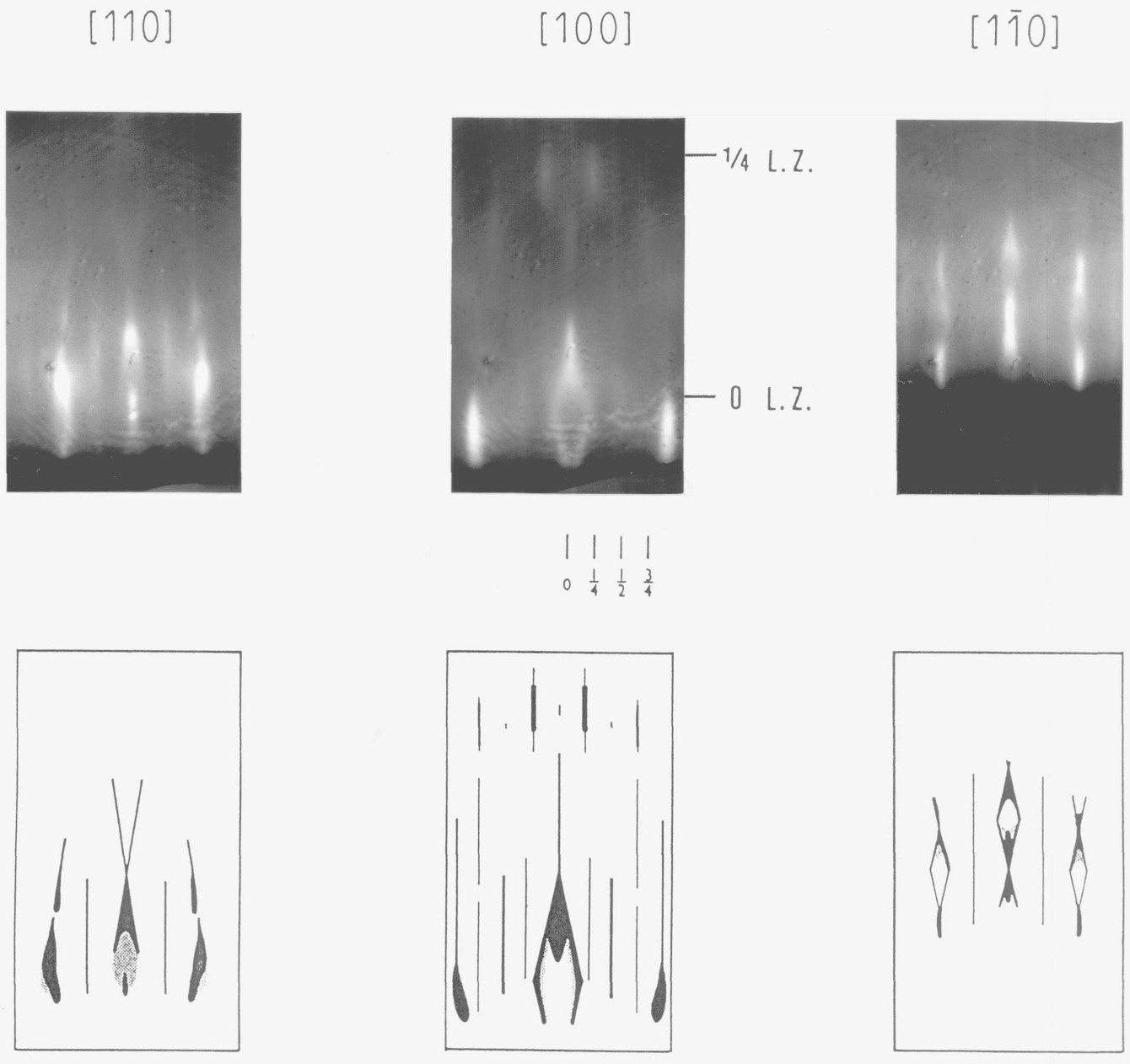


Fig. 6.13 (top) : RHEED patterns from the surface of a 1000Å thick α-Sn film
(bottom) : corresponding schematic representation of the patterns

existence of at least two surface structures. According to Fig. 6.4, it seems that the streaks at the 1/4 and 3/4-order positions may be induced by the formation of p(2x2) domains. This suggests that the increase in intensity of the 1/2-order streak in L_0 along this azimuth is predominantly due to an increasing amount of p(2x2) domains present in the surface. The existence of c(2x2) structures can thus be ruled out accordingly. On the other hand, the development of c(4x4) structures may be responsible for the occurrence of the weak 1/2-order streaks in this 1/4-order Laue zone.

Another feature of this growth stage is the appearance of parallelogram-like modulated structures along the integral rods. According to § 6.4.4, this suggests the presence of irregular step arrays on the α-Sn surface. Since our RHEED patterns closely resemble those shown schematically in Fig. 6.8a, it seems that the width of these steps are constant but the direction of steps is irregular (i.e. can go up and down at random). In addition, the step terraces should be flat and wide enough to support the surface reconstructions mentioned above which give rise to streaks in the fractional-order positions. Note that the RHEED patterns along the two orthogonal <110> directions are very similar except that the diffraction features in [1$\bar{1}$0] are shifted upwards due to the use of a larger ($\mathbf{k}_\perp$) for recording. The two sets of slanted streaks enclosing the parallelograms in these azimuths are inclined at about 7.5° to each side of the integral streaks. Along [100], the modulated streaks are much broader and the inclination angle is also larger (≅ 12°).

The slanted streaks in the diffraction patterns may correspond to high index planes such as {510} or {711} which form interplanar angles of 11.4°and 11.3° with the {100} plane respectively.[156] They may represent the macroscopic surface plane of a step array with perpendicular planes (Fig. 6.14a) or the inclined side-planes of each step (Fig. 6.14b and inset). Although RHEED is effective in detecting the presence of surface steps, their exact shapes can only be revealed by some sort of microscopic techniques. Plan view transmission electron microscopy (TEM) has proved to be very useful in such studies.[166]

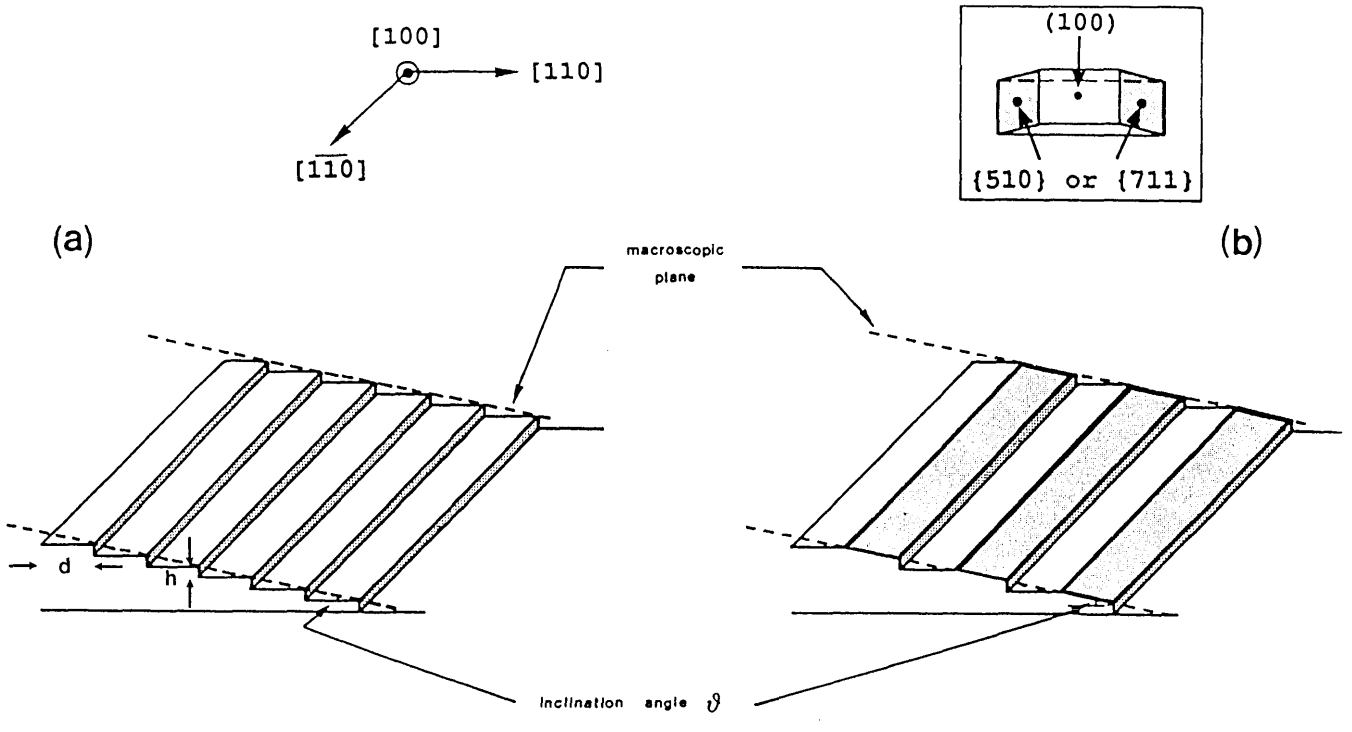
In order to support the c(4x4) reconstruction observed in the RHEED pattern, the width of the terrace d in the [110] direction must be larger than ~ 26Å (≅ $4a_o$ where a_o is the lattice constant of pseudomorphic α-Sn

films which is equal to the bulk InSb(100) value of 6.479Å). For an inclination angle of $\vartheta = 12^{\circ}$, the step height h must satisfy the following geometric relation (see Fig. 6.14) :

$$h/\tan\vartheta = d \geq 2.6\text{Å}$$
$$\Rightarrow \quad h \geq 5.32\text{Å} \qquad (6.14)$$

Therefore, it seems that the height of the surface steps on the α-Sn surface is at least diatomic.

It must be emphasized that the step array arrangement depicted in Fig. 6.14 represents a surface step structure obtainable only from ideal layer-by-layer growth. In a real growing film surface, 2-D nucleation may occur on the terraces forming kinks that reside along the step edges.[167] The presence of these kinks will further complicate the RHEED patterns by, for example, introducing inhomogeneity in the intensity profile within the modulated streaks or broadening the slanted streaks.



(a) step array with perpendicular planes forming a macroscopic surface plane

(b) step array with inclined planes (inset : relative orientation of the of sides of a step or an island)

Fig. 6.14 Two possible step structures on the α-Sn surface

iii) 1000 - 2500Å coverage

No new features are observed from the RHEED pattern as growth proceeds further. On the other hand, the intensities of the slanted streaks along <110> and the 1/4-order streaks along [100] increase with the thickness of the α-Sn overlayer and at a coverage of 2000Å, they become clearly observable (Fig. 6.15). Due to the complexity and weak intensities of the RHEED patterns, schematic patterns along [110] and [100] are also drawn (bottom of Fig. 6.15) to facilitate discussion. Two sets of streaks, labelled A and B, located at two different Laue zones can be observed along the [110] azimuth. The streaks labelled A are located at the 1/4 and 3/4 positions in $L_{1/4}$ while a faint streak at the 00 position extending from $L_{1/2}$ is seen in B. A comparison of these RHEED patterns with that shown in Fig. 6.4e proves unambiguously the presence of c(4x4) structures.

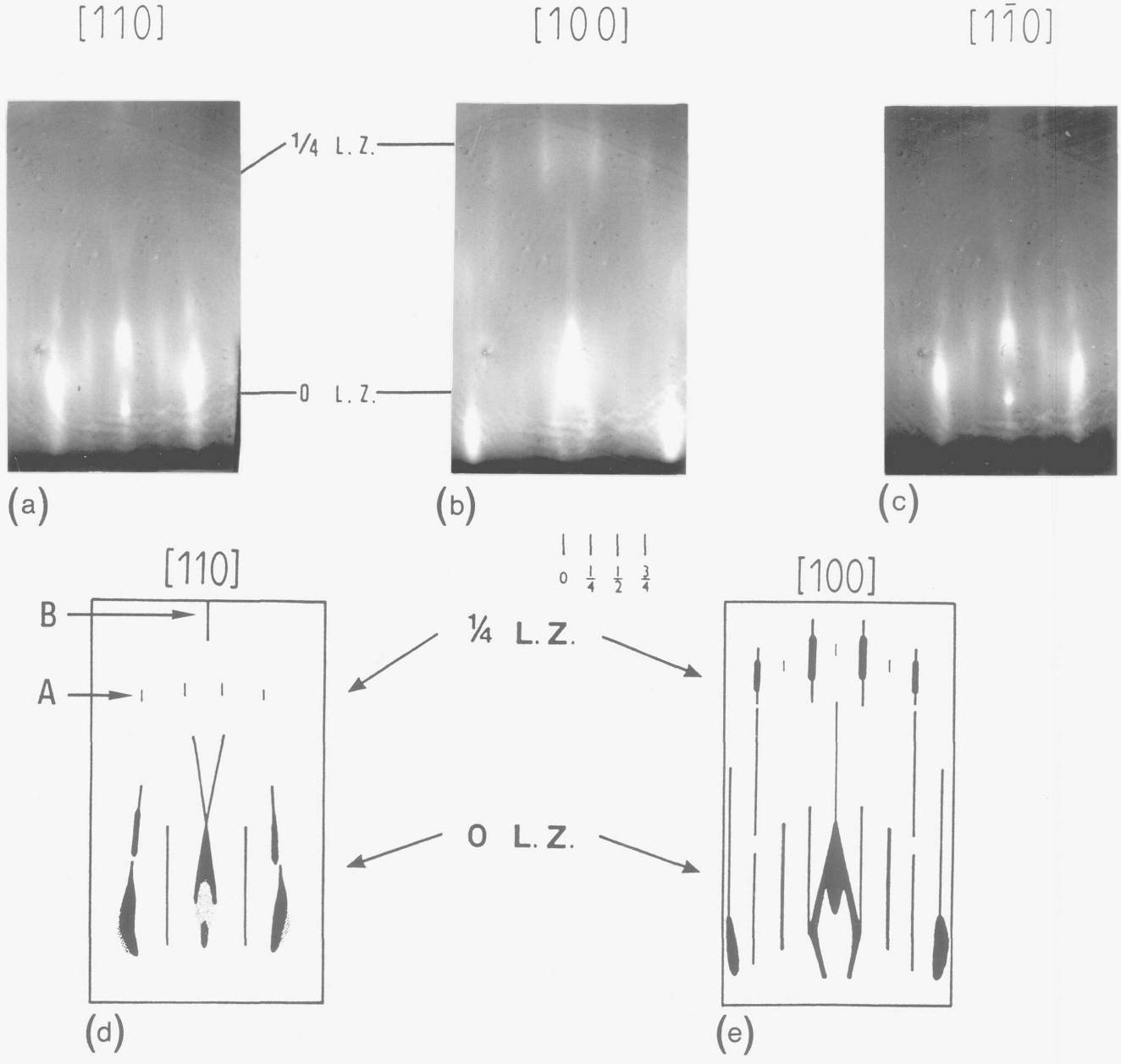


Fig. 6.15 a - c : RHEED patterns from the surface of a 2000Å thick α-Sn film
d - f : corresponding schematic representation of the patterns

For coverage exceeding 2500Å, both the intensities of the streaks and the background in the RHEED pattern increase. When the overlayer thickness approaches 3000Å, white specks of β-Sn can be seen on the surface of the sample. The development of surface structures for the α-Sn(100) surface is summarized in Table 6.2.[38]

TABLE 6.2

α-Sn Coverage	Reconstructions
0 (clean InSb(100) substrate)	(4 x 2)
0 - 20 Å	(1 x 1)
20 - 200 Å	2-domain (2 x 1) + very weak p(2 x 2) or c(2 x 2)
500 - 1000 Å	p (2 x 2)
1000 - 2500 Å	c (4 x 4)

6.6 Structural Models for α-Sn(100) Surfaces

α-Sn and Si are both group IV elements having the diamond crystal structure. Because of a) the similarity of the core potentials of these two elements and b) the occurrence of a seemingly 2-domain (2x1) structure in the α-Sn(100) surface which is commonly found in Si(100) surfaces, it may be instructive to compare the structural models of these two surfaces.[38] Ihm *et. al.*[168] suggest that the results of their total energy calculations on various Si(100) surface structures can be applied to Ge(100) and in fact to any (100) surfaces with diamond structures.

6.6.1. the Si(100) surface

i) surface reconstructions

The atomically clean Si(100) surface was found to exhibit several reconstruction structures such as 2-domain (2x1), p(2x2), c(4x2)[169] and

(2xn) where $6<n<10$.[170] The 2-domain (2x1) structure is commonly observed at room temperature and an ordered structure of 2-domain c(4x2) has been observed at about 200K.[171] In fact, it is commonly found that several of these structures can co-exist on Si(100) surfaces. Extremely surface sensitive experiments such as atom diffraction studies[172] reveal that Si(100)-(2x1) surfaces consist of very rough and disordered structures with secondary diffraction from (2x2) and c(2x4) superstructures. This result agrees with the scanning tunnelling microscopy (STM)[169] data which also indicates the occurrence of these surface structures. This co-existence can also be justified on energetic grounds : theoretical calculations by Ihm *et. al.*[168] and Chadi[173] reveal that the total energies of these structures are almost degenerate. Furthermore, monatomic steps from 2-domain (2x1) structures (in contrast to the single domain (2x1) which exhibits biatomic steps), the coexistence of different domains such as 2-domain (2x1), (2x2) and c(4x2) and the phase boundaries between them could all contribute to the observed roughness and disorder of the surface.

An additional structure has recently been observed from Si(100) surfaces : exposure of (2x1) surfaces to a hydrogen dosage higher than 10^{-2} L followed by a brief annealing at 600 °C induces the formation of c(4x4) structures.[174,175] I-V profiles of the diffracted LEED spots of this structure reveal the existence of monatomic steps on the surface.[175]

ii) structural models

Reconstruction of the Si(100) surface has now been universally accepted as arising from the formation of surface dimers and the (2x1) structure is recognized as the basic building block. The dimerization of surface atoms can be in the form of symmetric or asymmetric dimers. (2x1), p(2x2), c(2x2), c(4x2) and c(4x4) structures formed by **asymmetric dimers** can easily be realized by arranging the two non-equivalent dimers in different ways as shown in Fig. 6.16a. Alternatively, Pandey[176] has proposed a **missing dimer defect** (**π-bonded defect**) model which can account for all of the observed structures and is found to be energetically more favourable than that of the asymmetric dimer configurations (see Fig. 6.16b). Using STM, Tromp *et. al.*[169] have shown that both kinds of dimers as well as missing dimer defects are present on the Si(100) surface.

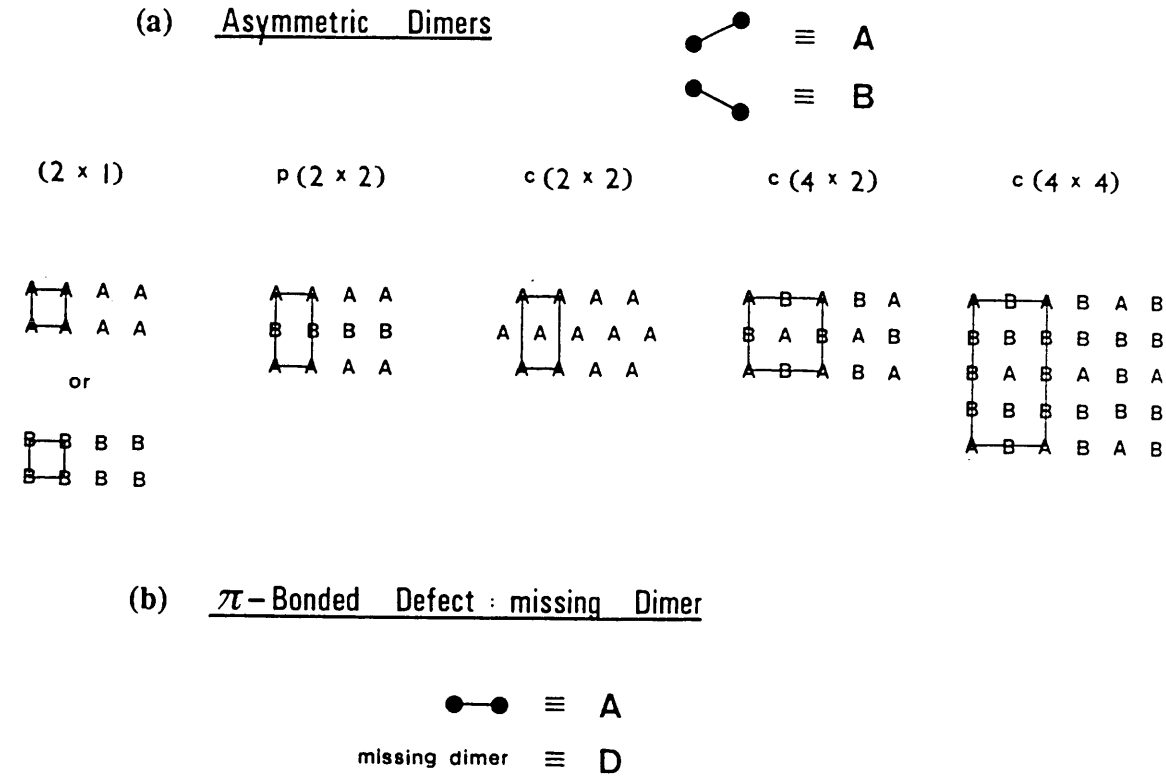


Fig. 6.16 Constructions of various surface reconstruction structures using (a) asymmetric dimers and (b) symmetric dimers and π-bonded defects

On the other hand, it is well known that the adsorption of H can revert asymmetric dimers to symmetric ones by fulfilling the dangling bonds in the surface and eventually breaking the dimer bonds.[177] Failure to convert the c(4x4) reconstruction back to (2x1) or (1x1) structures upon hydrogenation[174,175] suggests that an alternative to asymmetric dimers may be required to model the Si(100)-c(4x4) surface. Kato *et. al.*[175] have used Pandey's **missing dimer model** to construct both a roughened and an ordered (2x1) structure (first column in Fig. 6.16b). In addition, they proposed a regular arrangement of missing defects in a (4x4) unit mesh which forms islands with monatomic step height. In this arrangement, three dimers are treated as a single unit as depicted in Fig. 6.16b (model 2). Structural change between the roughened (2x1) and c(4x4) surfaces, considered as disorder and order forms of the missing dimer defects, was found to occur at ~ 600°C. The number of missing dimers could be reduced by further annealing the surface to ~ 700°C and give rise to an ordered (2x1) structure. The c(4x4) periodicity constructed using this 3-dimer model, however, will not be annihilated upon hydrogen adsorption which agrees with experimental results.[174,175] This suggests that most of the dimers present on the Si(100) surface may be symmetric.

6.6.2 Analogy of Si(100) and α-Sn(100) surfaces

Similarity of the surface structures and the energetics between α-Sn(100) and Si(100) surfaces are demonstrated in the following arguments :

a) From § 6.5.2, it is clear that the α-Sn(100) surface can exhibit 2-domain (2x1), p(2x2) and c(4x4) reconstructions which are also found in Si(100) surfaces (§ 6.6.1).

b) Total energy calculations performed by Ihm *et. al.*[168] and Chadi[173] showed that the higher order reconstructions found in Si(100) surfaces can be classified into two groups according to the energies and interchangeabilities of the structures. The first group consists of (2x1), p(2x2) and c(4x2) structures which are almost degenerate in total energies. In addition, structural transitions among these phases can readily occur (see Fig. 6.4). The second group is based on c(2x2) and p(4x2) structures which are also degenerate in total energies. Domains of these two families can co-exist on the Si(100) surface because the difference in their total energies is very small. On the

other hand, interchanging the structures between the two families requires huge amount of energy for the breaking of some dimer bonds and creating some new ones. In α-Sn(100) surfaces at 500Å coverage, 2-domain (2x1) and p(2x2) structures can co-exist which proves that the energy difference between these domains is also very small on this surface. Note that neither c(2x2) nor p(4x2) domains are present in this case.

Such observations imply that the theoretical results on the Si(100) surface may be applied to the α-Sn(100) surface.

6.6.3 the α-Sn/InSb(100) Surface

i) reconstruction building blocks

From the previous section, it is clear that a structural model based on dimerization can also be used to account for the sequence of structural changes in the α-Sn(100) surface. Unlike Si,[174,175] hydrogen adsorption experiments cannot be used to distinguish symmetric and asymmetric dimers in α-Sn because tin hydride is unstable.[37] However, due to the strong background and broadened streaks observed in our RHEED patterns which are characteristics of a roughened and disordered surface, it seems appropriate to use **symmetric dimers** together with **missing dimer defects** as the building blocks for the α-Sn(100) reconstruction model. Such a model is characterized by a roughened and disordered surface which is consistent with the strong background and broadened streaks observed in our RHEED patterns (see Fig. 6.11). Using this model, it is obvious from Fig. 6.16b that various higher order structures can be constructed. In practice, however, randomly distributed asymmetric dimers and symmetric dimers with missing dimer defects may well co-exist on the α-Sn surface due to the similarities in energies.[173,178]

ii) reconstruction models

As shown in Fig. 6.16b, it can be seen that various superstructures based on the dimerization of surface atoms can be constructed in terms of the following two models :

(1) a dimer (depicted as A in Fig. 6.16b) together with a π-bonded defect (depicted as D).

(2) a three-dimer block together with a missing dimer defect.

Using model 1, it is clear that the structural transition between 2-domain (2x1) and p(2x2) does not involve a large degree of bond breaking (4 bonds per unit cell) and therefore the energies of these structures may be very similar to each other. On the other hand, transition of p(2x2) to c(4x4) requires the breaking of 8 bonds per unit cell. Note that an alternative c(4x4) unit cell (depicted in Fig. 6.16b, model 2) involving fewer missing dimer defects can be formed by replacing rows of defects in model 1 with rows of dimers. However, the transition between these two different forms may be energetically unfavourable since considerable bond breakage is needed. The c(4x4) structures in models (1) and (2) are characterized by the presence of missing dimer defects and the formation of clusters of surface atoms respectively.

From the previous discussion (§ 6.5.2b) it is evident that 2-domain (2x1), p(2x2) as well as c(4x4) structures co-exist on the α-Sn(100) surface. The background intensity of the RHEED pattern is also found to have increased due to the presence of disorder in the surface. The random distribution of domain walls separating different superstructures and the presence of defects in the form of missing dimers or lattice voids may be responsible for the surface disorder. These two observations alone would favour the use of model 1 for the reconstructions of the α-Sn(100) surface. On the other hand, the α-Sn surface exhibits significant facets and step structures. This may be indicative of the presence of islands or blocks of structures, for instance, the c(4x4) and/or p(2x2) domain which would favour the use of model 2.[175] Due to the complicated nature of this α-Sn(100) surface, it seems premature, at this stage, to stick to one particular model without further investigation.

The progressive increase in periodicities of the surface atoms as the thickness of the α-Sn film increases, i.e. the occurrence of 2-domain (2x1) followed by p(2x2) and then c(4x4) structures, may be related to the amount of strain energy stored in the α-Sn films. In fact, Phillips[179] has proposed a theory to account for the stabilization of microdomains by epitaxial

misfit strain energies. In contrast to the general rule (Ostwald's Rule) that small unit cells are more stable than large ones at high temperatures, it was found that the superstructures of Sn on Ge(111) changed from (5x5) to (7x7) as the temperature is increased.[179] Phillips[179] suggested that this is mainly due to the energy-controlled formation of closely packed islands - a characteristic of strained-layer systems. It was suggested that the size of these islands or the periodicity of the surface atoms are energy-dependent : formation of large islands are energetically more favourable at higher temperature as a result of a more rapid decrease in misfit strain energy of the atoms in the surface plane than that in the local rebonding energy.[179] Kaplan[178] has argued that while certain reconstructions with large unit cells are suppressed on narrow terraces, larger periodicities can be supported when the islands gradually coalesce to form wider terraces as more and more atoms are deposited.

In our case, the pseudomorphic growth of metastable α-Sn films, substrate-stabilized to temperatures above the bulk value of 13.2°C, would be energetically favourable if the strain energy of the film is less than that required for the development of a dislocation (refer to § 3.4). As the thickness of the α-Sn overlayer increases, the amount of strain energy stored will increase and the substrate stabilization effect will be reduced. When the thickness of the overlayer approaches a certain critical value, the surface layer will start to relax. More bonds will be broken and a more open lattice (i.e. with larger unit cells) will be formed. This picture is consistent with the c(4x4) structure depicted in model 1 of Fig. 6.16b.

6.7 Conclusions

Structural properties of α-Sn thin films pseudomorphically grown on atomically clean InSb(100)-(4x2) surfaces have been investigated by RHEED. Diffraction patterns are analyzed using the reciprocal lattice-Ewald's sphere construction within the kinematic approximation framework. Similar to the well-known GaAs(100) surface, InSb(100) surfaces prepared by our substrate cleaning procedure are found to consist of predominantly (4x2) structures with a small amount of c(8x2) domains. The co-existence of these two structures gives rise to 1/2-order curved streaks along <100> azimuths, seen for the first time in InSb(100) surfaces. The origin and

characteristics of these curve streaks are explained in terms of the presence of 1-D disorder boundaries.

Different α-Sn surfaces which evolved during various stages of growth are discussed. The surface morphology of the growing α-Sn surfaces can be broadly classified into four stages :

i) Initial stage :

The α-Sn/InSb(100) interface is characterized by disorder features which may be caused by either the breakage of surface dimer bonds in the substrate or by atomic rearrangement at the interface. Due to the low growth temperature (≤ 50°C), the surface migration rate of Sn atoms is limited and disorder may arise from the random distribution of Sn atoms on the surface.

ii) Planar growth :

For thickness greater than 20Å growth proceeds in a layer-by-layer mode. The surface reconstruction is predominantly 2-domain (2x1) with a small amount of p(2x2) structures.

iii) Steps and island growth :

p(2x2) surface structures are well developed at a coverage of 500Å. When the α-Sn overlayer thickness approaches 1000Å, modulated structures are found along the integral-order streaks in the RHEED patterns. This suggests that arrays of steps with flat tops, fixed height and irregular step directions are randomly distributed on the surface. At the same time, c(4x4) structures also starts to emerge.

iv) Relaxation of pseudomorphic film :

Clear c(4x4) RHEED patterns with increasing intensities in the 1/4-order streaks are observed when the overlayer thickness approaches 2500Å. At a thickness of about 3000Å, white specks of β-Sn are observed on the surface.

Due to the similarities of core potentials and surface reconstructions between the Si(100) and α-Sn(100) surfaces, structural models based on the dimerization of surface atoms may be applicable for both surfaces. Since the growth of α-Sn(100) films is pseudomorphic and strong background is observed in the RHEED pattern, it is believed that the surface structure is dominated

by symmetric dimers and missing dimer defects. The driving force for the progressive increase in periodicities of the surface atoms with film thickness (i.e. 2-domain (2x1) → p(2x2) → c(4x4)) is discussed in terms of the energetics of the α-Sn film. It is thought that α-Sn films tend to relax at high coverage due to the reduction of the substrate stabilization effect, leading to the formation of a more open surface structure.

CHAPTER 7 MAGNETO-TRANSPORT AND MAGNETO-OPTICAL PROPERTIES OF α-Sn

7.1 Introduction

Although the RHEED technique discussed in the previous chapter can provide valuable information on surface structural properties, direct assessment of the "quality" of MBE grown samples has to be obtained from electrical and magneto-transport measurements. Hall effect measurements are commonly employed to obtain material parameters such as semiconductor type, carrier concentration, resistivity and Hall mobility.[180,181] In a semiconductor with one dominant carrier, the high-magnetic-field Hall coefficient is a direct measure of the semiconductor type and its carrier concentration. In heteroepitaxial systems, however, mixed conduction of light holes, heavy holes and electrons from closely placed conduction band minima can make Hall measurements difficult to interpret as in the case of the α-Sn/p-InSb system. Because of its narrow bandgap, InSb has no insulating or semi-insulating form and when used as a substrate can contribute significantly to the measured Hall quantities. During the course of this work, a two-dimensional electron gas (2DEG) is observed for the first time at the interface of an α-Sn/InSb heterostructure. This 2DEG dominates the electrical behaviour of the system and further complicates the analysis of Hall data, thus limiting the usefulness of the technique.[55]

Magnetoresistance measurements based on Shubnikov-de Haas (SdH) effect, on the other hand, are particularly useful in studying the properties of the α-Sn/InSb system. The existence of a 2DEG occupying several different subbands is manifested by the presence of more than one frequency in the SdH oscillations and the relative distribution of carriers between the subbands can be deduced from the oscillation periods.[182] The reduced dimensionality of the carriers is evident from the results of tilted magnetic field experiments.

In order to understand the nature and the location of the 2DEG as well as the properties of the carriers in the bulk α-Sn films, far infrared magneto-optical experiments were also carried out. In addition to bound-hole transitions from the p-InSb substrate, cyclotron resonance transitions can

also be observed which provide a direct and accurate method of measuring the effective masses of the charge carriers. Much of the experimental work reported in this chapter was carried out in co-operation with Dr. W. T. Yuen (Physics Department, Imperial College).

In this chapter, the basic theories behind these magneto-transport and magneto-optical experiments will be presented. The practical aspect of the measurements and the results will then be discussed.

7.2 Hall Effect Measurements

7.2.1 Basic theory

Hall effect measurements are routinely used to determine the electrical transport properties of semiconducting materials.[180] In these experiments, a known current is constrained to flow along a well-defined direction by the sample geometry.[183,184] The application of a magnetic field perpendicular to the current direction will cause an initial deflection of charge carriers in the transverse direction, i.e. in a direction normal to both the current and the magnetic field. Since no current path exists in this direction, carriers will accumulate on one side. A Hall electric field is thus established which opposes the motion of the carriers preventing further accumulation. In equilibrium, the magnetic Lorentz force will be exactly balanced by this Hall electric field and all the carriers will move through the sample undeflected, provided they have the same drift velocity. In this case, the magnetoresistance will be zero, i.e. there will be no change in the sample resistance when a magnetic field is applied. In practice, however, carriers do have a distribution of speeds and only for those of some "average" speed is the magnetic deflection of the Lorentz force exactly compensated by the electrostatic Hall field. Carriers moving either faster or slower than this average speed will follow a curved (and hence elongated) path from one end of the sample to the other. Curvature of many carrier paths gives a lower macroscopic conductance resulting in the magnetoresistance effect which will be discussed in the next section (§ 7.3).

Suppose a current density (J_x) is established in the sample along the x-direction, the magnetic field (B_z) is applied in the z-direction and no

current is allowed to flow in the direction of the Hall field (E_y). In Hall effect experiments, the resistivity (ρ_{xx}) and Hall coefficient (R_H) are measured. These two parameters are related to the components of the conductivity tensor (σ) by :

$$\rho_{xx}(B) = \frac{\sigma_{xx}(B)}{\sigma_{xx}^2(B) + \sigma_{xy}^2(B)} \tag{7.1}$$

$$R_H(B) = \frac{E_y}{J_x B_z} = \frac{-\sigma_{xy}(B)}{B_z\left[\sigma_{xx}^2(B) + \sigma_{xy}^2(B)\right]} \tag{7.2}$$

However, the ultimate purpose of most of these experiments is not to determine the conductivity elements themselves but rather some underlying properties such as the density and the mobility of the carriers. For the simplest case where (a) there is only one dominant carrier and all conduction takes place in a single band with a spherical Fermi surface, (b) the dependence of energy **E** on crystal momentum **k** is parabolic, and (c) scattering can be described by a single relaxation time constant, the carrier density (n or p) and Hall mobility (μ_H) can be easily obtained from :

$$n = \frac{r_H}{qR_H}, \qquad \mu_H = |R_H|\,\sigma \tag{7.3}$$

where q is the electronic charge and the value of the Hall factor r_H depends on the dominating scattering mechanism. For an isotropic, energy-independent relaxation time, r_H is equal to unity. In this case, R_H and ρ_{xx} are both independent of B and the elements of the conductivity tensor are given by

$$\sigma_{xx}(B) = \frac{en\mu}{1 + \mu^2 B_z^2} \qquad \sigma_{xy}(B) = \frac{en\mu^2 B_z}{1 + \mu^2 B_z^2} \tag{7.4}$$

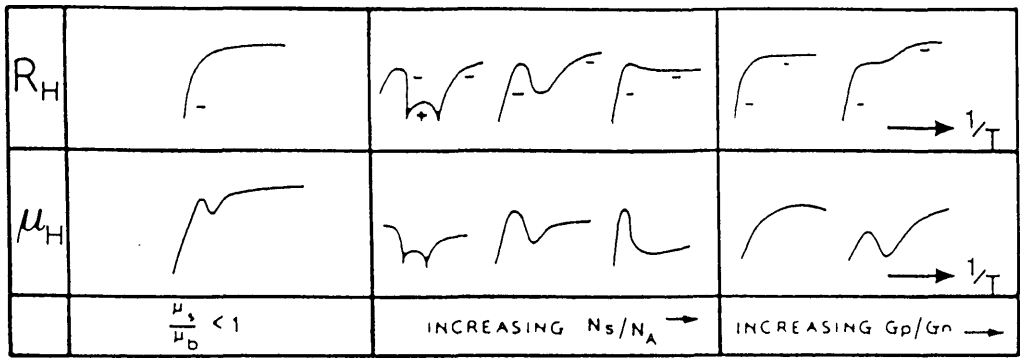
Unfortunately, samples that meet these requirements are rarely encountered. In the case of p-type InSb substrate, for example, Hall effect measurements are complicated by the mixed conduction of electrons and holes due to their large difference in mobility. With a low magnetic field, classical Maxwell-Boltzmann statistics give the following expressions for the conductivity and Hall coefficient :

$$\sigma = e\,(n\mu_n + p\mu_p) \tag{7.5}$$

$$R_H = \frac{-\,r_H\,(n\mu_n^2 - p\mu_p^2)}{q\,(n\mu_n + p\mu_p)^2} \tag{7.6}$$

where μ_n and μ_p are the mobilities of electrons and holes respectively.

Experimentally, deviations from classical behaviour are often observed, especially in heterostructures and in bulk structures having a surface accumulation layer where multi-carrier conduction occurs.[181] In the case where a two-dimensional electron gas (2DEG) is present, mobility difference between carriers in different subbands (see § 7.3.1) can produce multi-carrier changes in the measured Hall quantities which may become very complicated for analysis. Based on a theoretical model for multilayer structures, Lou and Frye[181] have successfully accounted for the dependence on surface condition and sample thickness observed in Hall data obtained from LPE HgCdTe layers. Some of their results are summarized in Fig. 7.1 and will be used for comparison with the Hall data obtained from our α-Sn/InSb samples. Quantitatively, Beck and Anderson[185] have developed an analytical technique in which the concentration and the corresponding mobilities of each carrier present in a multi-layer structure can be obtained. Using the magnetic field dependence of the Hall data, they are able to generate a "mobility spectrum" in which the maximum carrier density or maximum conductivity can be determined as a continuous function of mobility. The major advantage of this technique is that it does not require prior knowledge of the number of different types of carriers nor their properties. This technique has been used to analyze Hall data from a modulation-doped multi-quantum-well GaAs/AlGaAs heterostructure. The carrier densities and mobilities of the confined 2DEGs deduced from the mobility spectrum is found to be in good agreement with that from SdH measurements. This technique can, therefore, be used to tackle the multi-carrier conduction problem in our α-Sn/InSb samples. Unfortunately, the implementation of the mobility spectrum algorithm is quite a formidable task and is beyond the scope of this work. In the following studies, Hall data will be used solely for determining the carrier type of the α-Sn epilayer and to identify the presence of multi-carrier conduction.



(a) n-skin on n-type bulk layer

(b) n-skin on p-type bulk layer

(c) n-bulk layer on p-bulk layer

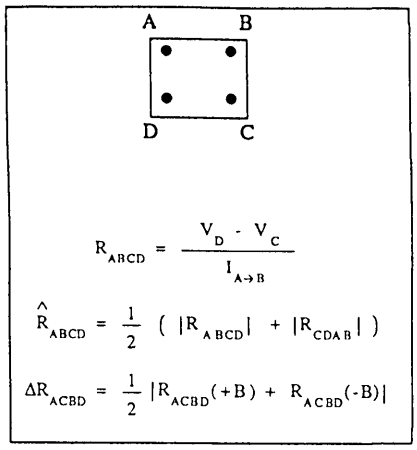
Fig. 7.1 Qualitative representation of the simulated Hall coefficient (R_H) and Hall mobility (μ_H) for three different heterostructures (from Ref. 181)

7.2.2 Experimental Techniques

The same sample preparation procedure was used for all electrical characterization including Hall, SdH and magneto-optical measurements. Square samples (~5mm × 5mm) with standard four-point-contact geometries were employed. Clover-leaf or Hall-bar patterns were not used lest local heating arising from the eroding process might affect the quality of the metastable α-Sn epilayer. For the same reason, the commonly used In contacting method which requires high temperature annealing (~150°C) and subsequent soldering was unsuitable for the α-Sn/InSb system. Instead, highly conductive Ag paint was used with thin gauge copper wires and the contacts were made as near to the corners of the epilayer as possible. In all cases, the ohmic contact requirement was checked before pursuing any electrical measurement.

Van der Pauw Hall measurements[186] were carried out using an automated pulsed-magnetic-field system which allows continuous temperature measurement in the range of 4.2 to 300K (see Ref. 187 for details). In addition, Hall measurements were also performed at 4.2K prior to Shubnikov-de Haas measurements using a superconducting magnet system (see § 7.3.2). For a particular combination of temperature and magnetic field strength, eight voltages were recorded to take into account the two directions of current and magnetic field. Any minor contact potential and geometric asymmetry would thus be cancelled through averaging. From the measured voltages, the

specific resistivity (ρ) and Hall coefficient (R_H) could be computed from the following expressions :[186]



$$\rho = \frac{\pi d}{2\ln 2}\left(\hat{R}_{ABCD} + \hat{R}_{BCDA}\right) f\left(\frac{R_{ABCD}}{R_{BCAD}}\right)$$

$$R_H = \frac{d}{B}\left(\frac{\Delta R_{ACBD} + \Delta R_{BDAC}}{2}\right) \qquad (7.7)$$

where the sample thickness d is assumed to be the same as the substrate thickness (~ 0.5mm) and *f* is the Van der Pauw function.[186]

Using the automated pulsed-magnetic-field system, the variation of ρ and R_H as a function of temperature in the range between 4.2 to 300K could be obtained. Data were normally taken on warming up the sample to ensure a more controllable temperature change. Alternatively, the magnetic field dependence of the resistivity and Hall coefficient could also be obtained. Since the magnetic field strength was limited to approximately 0.1T, all measurements were therefore restricted to the low field regime ($\mu B < 1$) where quantum oscillations would not be observed. From the two quantities ρ and R_H, the **apparent** carrier concentration (n) and Hall mobility (μ_H) could be computed from Eqn. 7.3.

7.2.3 Results and Discussions

i) Hall Measurements of p-InSb substrates

Hall measurements were performed on p-InSb substrates subjected to the normal cleaning procedure discussed in chapter 4 but without subsequent epitaxial growth. Classical behaviour can be observed in the plot of the magnitude of the Hall coefficient ($|R_H|$) as a function of temperature (Fig. 7.2). At high temperatures (T > 125K) where intrinsic electrons with high mobility dominate the conduction, the Hall coefficient is negative. At lower temperatures, the electron concentration decreases with decreasing

temperature according to n_i^2/p in which the intrinsic carrier concentration (n_i) decreases much faster than the hole concentration (p). Accordingly, holes dominate the conduction and give rise to the exhaustion region where the Hall coefficient is positive. In the intermediate temperature range, the large mobility ratio between electrons and holes causes mixed conduction and the Hall coefficient changes its sign (at around $n = p\ (\mu_p / \mu_n)^2$ according to Eqn 7.6), going from negative in the electron-dominated region to positive in the hole-dominated region.

From the two experimentally measured quantities, namely the Hall coefficient and resistivity, the Hall mobility can be derived from Eqn. 7.3 and its temperature dependence is also shown in Fig. 7.2. At low temperatures, the Hall mobility reflects the drift mobility of the majority carriers and its value is therefore low because of the low mobility of the holes. As the temperature increases, the Hall mobility is further reduced by lattice scattering. This decrease is counteracted by the onset of intrinsic electron conduction at around 125K, giving rise to a sign reversal similar to the behaviour of the Hall coefficient. Above 200K, the Hall mobility starts to decrease as lattice scattering becomes important at high temperatures.

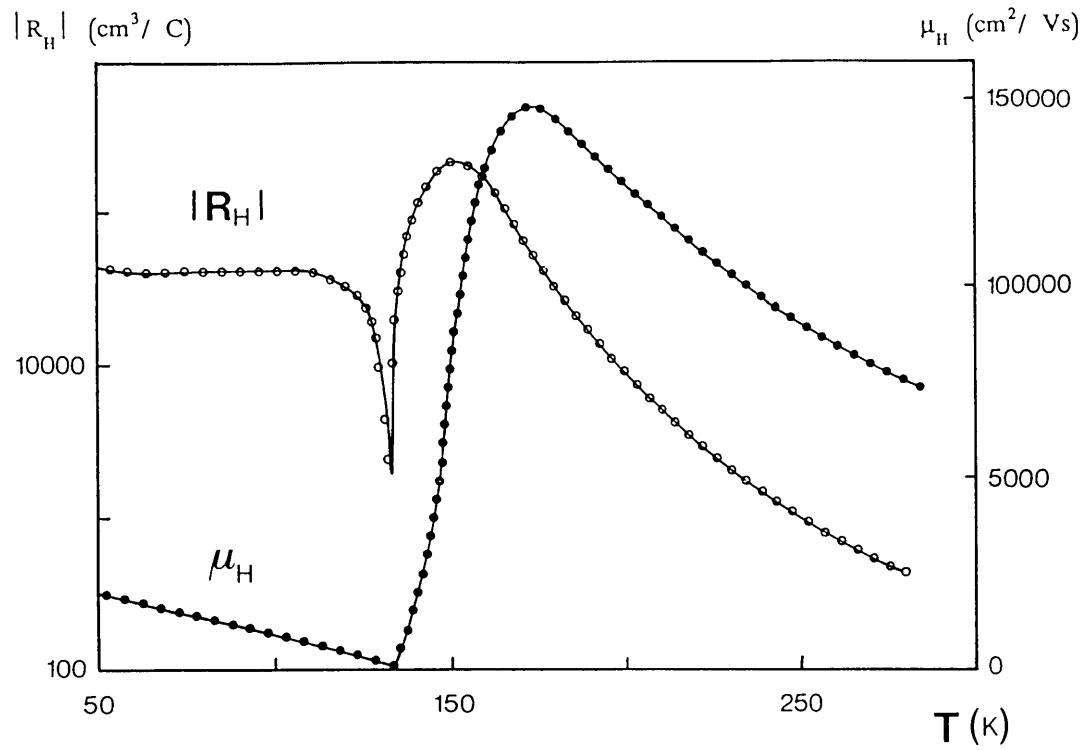


Fig. 7.2 A typical result of low-field Hall measurements for a p-InSb(100) substrate subjected to pre-growth cleaning procedures.

ii) Hall Measurements of α-Sn/p-InSb

As mentioned in chapter 4, the electrical properties of α-Sn epilayers depend very much on the details of substrate preparation prior to growth. Hall measurements showed that the extrinsic conduction of the epilayer could become p-type if the Ar ion bombardment energy used for substrate cleaning is too high (>500eV). Using an optimum substrate cleaning method (see chapter 4), structures consisting of unintentionally doped α-Sn films grown on p-InSb show a reproducible n-type Hall effect. Hall mobility as high as 9,000 cm^2/Vs at 4.2K with apparent carrier concentration corresponding to low 10^{17} cm^{-3} could be obtained. Due to the multi-carrier conduction mentioned earlier, it should be realized that these values do not truly reflect the electrical properties of the α-Sn epilayer.

The multi-carrier conduction effect can sometimes be manifested by anomalous temperature dependence of the Hall coefficient and Hall mobility where double reversals of sign are observed in both quantities as the material is cooled down from room temperature (see Fig. 7.3). Such anomalous behaviour is correlated with an apparently low Hall mobility. The reversal at about 130K is due to the freeze-out of intrinsic carriers in the InSb substrate which becomes p-type at low temperatures. The second reversal (at around 110K) is thought to be due to the increasing conductivity of the α-Sn epilayer or the 2DEG at the interface with respect to the p-InSb substrate as the sample cooled down. It should be emphasized that the apparent Hall mobility is anomalously low for samples showing such sign reversals of the Hall coefficient. The quality of the Shubnikov-de Haas peaks for these samples was as good as those having higher Hall mobilities (see § 7.3.3). Comparing our Hall data with the simulated results of Lou and Frye[181] shown earlier in Fig. 7.1 revealed a similarity between the α-Sn/p-InSb and a n-type skin layer on p-type substrate structures. In the simulated case, holes from the substrate are frozen out at low temperatures and electrons from the n-skin layer dominate the conduction, giving rise to the second crossover in the Hall coefficient and Hall mobility. A consequence of this behaviour is the increase in the low temperature mobility as the influence of the n-skin increases. Such an increase in Hall mobility is indeed observed in our sample as shown in Fig. 7.3. According to the simulation, the shape of the Hall coefficient and Hall mobility curve depends strongly on the ratio between the electron concentration in the skin layer (N_s) and

the hole concentration (N_A) of the substrate. A double crossover structure can only be observed if this ratio is high which is consistent with fact that our InSb substrate is only doped to 10^{14} cm^{-3}.

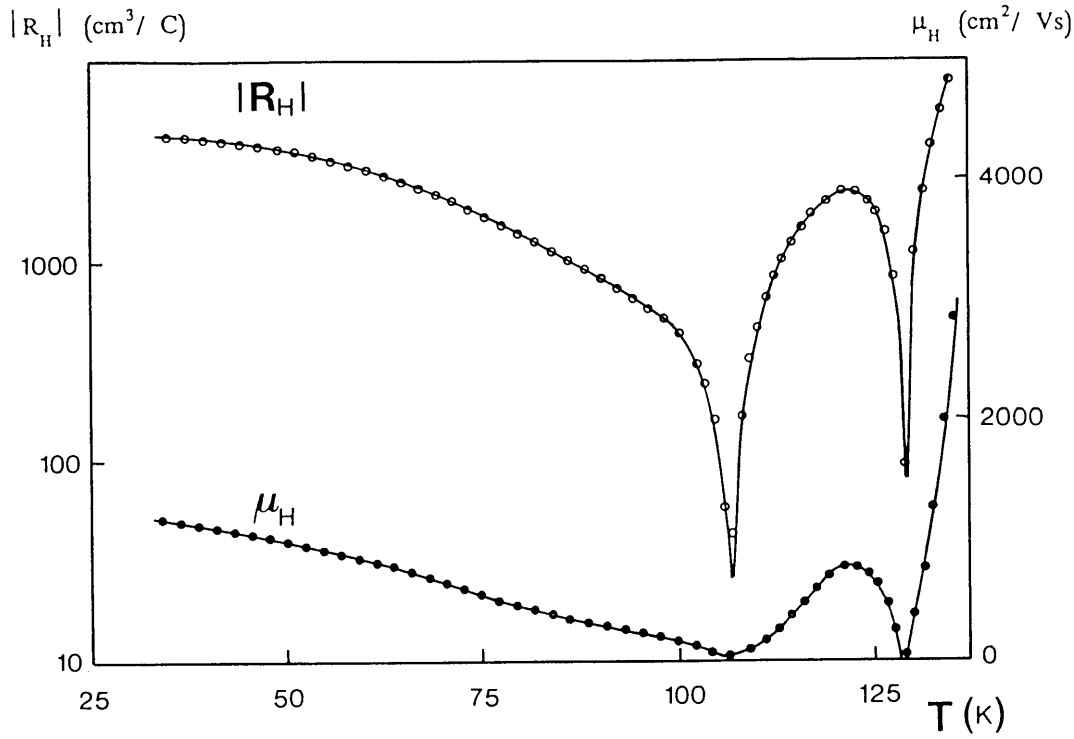


Fig. 7.3 Hall measurement for an ~2500Å thick α-Sn film grown on p-InSb
(Note that a double reversal of sign is observed in the temperature dependence of the Hall coefficient ($|R_H|$) and Hall mobility (μ_H).)

7.3 Shubnikov-de Haas (SdH) Effect Measurements

7.3.1 Basic Theory

a) Effect of Magnetic Field on Electrons in a Semiconductor

Case 1 : Three-dimensional (3-D) System

Within the effective mass approximation in which the effect of a periodic crystal potential is incorporated as a renormalization of electron mass, the influence of a magnetic field on an electron in an isotropic

semiconductor with parabolic bands is represented by the Hamiltonian :[188]

$$\hat{H} = \frac{1}{2m^*} \left(\hat{\mathbf{P}} - e\mathbf{A} \right)^2 \qquad (7.8)$$

where m^* is the renormalized effective mass, $\hat{\mathbf{P}}$ the momentum operator and $\mathbf{A}$ the magnetic vector potential.

For a semiconductor with spherical Fermi surfaces, it can be shown that the eigen-energies of the electrons (including spin) with magnetic field (B) applied along the z-direction are given by :[188]

$$E_N = \left(N + \frac{1}{2} \right) \hbar\omega_c + \left(\frac{\hbar^2 k_z^2}{2m^*} \right) \pm \frac{1}{2} g^* \mu_B B \qquad (7.9)$$

Here all energies are measured from the bottom of the conduction band. N is an integer, ω_c the cyclotron frequency given by $\omega_c = eB/m^*$, g^* the effective Landé g-factor, and $\mu_B = \frac{e\hbar}{2m_o}$ is the Bohr magneton.

The magnetic field thus has the effect of quantizing the electron motion in the plane perpendicular to itself, giving rise to a discrete series of energies known as the Landau levels[188] (first term on the right of Eqn. 7.9). Superimposed on this set of levels is a free motion in the field direction. In the E-k_z diagram, this can be represented by a family of quadratic parabolae shifted by $\hbar\omega_c$ relative to one another along the energy axis, with the lowest level $\frac{1}{2}\hbar\omega_c$ above the bottom of the band (see Fig. 7.4a). In fact, the field causes all the allowed energy states in the Fermi sphere to redistribute themselves on the surface of a set of coaxial cylinders parallel to k_z.[183]

In the absence of a magnetic field, the number of electron states per unit volume within an infinitesimal range of wave-vector k is given by :[183]

$$D(k)\, dk = 2 \frac{4\pi k^2 dk}{(2\pi/L)^3 \, L^3}$$

where L is the periodicity of the permitted states in each direction of real space and the factor of two is included to take account of the two possibilities for electron spin. From $E = \hbar^2 k^2 / 2m^*$,

$$D(E)\,dE = D(k)\,\frac{dk}{dE}\,dE$$

$$= \frac{m^*}{\pi^2\hbar^2}\,\frac{(2m^*E)^{1/2}}{\hbar}\,dE$$

$$\Rightarrow \qquad D(E) = \frac{1}{2\pi^2}\left(\frac{2m^*}{\hbar^2}\right)^{3/2} E^{1/2} \qquad (7.10)$$

Note that the 3-D density of states D(E) is proportional to the square root of the energy as depicted by the dotted line in Fig. 7.4b.

Application of a magnetic field will cause a redistribution of the density of states among the quantized Landau levels. The density of states $D_B(E)$ for the energy spectrum given by Eqn. 7.9 is discontinuous and follows the shape of[188]

$$D_B(E) \propto \left[\, E - (N + \tfrac{1}{2})\,\hbar\omega_c \,\right]^{-1/2} \qquad (7.11)$$

as depicted by the solid lines in Fig. 7.4b.

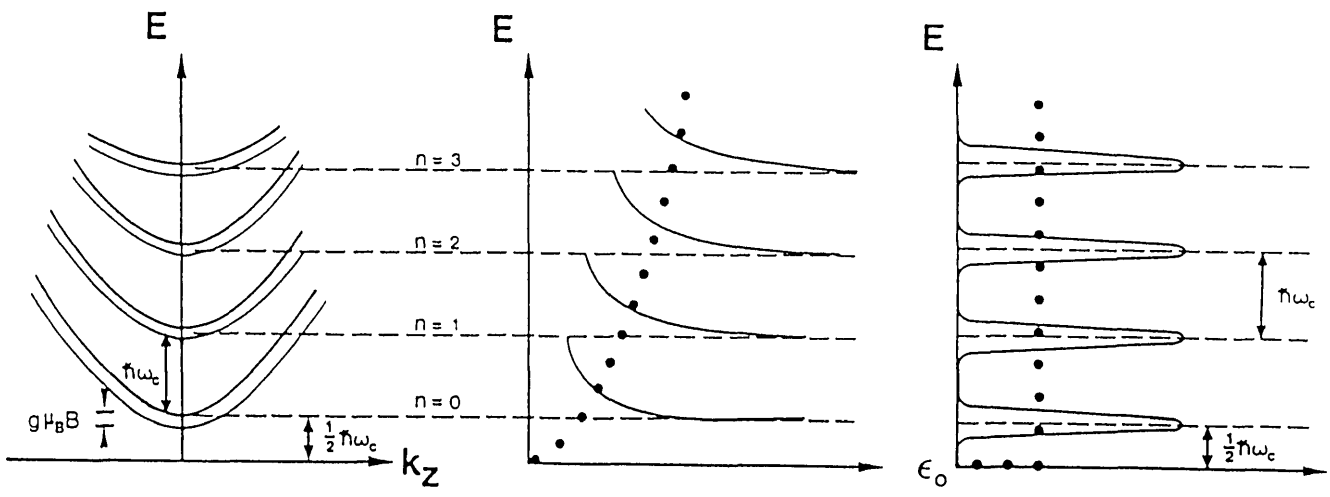


Fig. 7.4 Schematic representations of (a) the variation of energy with k_z in a 3-D system when a magnetic field B is applied in the z-direction, (b) the 3-D density of states as a function of energy when a magnetic field is applied (solid lines) and in the absence of the field (dotted line), and (c) the corresponding density of states for a 2-D system. Note that the density of states in the presence of a magnetic field (solid line) is broadened by scattering effects.

Case 2 : Two-Dimensional Electron Gas (2DEG)

In a two-dimensional (2-D) system, electrons are free to move in two spatial dimensions but their motion in the third, say the z-direction is constrained. This gives rise to the confinement of a two-dimensional electron gas (2DEG) in a one-dimensional potential well.[189,190] The eigen-states for the z-direction are quantized into a set of discrete levels known as electric subbands (ϵ_i), whereas those in the x-y plane will be essentially unmodified in the absence of a magnetic field. The eigen-energies for electrons in an isotropic 2-D system are thus given by :

$$E_i = \frac{\hbar}{2m^*} \left(k_x^2 + k_y^2 \right) + \epsilon_i \qquad (7.12)$$

This equation implies that a continuum of allowed states is associated with each electric subband ϵ_i with i = 0,1,2... The form of ϵ_i depends on the shape of the confining potential well which in turn depends on the origin of the 2DEG. Experimentally, a 2-D system can be realized in a number of different media such as semiconductor/oxide interfaces; modulation-doped heterostructures; surface accumulation or inversion layers; and ultrathin films etc..[189,190] For thin films and layered structures, electrons can be considered as being confined within a rectangular well whereas in the case of an inversion or accumulation layer, the potential well can be approximated by an 1-D triangular well.[190] In the $E(k_x)$ and $E(k_y)$ representation, the allowed states are parabolae whereas in the $E(k_z)$ plot, only points of allowed states are obtained.[190] The 2-D density of states D'(E) for one subband can be calculated from :

$$D'(k)\,dk = 2\,\frac{2\pi k\,dk}{(2\pi/L)^2\,L^2} = \frac{k}{\pi}\,dk$$

$$\Rightarrow \qquad D'(E)\,dE = \frac{k}{\pi}\,\frac{m^*}{\hbar^2 k}\,dE$$

$$\therefore \qquad D'(E) = \frac{m^*}{\pi\hbar^2} \qquad (7.13)$$

Note that the density of states is now energy independent in contrast to that in a 3-D system (c.f. Eqn. 7.10). The reduction in dimensionality also changes its shape from a parabolic variation to a stepped variation as represented by the dotted line in Fig. 7.4c.

When a magnetic field is applied along the z-direction which is perpendicular to the plane of the 2DEG, an infinite set of Landau levels associated with each electric subband will be introduced.[189,190] The total energy will now be completely quantized and will consist of terms representing both the Landau level quantization and the confinement of the potential well :

$$E_{N,i} = \left(N + \frac{1}{2} \pm \Delta \right) \hbar\omega_c + \epsilon_i \qquad (7.14)$$

Δ is the spin term where $\Delta\hbar\omega_c = \frac{1}{2} g^* \mu_B B \Rightarrow \Delta = \frac{g^* m^*}{4m_o}$.

As in the 3-D case, the density of states will become discontinuous and in the absence of any scattering, can be represented by a series of delta functions at the Landau level energies. In practice, the density of state function will be broadened by scattering as shown by the solid curves in Fig. 7.4c.

b) The Shubnikov-de Haas (SdH) Effect

As shown in the previous discussions, electrons are quantized into Landau levels in the presence of a magnetic field. As the magnetic field is varied, these Landau levels will pass through the Fermi level (E_F) which is almost independent of the field.[182] For a degenerate semiconductor, the conduction properties are dominated by electrons close to the Fermi level which is high up in the conduction band. The scattering probabilities of these electrons will be affected by the sudden change in the density of states when the bottom of a Landau level coincides with the Fermi level, i.e. when

$$E_F = \left(N + \frac{1}{2} \pm \Delta \right) \frac{\hbar e B}{m^*} \qquad (7.15)$$

This gives rise to a series of oscillations in the magnetoresistance known as the Shubnikov de-Haas (SdH) effect from which important parameters of the carriers can be obtained directly. Carrier concentration and band anisotropies can be deduced from the field position of the peaks; temperature and field dependence of the oscillation amplitudes provide information about the effective mass and mobility of the carriers; and the g-factor can be found from the spin-splitting of the peaks.[180] In this work, however, only the carrier concentration will be extracted from SdH effect

measurements.

According to Fermi-Dirac statistics, the carrier concentration (n) is given by :[183]

$$n = \int_0^\infty D(E)\ f(E)\ dE \tag{7.16}$$

where f(E) is the expectation of occupancy of a state with energy E and D(E) the density of states. For a degenerate semiconductor of which the conduction properties are dominated by the varying occupancy of states at the Fermi energy E_F, Eqn. 7.16 can be reduced to :[183]

$$n = \int_0^{E_F} D(E)\ dE \tag{7.17}$$

Case 1 : 3-D Systems

For a 3-D system, the carrier concentration can be found from Eqns. 7.10 and 7.17 giving

$$n = \frac{1}{3\pi^2}\left(\frac{2m^*}{\hbar^2}\right)^{3/2} E_F^{3/2} \tag{7.18}$$

$$\Rightarrow E_F = \frac{\hbar^2}{2m^*}\left(3\pi^2 n\right)^{2/3} \tag{7.19}$$

SdH oscillations will occur when the Landau levels coincide with the Fermi level, i.e. when

$$E_F = \frac{\hbar}{2m^*}\left(3\pi^2 n\right)^{2/3} = \left(N + \frac{1}{2} \pm \Delta\right)\frac{\hbar e B}{m^*} \tag{7.20}$$

For two successive quantum numbers N, we obtain

$$\frac{1}{B_N} - \frac{1}{B_{N+1}} = \Delta\left(\frac{1}{B}\right) = \frac{\hbar e}{m^* E_F} \tag{7.21}$$

$$\therefore \quad \Delta\left(\frac{1}{B}\right) = \frac{2e}{\hbar}\left(3\pi^2 n\right)^{-2/3} \tag{7.22}$$

Note that the SdH oscillations are periodic in reciprocal magnetic field and the oscillation period $\Delta(1/B)$ is independent of the effective mass. The carrier concentration (n) can thus be obtained directly from this period

without the uncertainty associated with the estimation of the Hall factor[180] (r_H) as discussed in § 7.2.1.

Case 2 : 2-D Systems

SdH oscillations are more pronounced in a 2-D system due to a more abrupt change in the density of states at the Fermi level. In the case where more than one electric subband is occupied, each will contribute to a distinct series of oscillations periodic in 1/B.[182,190] The carrier concentration of each subband (n_i) can be deduced from the corresponding oscillation period $\Delta(\frac{1}{B})_i$ as follows :

from Eqn. 7.21 $$\Delta(\frac{1}{B}) = \frac{\hbar e}{m^* E_F}$$

from Eqns. 7.13 & 7.17 $$n = \int_0^{E_F} D'(E)\, dE = \frac{m^* E_F}{\pi \hbar^2}$$

$$\therefore \quad \Delta(\frac{1}{B})_i = \frac{2e}{n_i \hbar} \tag{7.23}$$

At sufficiently high magnetic fields, magnetoresistance spectra may be complicated by structures arising from spin-splitting of the Landau levels. Great care must thus be taken when interpreting the SdH results.

In order to observe the SdH effect, the requirements $\hbar\omega_c \gg k_B T$, $E_F \gg k_B T$ and $\omega_c \tau \gg 1$ have to be satisfied.[191] Here τ refers to the lifetime of a quantum state and k_B the Boltzmann's constant. In practice, these requirements place stringent demands on the magnetic field strength and the quality of the semiconductor sample.

c) Tilted Field and Diamagnetic SdH Effects

All discussions so far have implicitly assumed that the magnetic field is aligned perpendicular to the plane of the 2DEG (i.e. along the z-direction). In the presence of a magnetic field having an in-plane component, the electric and magnetic quantization are mixed in a complex manner.[182] Cyclotron orbits will be constrained by the confining potential to remain in the plane of the 2DEG and the Landau level splitting will be

determined solely by the perpendicular component of the field $B_\perp$ (= Bcosϑ where ϑ is the tilt angle with respect to the normal of the 2DEG plane). Using a perturbation approach, it can be shown that the eigen-energies of electrons under the influence of a tilted magnetic field are given by :[182]

$$E_{N,i} = \left(N + \frac{1}{2}\right) \frac{\hbar e B_\perp}{m^*} \pm \frac{1}{2} g^* \mu_B |\mathbf{B}| + \epsilon_i + \frac{e^2 B_\parallel^2}{m^*} \langle \Delta z_i \rangle^2 \quad (7.24)$$

where $B_\perp$ and $B_\parallel$ are the perpendicular and parallel components of the magnetic field **B** with respect to the plane of the 2DEG and $\langle \Delta z_i \rangle^2$ represents the extent of the electronic wave-function of the i^{th} subband in the z-direction.

On tilting the magnetic field, SdH peaks arising from a perfect 2DEG will move upwards in field as 1/cosϑ. On the other hand, bulk oscillations depend on the total value of the magnetic field and are unaffected by the change in ϑ. The 1/cosϑ dependence of the SdH oscillations is thus characteristic of the two-dimensionality of the carriers.[189,191] The spin energy, given by the second term on the right hand side of Eqn. 7.24, also depends on the total field and hence the spin effect will become more pronounced as the ratio of spin-splitting to Landau level splitting increases with 1/cosϑ (see Fig. 7.5)[181,191]

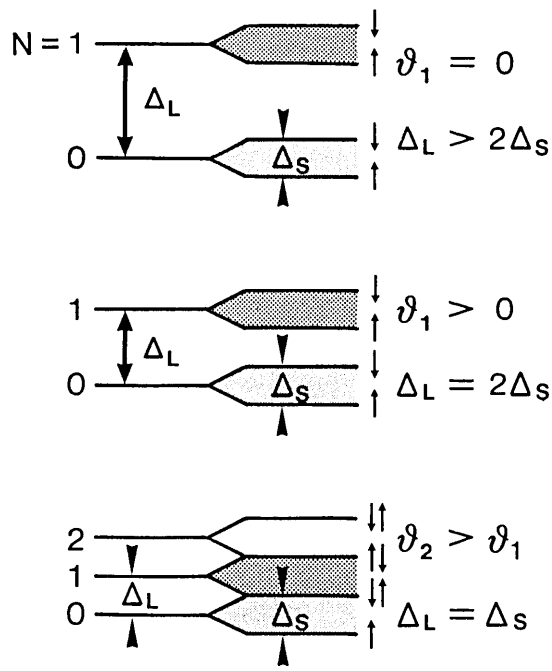


Fig. 7.5 Relationship between Landau level splitting (Δ_L) and spin-splitting (Δ_S) of a 2DEG for various tilt angles ϑ (from Ref. 188)

The last term in Eqn 7.24 represents a diamagnetic shift of the subbands and accounts for the only change in the energy of the 2DEG at parallel field (i.e. $\vartheta = 90^{\circ} \Rightarrow B_{\perp} = 0$). Due to the spatial extension of the electron wave-functions, the subband minima will be shifted with respect to $k_{\parallel} = 0$ and raised in energy as the magnetic field ($B_{\parallel}$) increases.[182] Here $k_{\parallel}$ is the component of a wave-vector in the plane of the 2DEG. This energy shift will move each subband successively up through the Fermi level, causing them to depopulate and redistribute their carriers among lower lying subbands. As a result, the magnetoresistance will go through a series of maxima and minima due to the successive reduction of inter-subband scattering. This behaviour will produce a series of widely-spaced peaks which are not periodic in 1/B and is called the "diamagnetic Shubnikov-de Haas effect".[191] This effect can give valuable information about the number of subbands occupied, which is particularly useful when unambiguous results cannot be obtained from the normal SdH effect. At some intermediate angles, the change in subband separation caused by the parallel component of the magnetic field can shift the Landau levels of higher subbands into coincidence with those of the lower subbands.[192] Any mixing of these degenerate levels can lead to hybridized behaviour in the periodicity of the SdH series.

7.3.2 Experimental Techniques

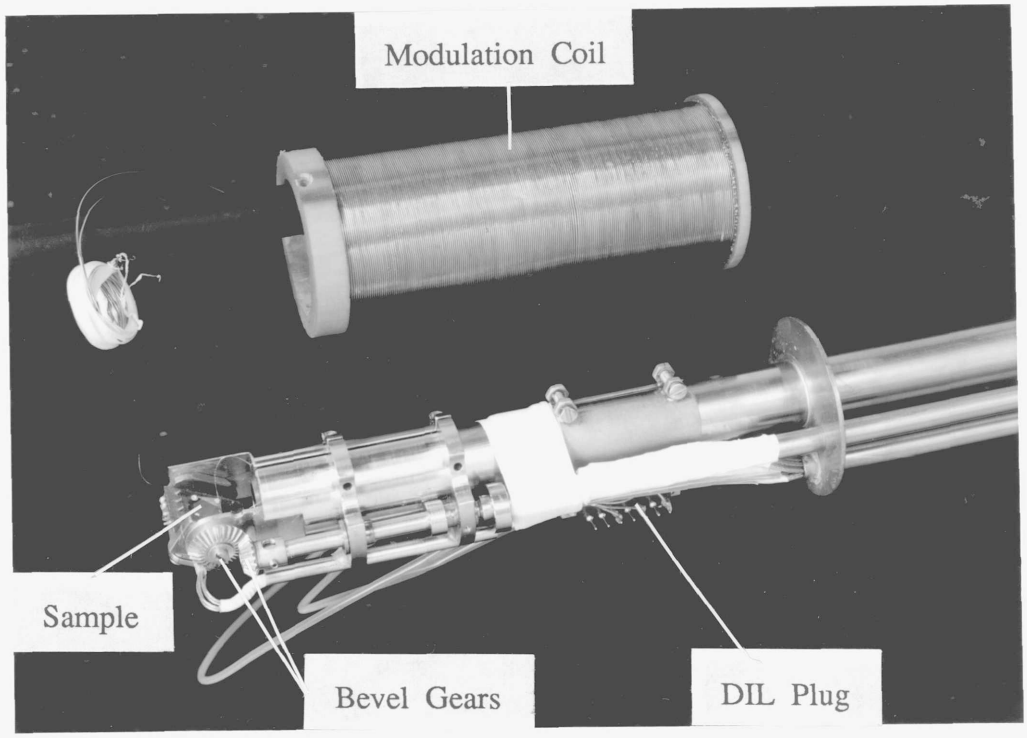
All SdH and magneto-optical experiments were performed at liquid helium temperature (4.2K) in a double superconducting magnet system (Thor Cryogenics Ltd.) using the 8T coil. Samples were introduced into the bore of the superconducting solenoid via a cryogenic insert enclosed in a stainless-steel sleeve. Good thermal contact between the liquid helium bath and the sample was facilitated by filling the sleeve with helium gas (at P = 1 atm.). A rotatable insert (shown in Fig. 7.6) was designed for tilted field experiments such that the tilt angle could be varied while maintaining the integrity of the cryogenics. Since the magnetic field is along the length of the insert, bevel gears had to be used to rotate the surface plane of the sample in and out of the field. The sample holder was constructed from a block of Tufnol with eight pins for electrical connections which were terminated in a standard DIL plug further up the insert. The sample holder together with its stainless-steel support is removable from the main insert to facilitate sample changing procedures. A series of thin copper baffles

was placed along the length of the insert (not shown in the picture) to reduce helium boil off due to radiation from the 300K end. Electrical leads using sub-miniature coaxial cables were connected to Lemo type connectors on the top end of the insert. Coaxial cables of stainless-steel construction were used in an attempt to minimize conductive heat loss down the insert. For magneto-optical experiments, the sample could be illuminated down a light-pipe placed in the centre.

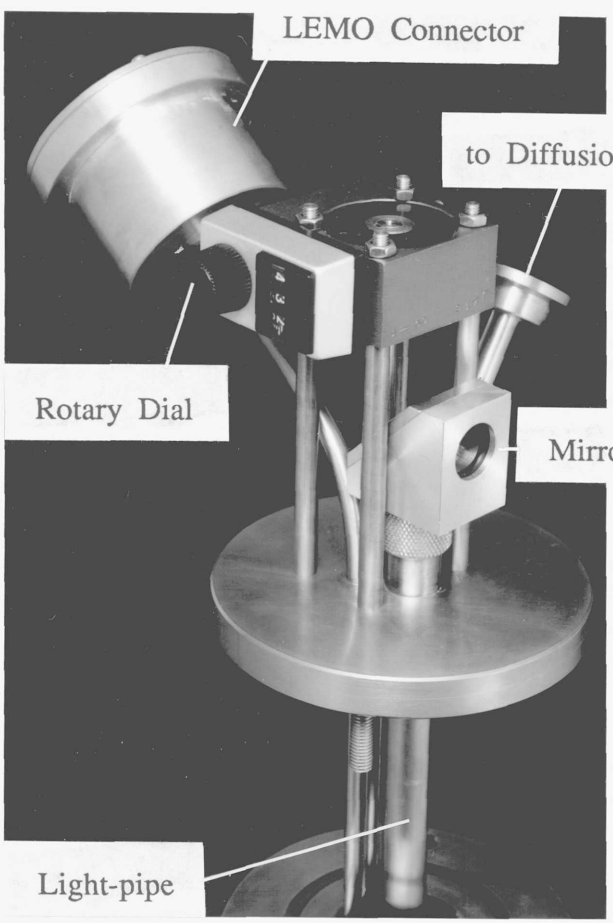
In SdH experiments, the transverse resistivity ρ_{xx} of the sample is measured as a function of the applied magnetic field. For d.c. measurements, a known current was passed between a pair of neighbouring contacts and the voltage generated across the other pair was recorded while the field was swept. A constant current source was built from a batch of 15V batteries and two potential dividers. Automatic data acquisition was accomplished by the use of an Amstrad 1512 micro-computer equipped with standard IEEE interface. Turbo Pascal routines were used to drive two digital voltmeters (Keithley 195A) which measured the sample resistance and a voltage proportional to the magnetic field. SdH oscillations arising from a 2DEG with more that one subband occupied are seen as a superposition of oscillations from separate subbands as discussed in the previous section. In most cases, it is extremely difficult to extract individual subband carrier densities from the raw magnetoresistance data. Instead, the data must be analyzed by a Fourier technique which yields a series of peaks corresponding to individual subband carrier densities. A Fast Fourier Transform (FFT) algorithm together with numerical averaging and differentiation routines are available to facilitate data analysis.

In most measurements, the oscillatory components of the longitudinal resistivity are masked by a strong magnetoresistance background arising from multi-carrier conduction effects and could be of the order of only 1% of the measured resistivity. In those situations, a field modulation technique using a modulation coil was employed to suppress the slowly varying background magnetoresistance. As the d.c. field from the 8T magnet was swept, a small oscillatory magnetic field of much smaller amplitude was applied colinearly. The modulation coil (shown in Fig. 7.6a) was made by winding multi-filament NbTi superconducting wire (~0.352mm dia.) round a smooth Tufnol tube insulated with a layer of thin Mylar tape. The diameter of the Tufnol tube (29mm) was chosen such that it could fit between the

(a)



(b)



(c)

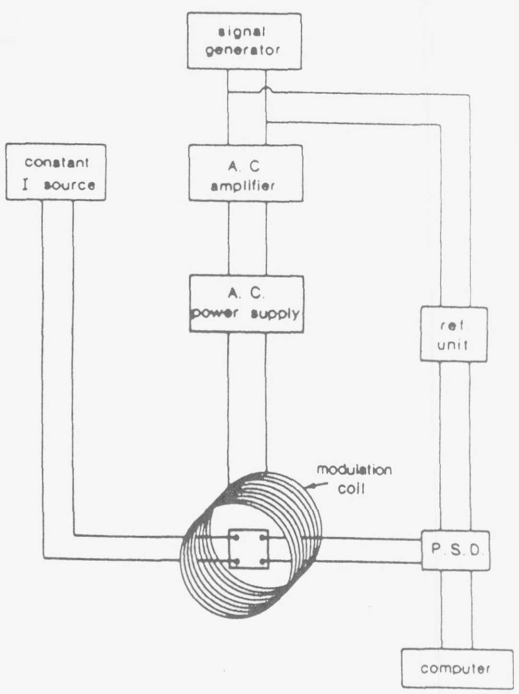


Fig. 7.6 Apparatus used for SdH and magneto-optical experiments :

(a) Sample holder of the rotatable insert and the modulation coil

(b) Top end of the insert showing the mirror box connecting the light-pipe to the laser system, the rotary control and the electrical connectors

(c) Circuitry for driving the modulation coil in a.c. SdH measurements.

sample holder end of the insert and the stainless-steel sleeve. The coil was positioned such that its centre coincided with that of the 8.3T magnet coil. Winding of the solenoid was achieved by tensioning the superconducting wire and rotating the tube in a lathe. As winding progressed, each completed layer was thoroughly coated in low temperature Stycast epoxy resin and a total of four layers was wound. The modulation coil was driven by a 120W audio power amplifier protected by two zener diodes. Using a modulating frequency of 35Hz and a supply voltage of 1V across the coil, a magnetic field of approximately 0.005T could be generated. Using a phase sensitive and lock-in detection technique, a d.c. output signal proportional to the first derivative of the magnetoresistance could be recorded. An a.c. preamplifier was also used to improve the signal to noise ratio of the output. Circuitry used for a.c. SdH measurements is schematically shown in Fig. 7.6c.

7.3.3 Results and Discussions

α-Sn films grown on InSb substrates showed very high magnetoresistance characteristic of multi-carrier conduction.[180] Fig. 7.7a indicates that the SdH oscillations observed from a α-Sn/p-InSb layer at liquid helium temperature produced a relatively small modulation of the monotonic magnetoresistance (marked by arrows) and the field modulation technique was required to suppress the slowly varying background magnetoresistance. Fig. 7.8a shows typical recordings using this technique for films of various thicknesses with the magnetic field applied perpendicular to the sample.[55] Note the remarkable difference between the peak structures observed from the thin (200Å) and thick (3000Å) films. The rather complicated magnetoresistance was found to be a superposition of several SdH series which could be attributed to the presence of a high density 2DEG. Due to the complexity of the oscillatory structures, Fast Fourier Transform (FFT) analysis was required to determine the 1/B periodicity and to identify individual subbands. The corresponding FFT power spectra shown in Fig. 7.8b reveal the presence of a series of strong maxima. For the α-Sn/p-InSb($\bar{1}\bar{1}\bar{1}$) film, as many as nine subbands were occupied with a total occupancy of ~ 7.5×10^{12} cm^{-2}. The carrier concentrations are very high and it is believed that the 2DEG is located at the α-Sn/InSb interface rather than the surface. The presence of surface states in α-Sn has not been reported and is thus believed to be insignificant. The variation of total carrier concentration

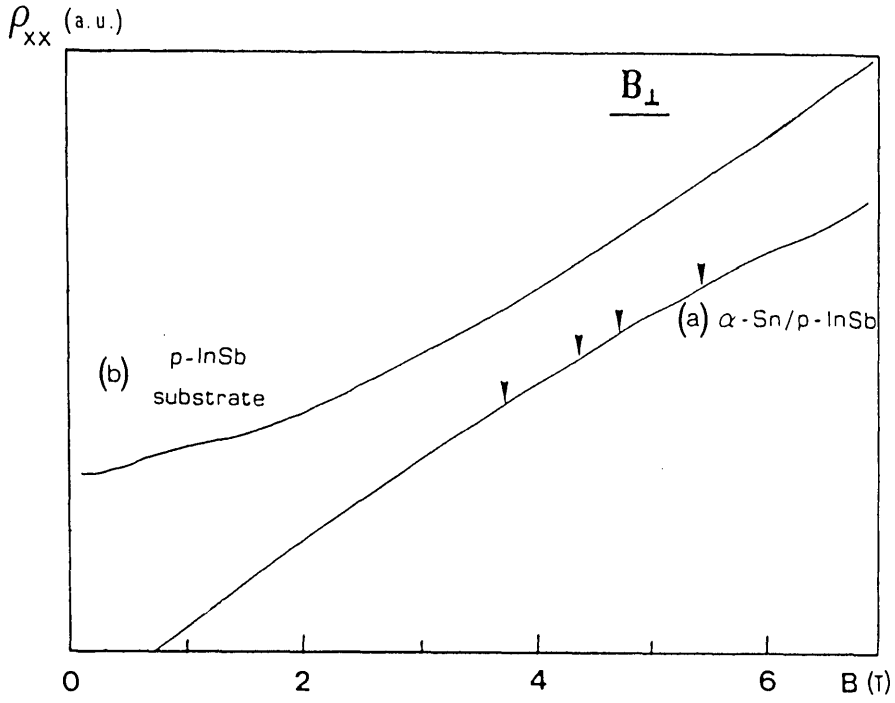


Fig. 7.7 D.C. magnetoresistance recordings taken at 4.2K with the magnetic field perpendicular to the growth plane for :

(a) an ~3000Å thick α-Sn film grown on p-InSb(100) and

(b) a p-InSb(100) substrate subjected to pre-growth cleaning procedure

TABLE 7.1

Sample *	Overlayer Thickness (Å)	Carrier Concentrations (x 10^{12} cm^{-2})								
		n_0	n_1	n_2	n_3	n_4	n_5	n_6	n_7	Σn_i
Sn-48p	200	1.55	1.09	0.71	0.50	0.31	0.18			4.16
Sn-39p	1500	1.90	1.37	0.94	0.64	0.41	0.25			5.50
Sn-32p	2000	1.97	1.37	0.94	0.67	0.41	0.23	0.16	0.11	5.58
Sn-41p	3000	1.90	1.43	1.02	0.69	0.46	0.26	0.21	0.13	6.10
	etched in HCl for 2 mins.	1.66	1.19	0.85	0.58	0.39	0.27	0.19	0.10	5.23
Sn-26p	3000	2.2	1.55	1.09	0.76	0.47	0.32	0.24	0.17	6.40
Sn-27p	3500	2.03	1.38	0.97	0.60	0.37	0.25	0.08		5.68
Sn-42p	4000	1.68	1.23	0.80	0.46	0.30	0.21	0.11		4.45
Sn-31p(111)	1500	2.18	1.61	1.20	0.89	0.66	0.46	0.33	0.14	7.46

* all samples were grown on p-InSb(100) substrates unless otherwise stated

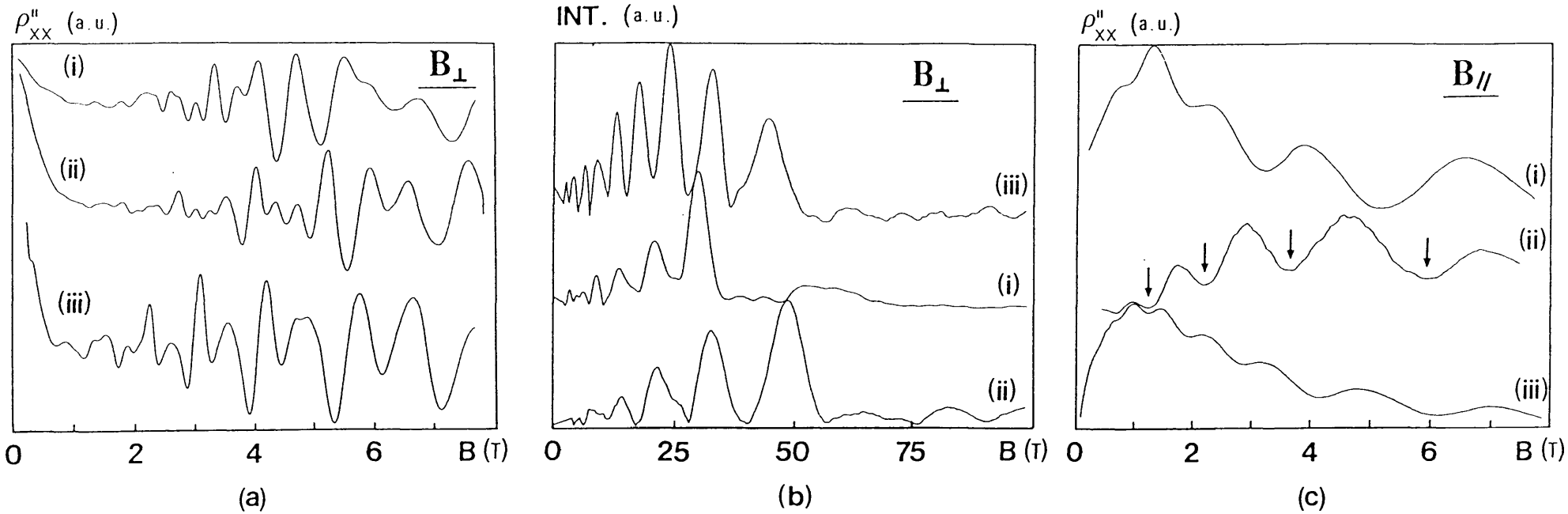


Fig. 7.8 Experimental recordings from a.c. SdH measurements showing :

(a) Second derivatives of the magnetoresistance recorded at 4.2K with the magnetic field perpendicular to the growth plane for (i) 200Å and (ii) 3000Å thick α-Sn films grown on p-InSb(100), and (iii) 1200Å thick α-Sn film grown on p-InSb$(\overline{111})$

(b) Corresponding FFT power spectra for these three samples

(c) Corresponding diamagnetic resonances spectra recorded with magnetic field parallel to the growth plane. Note that the depopulation fields of individual subbands are indicated by the arrows.

and subband occupancy for several samples with different overlayer thicknesses and substrate orientations are summarized in Table 7.1. When the magnetic field was applied parallel to the sample surface i.e. parallel to the plane of the 2DEG, series of more widely-spaced peaks without 1/B character were observed due to the depopulation of successive subbands. This "diamagnetic SdH effect" shown in Fig. 7.8c demonstrates consistently the presence of a large number of subbands in all of these films. Depopulation fields of individual subbands are marked by arrows in the diagram.

Confinement of the conduction electrons is further evidenced from the results of tilted magnetic field experiments in which the magnetic field is rotated to a variable angle ϑ with respect to the normal of the growth plane.[47] As mentioned before, fundamental fields in the SdH series for a true 2DEG should increase as $1/\cos\vartheta$, i.e. the separation of the Landau levels should decrease with increasing ϑ. Fourier-transformed results of tilted field measurements performed on an α-Sn/p-InSb(111) sample are shown in Fig. 7.9 with the fundamental field scaled to $B\cos\vartheta$. Note that the field position and hence the occupancy of each subbands depends strongly on the orientation of the magnetic field. For $\vartheta \leq 45^{\circ}$, the dependence is close to $1/\cos\vartheta$ (dashed lines in Fig. 7.9) which confirmed the two-dimensionality of the electron gas. Above this angle, some peaks start to merge together (marked by arrows in the figure). This behaviour may arise from the mixing between Landau levels belonging to two adjacent electric subbands[192] or from the decrease of Landau level splitting with respect to spin splitting[190] (refer to § 7.3.1c and Fig. 7.5). Similar results were observed from α-Sn layers grown on InSb(100) substrates.

Having confirmed the existence of a 2DEG in the α-Sn/InSb layer, the next question to be answered would be the origin of this 2DEG. Zheng *et. al.*[115] observed a low carrier density 2DEG in an InSb/CdTe heterostructure and suggested the possibility that it arose from a n^+ region in the substrate. These workers conducted their Ar ion bombardment at 500eV which is higher than the energy we used for cleaning our InSb substrates.[55] Our substrates subjected to the usual cleaning procedure without subsequent epitaxial growth do not exhibit any SdH oscillation as shown in Fig. 7.7b. This demonstrates that the 2DEG in our α-Sn/InSb layer is unlikely to be caused by substrate cleaning artefacts. The charge density of the 2DEG seems to be affected by the thickness of the α-Sn overlayer in a complex manner as

shown in Table 7.1. For films grown on InSb(100) substrates, the charge density increases with overlayer thickness for films less than 3000Å thick, while the opposite trend occurs when this thickness is exceeded. On reducing the thickness of a 3000Å film by etching the surface with HCl for 2 mins., the total charge density was found to fall by about 10%. One possible explanation for these observations is that the thickness dependence of the dielectric constant of epitaxial α-Sn causes a corresponding variation in the shape of the potential well confining the 2DEG.[8] In addition, dielectric effects can also alter the potential of the well via the image force.

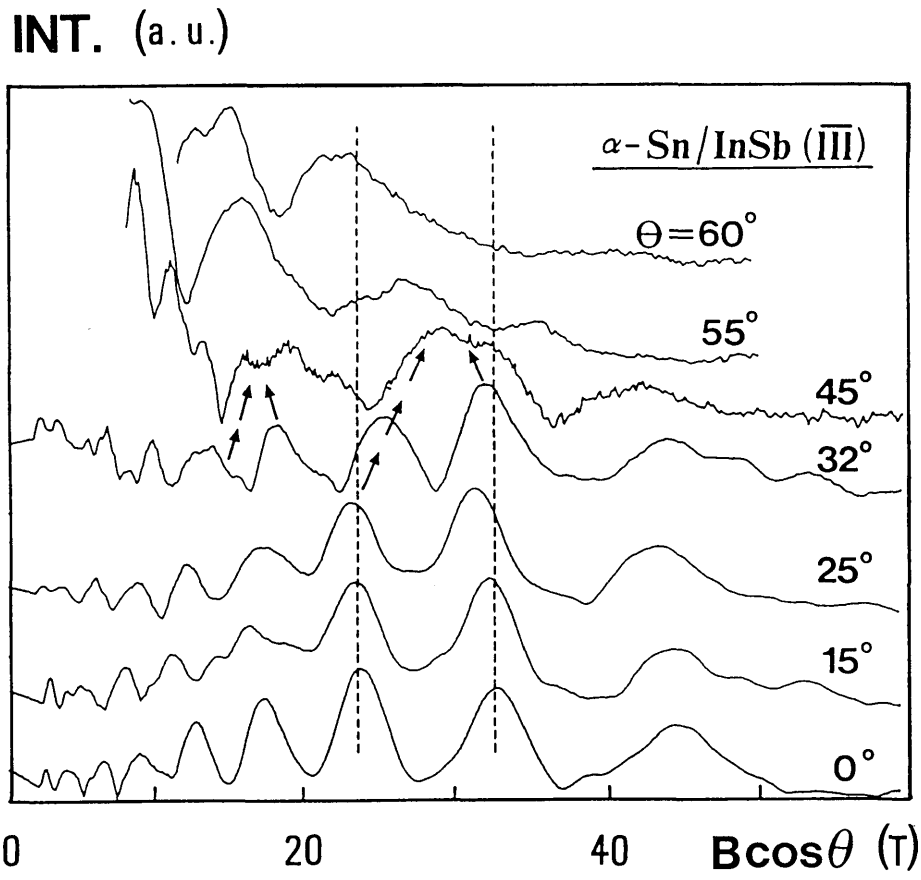


Fig. 7.9 Tilted-field FFT power spectra for an α-Sn/p-InSb(TTT) sample
The fundamental fields for the subbands have been scaled to Bcosϑ where ϑ is the tilt angle of the magnetic field with respect to the normal of the growth plane. For a true 2DEG, the peaks should follow the dashed lines. Note that from about ϑ = 45° onwards, some peaks start to merge together as marked by the arrows.

Two-dimensional behaviour has also been detected in SdH oscillations observed in thin α-Sn films (~800Å) grown on CdTe(001) by Song *et. al.*.[53] It was assumed that the carriers are confined in a potential well which is approximately rectangular in shape, giving rise to quantum size effects. In this case, the difference of consecutive subband energies as well as their occupancy difference should increase with decreasing film thickness[190] and is indeed observed by Song *et. al.*.[53] On the contrary, Fig. 7.8b indicated that the reverse trend is true for our α-Sn/InSb layers and the ratio of the subband occupancies n_i/n_{i+1} is relatively constant (~ 1.4 as listed in Table 7.1) for a wide range of film thicknesses. Quantum size effects thus cannot be fully responsible for the observed SdH results.

Carrier confinement can also arise from band-bending effects at the interface of the α-Sn/InSb heterostructure. At 4.2K, the Fermi levels for α-Sn and p-InSb (low doped to 10^{14} cm^{-3}) are about 20meV and 1meV above the valence bands of the two materials respectively (see Eqn. 7.19). The first figure is estimated from Hall measurements, which gives an apparent electron concentration of 10^{17} cm^{-3} for the α-Sn layer. From core level photoemission studies, the valence band offset for the α-Sn/InSb(100) heterostructure was estimated to be 400 ± 60 meV.[36] Using this value, the difference in Fermi level of the two materials in vacuum will be about 420 ± 60 meV as depicted in Fig. 7.10a. Because of the high carrier concentration of the α-Sn overlayer, most of the band bending will occur in the InSb substrate with the space charge region extending for more than 1000Å into the bulk (Fig. 7.10). It is therefore unlikely that the observed 2DEG, which obeys the $1/\cos\vartheta$ rule in tilted magnetic fields with ϑ up to 45°, arises from carrier confinement within the space charge region depicted in the figure.

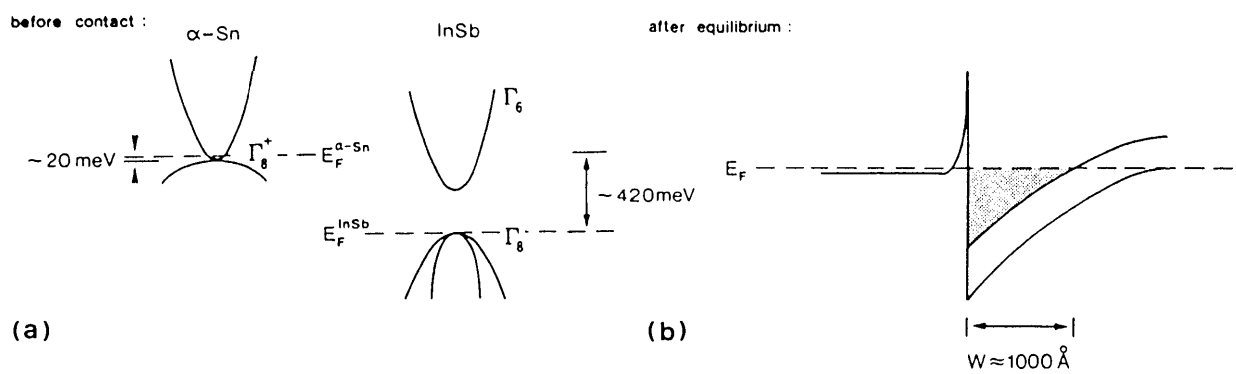


Fig. 7.10 Schematic diagram showing the band-bending effect in α-Sn/p-InSb(100) heterostructures

On the other hand, Fig. 7.10 is very much an over-simplified representation of the α-Sn/InSb interface which can be complicated by factors such as :

a) Pseudomorphically grown α-Sn films are highly-strained and the symmetry-induced degeneracy of the conduction and valence band in bulk samples is expected to be lifted. A finite bandgap should therefore exist in epitaxial α-Sn layers and the band-bending depicted in Fig. 7.10 is no longer valid.

b) Due to the non-polar/polar nature of the α-Sn/InSb(100) system, a large concentration of interface states may be present which may alter the interfacial potential substantially.[104]

In both cases, the interfacial band structure will be very complicated and carrier confinement may occur at both sides of the heterojunction. Since information regarding the band structure of epitaxial α-Sn, both theoretical and experimental, is very limited, it is difficult to rule out any of these possibilities at this stage.

In chapter 3 it was mentioned that cross-doping artefacts originating from both sides of the heterojunction could give rise to a 2DEG with the observed charge density as in δ-doped samples. Indeed, there is some evidence (§ 5.4.3) that Sb segregation can occur at the α-Sn/InSb interface when elevated growth temperatures or slow growth rates are used.

7.4 Far Infrared (FIR) Magneto-optical Measurements

In order to understand more about the nature of the 2DEG as well as the properties of the carriers in the bulk α-Sn films, high resolution magneto-optical measurements were carried out in the far infrared (FIR) region. It is hope that these experiments can shed some light on the origin and the location of the 2DEG through the determination of the effective masses involved in the conduction of the α-Sn/p-InSb system.

7.4.1 Basic theory

The phrase "magneto-optical measurements" was first used by Zeeman to describe optical experiments on atoms in a magnetic field. As already shown

in § 7.3.1, a magnetic field introduces Landau levels in the energy bands and most magneto-optical experiments are concerned with transitions between these Landau levels. In order to discuss all the possible transitions, the eigen-energies for bulk electrons in a magnetic field expressed in Eqn. 7.9 is rearranged to the form :

$$E_N^c = E_g + \left(N + \frac{1}{2} \right) \hbar\omega_c^c + \left(\frac{\hbar^2 k_z^2}{2m^{*c}} \right) \pm \frac{1}{2} g^{*c} \mu_B B \qquad (7.25)$$

where E_g is the bandgap of the semiconductor and the superscript (c) denotes the conduction band. All energies are now measured from the top of the valence band. A similar relationship exists for electrons in a simple, non-degenerate valence band :

$$E_N^v = - \left(N + \frac{1}{2} \right) \hbar\omega_c^v + \left(\frac{\hbar^2 k_z^2}{2m^{*v}} \right) \pm \frac{1}{2} g^{*v} \mu_B B \qquad (7.26)$$

For intraband magneto-optical transitions, the peaks in the 3-D density of states depicted in Fig. 7.4b become sharp optical features corresponding to transitions between Landau levels in the same band. Depending on the photon energy (ω) available for excitation, several types of transition can be observed such as :

a) Cyclotron resonance (CR) which occurs at $\omega = \omega_c$ for spin conserved $N \rightarrow N+1$ transitions and from which information about the effective mass of carriers can be deduced. In practice, scattering of electrons is inevitable and the linewidth of a CR peak is determined by the electron lifetime (τ). Distinctive cyclotron resonance can be resolved only if $\omega_c \tau \gg 1$ such that an electron can move through a significant part of its cyclotron orbit before being scattered.[183]

b) Spin resonance which occurs at $\omega = \omega_s = |g^*| \mu_B B$ for spin reversed $N \rightarrow N$ transitions. Being a magnetic dipole transition, the intensity of spin resonance is, in general, weaker than that of cyclotron resonance.

c) Combined resonance which is only allowed in semiconductors with zinc-blende structures such as InSb for spin reversed $N \rightarrow N+1$ transitions occurring at $\omega = \omega_c + \omega_s$. This kind of transition can be significant when spin-orbit coupling is large as is the case with narrow bandgap semiconductors which are generally heavy elements.

In addition to intraband transitions, transitions from Landau levels in

the valence band to those in the conduction band can also occur. Several interband transitions among levels of different N and different spin may be observed and thus many independent measurements of the conduction and valence band parameters may be extracted. In particular, these transitions may be extrapolated back to the zero-field condition from which a more accurate value of the bandgap (E_g) can be deduced (see Eqns. 7.25 and 7.26).

In the case of a 2DEG arising from space charge effects where a set of Landau levels is associated with each subband, only intraband cyclotron resonance between adjacent Landau levels tends to be of experimental importance.[188]

For the α-Sn/p-InSb system, transitions originating from hole bands in the substrate can also be observed as will be seen later. Following Pidgeon and Brown's scheme,[193,194] energy levels for holes in a magnetic field are classified into Landau ladders *a* and *b*, where loosely speaking, *a* and *b* correspond to "spin-up" and "spin-down" levels respectively. Hereafter, the notations - N*a*, + N*a*, - N*b*, + N*b* will be used where N denotes the quantum number of the Landau level. Since the Landau levels associated with each hole band contain a strong mixture of light hole and heavy hole band character, the signs - and + are used simply to distinguish the set of ladders with wider energy separations (hence light-hole-like) and those with narrower separation (hence heavy-hole-like) respectively.

At low temperatures, such as 4.2K used in our experiments, free holes are frozen out onto acceptor sites and excitations involving acceptor impurity or bound-hole states dominate over free-hole transitions. The standard approach for the treatment of impurity states in the presence of an external magnetic field is to use the effective mass approximation. The following discussions on bound-hole transitions in InSb are based on the analysis of Lin-Chung and Henvis,[194] who extended the standard method to include details of the InSb band structure. Because of the degeneracy of the valence band structure, acceptor states in a magnetic field exist in association with both heavy- and light-hole Landau levels. At low temperatures, it is expected that the excited acceptor state would be the final state of a hole transition originating from a ground acceptor state. Transitions to the continuum levels are not expected to dominate since the transition probabilities to states in the continuum are weak and decrease

with increasing field.[195] The zero-field acceptor ground state binding energy can be extracted from low temperature data by considering all the field contributions to the bound-hole transition energy ($\hbar\omega$) which is given by :[195]

$$\hbar\omega = E_a^g(0) + \Delta E_a^g(B) + E_{lh}^{a,b}(N,B) - E_a^e(B) \qquad (7.27)$$

where $E_a^g(0)$ is the binding energy of the acceptor ground state, $\Delta E_a^g(B)$ the field-induced shift of the ground state energy, $E_{lh}^{a,b}(N,B)$ refers to the energy of the N^{th} light-hole Landau level in ladder *a* or *b*, and $E_a^e(B)$ is the binding energy of the excited light-hole acceptor state (i.e. the final state for the transition). Since $\Delta E_a^g(B)$ and $E_a^e(B)$ are small quantities of comparable magnitude and opposite sign, their contributions to the transition energy can be neglected and Eqn 7.27 can be simplified to :[195]

$$\hbar\omega \simeq E_a^g(0) + E_{lh}^{a,b}(N,B) \qquad (7.28)$$

By plotting a "fan-chart" of magnetic field against different photon frequencies, the binding energy of the acceptor at zero field $E_a^g(0)$ can thus be found.

7.4.2 Experimental Techniques

All magneto-optical measurements in this work were carried out at 4.2 K using fixed photon energies and a continuous sweep of magnetic field ranging from 0 to 8T. Photon energies in the FIR region were provided by a coherent FIR laser system optically-pumped by a CO_2 laser (Edinburgh Instruments). By suitable choice of molecular gas mixture, the wavelength range of this system can extend from 70.5μm up to 1.22mm although only the three most intense lines at λ = 70.5, 96 and 118μm were used in these studies. The laser was operated in the continuous working (CW) mode with a power level of approximately 10mW and the FIR beam was chopped at approximately 600Hz. Further details of the experimental set-up for magneto-optical measurements can be found in Ref. 187. Unpolarized light in the Faraday configuration, where the incident radiation propagates in a direction parallel to the magnetic field, was used exclusively in this work. In order to enhance the sensitivity for detecting small amount of impurities in the substrate as well as carriers in the thin α-Sn films, photoconductivity spectra were taken in preference to transmission ones.[195]

These spectra may, however, be distorted as the sample resistance and hence the detection sensitivity changes with magnetic field. Extrinsic photoconductivity was detected using a cross modulation technique where the change in d.c. conductivity (σ_{xx}) was measured by phase sensitive techniques. The magnetic field was again provided by the Thor 8T system and the same rotatable insert and biasing circuitry were used as in SdH measurements. In fact, Hall, SdH and magneto-optical measurements were usually carried out on the same sample in succession in order to minimize the time and the amount of liquid He consumed during the sample changing process. To cut off any 9-10μm components in the FIR beam arising from pumping radiation, a TPX (poly 4 methyl pentene-1) window was mounted at the top end of the light-pipe which was fixed at the centre of the insert.

7.4.3 Results and Discussion

7.4.3.1 Photoconductivity Response at λ = 70.5μm

a) Structures originating from the p-InSb substrate

Fig. 7.11a shows the photoconductivity spectra taken at a laser wavelength of 70.5μm for a p-InSb substrate (doped with Cd) subjected to the normal cleaning procedure but without subsequent epitaxial growth. For Cd-doped p-InSb, holes are frozen out onto acceptor sites at temperatures below 14K. Using laser wavelengths of 10 to 70.5μm, Littler *et. al.*[195] were able to observe bound-hole transitions originating from heavy-hole-like ground states to final excited acceptor states associated with light-hole Landau levels with quantum number N = -1 to 27 at 4.2K. The transition energies deduced from the sharp structures recorded in Fig. 7.11a is in excellent agreement with their results. In this spectrum, the numbers used to identify the individual peaks refer to the light-hole Landau level with which the excited acceptor states are associated. With increasing wavelengths (i.e. 96 and 118μm), these bound-hole transitions were found to occur at lower magnetic field as expected. A fan-chart of magnetic fields against photon energies is plotted in Fig. 7.12. By extrapolating the experimental data back to zero field, the ground-state binding energy for the acceptors is found to be 8.9±0.3 meV. This energy is close to the values cited for Cd impurities in the literature.[195-197]

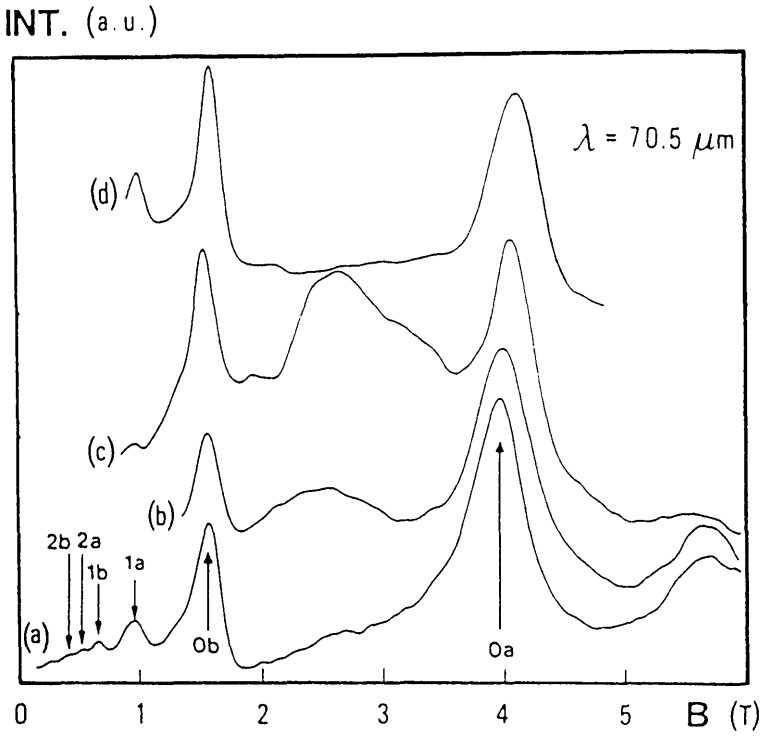


Fig. 7.11 Photoconductivity response recorded using a laser wavelength of 70.5μm for :

(a) A p-InSb(100) substrate subjected to pre-growth cleaning showing a series of bound-hole transitions. The labels refer to the light-hole Landau levels to which the excited impurity states are associated.

(b) A 200Å thick α-Sn/p-InSb(100) sample

(c) A 3000Å thick α-Sn/p-InSb(100) sample

(d) Sample (c) after being etched in HCl for 2 mins.

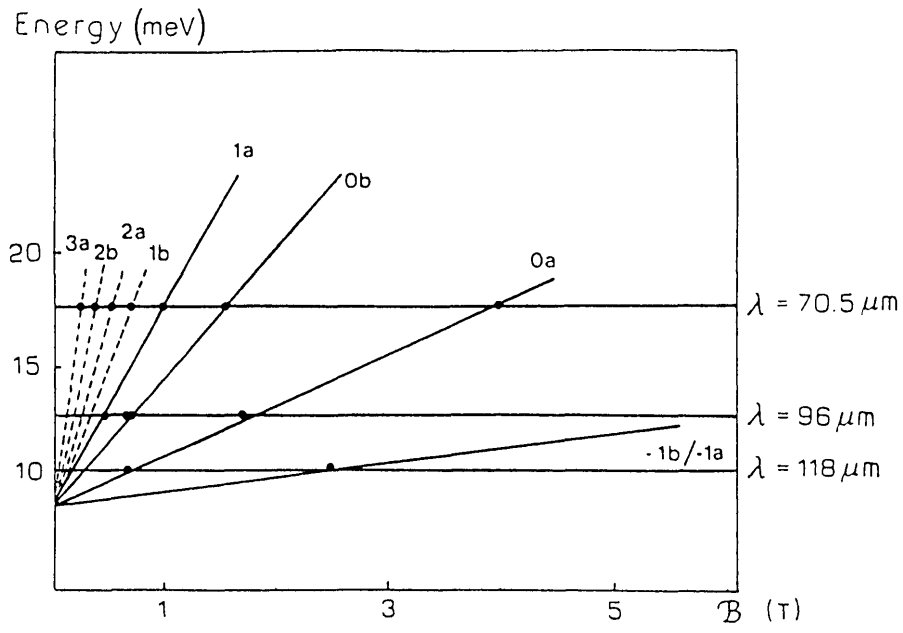


Fig. 7.12 A fan-chart of magnetic fields against photon energies.

(By extrapolating the experimental data back to zero field, the ground-state binding energy of the acceptor is found to be (8.9±0.3) meV.)

b) Structures originating from the 2DEG and the α-Sn film

Also shown in Fig. 7.11 are photoconductivity spectra taken from α-Sn/p-InSb structures with various overlayer thicknesses. The response in the field range of 2 to 3.5T is found to be dependent on the film thickness - the intensity increases as the film becomes thicker. At an overlayer thickness of 3000Å, a broad hump centred at about 2.6T is clearly observed (Fig. 7.11c) which is found to be quenched when the film thickness is effectively reduced by etching the surface (Fig. 7.11d). This broad feature, corresponding to an effective mass of $(0.018 \pm 0.002)m_o$, is thus related to the α-Sn overlayer although the effective mass value is too small compared with the bulk α-Sn value of approximately $0.024m_o$.[15,21,24] This discrepancy is believed to be the result of the strongly non-parabolic and warped energy surfaces characterizing the highly-strained pseudomorphic α-Sn overlayer. The complex band contour is reflected in the broadness of the cyclotron resonance peak which may include contributions from a range of effective masses associated with different points on the constant energy surface. Strong admixtures of the conduction and valence band wave function expected in narrow bandgap semiconductors can also cause broadening in the CR peaks.

7.4.3.1 Photoconductivity Response at λ = 96 and 118 μm

Using a longer wavelength of 96μm, transitions arising from both bound holes and free-carrier cyclotron resonance are expected to shift to lower magnetic field (see Fig. 7.13). Bound-hole transitions originating from the substrate dominate the photoconductivity spectra below 3T and the two peaks labelled S_1 and S_2 correspond to the light-hole Landau levels $0a$ and $-1b/-1a$ respectively to which the acceptors are excited. At higher field, an overlayer thickness dependence is again observed. A broad hump at about 5T (corresponding to effective masses in the range of $0.044m_o$ to $0.051m_o$) can be observed in the thinner film (Fig. 7.13a) which gradually diminishes as the film thickness increases (Fig. 7.13b). Transitions involving effective masses in this range are also observed in the photoconductivity response using a laser wavelength of 118μm. These transitions are tentatively attributed to the 2DEG at the interfacial region, where its influence on the overall conductivity of the sample is expected to decrease as the overlayer becomes thicker. However, it is still not possible to determine whether the 2DEG is confined at the α-Sn or the InSb side of the heterojunction. In both

cases, the Fermi level will be high due to strong non-parabolicity and high carrier concentration of the 2DEG. The effective masses associated with the 2-D electrons can thus be very large. In fact, in inversion layers on p-InSb surfaces with electron densities in excess of 3 x 10^{12} cm^{-2}, CR masses of the lowest subband are found to be larger than $0.040m_o$.[198,199]

In contrary to the broad hump centred at around 5T, two sharp peaks labelled A and B in the 96μm photoconductivity spectra (Fig. 7.13b) can only be observed in the thicker sample. Two similar peaks are also observed in the 118μm spectra at slightly lower field. These two peaks, corresponding to effective masses of $0.028m_o$ and $0.034m_o$, are believed to be cyclotron resonance structures which arise from the warped energy surfaces of the α-Sn overlayer. A broad cyclotron resonance structure centred at an effective mass of $0.033m_o$ has also been observed in an α-Sn/CdTe(001) heterostructure.[54]

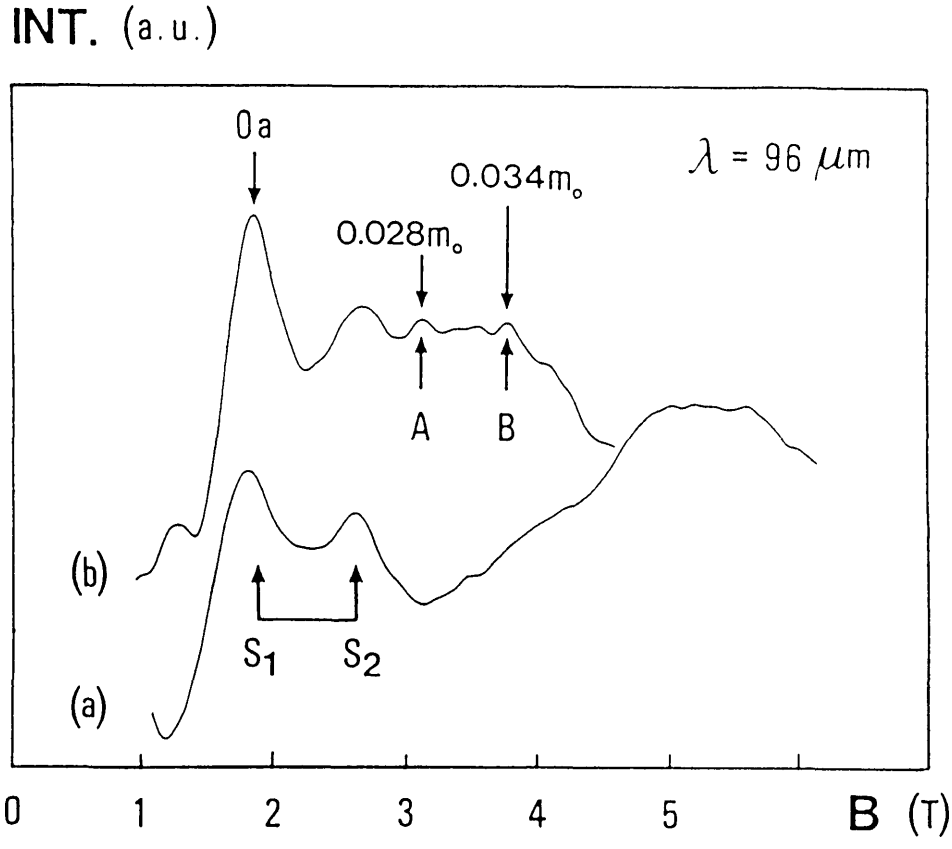


Fig. 7.13 Photoconductivity spectra recorded using a laser wavelength of 96μm for (a) 200Å and (b) 3000Å thick α-Sn films grown on p-InSb(100).

(S_1 and S_2 represent bound-hole transitions associated with the final states 0*a* and -1*b*/-1*a*. The two peaks labelled A and B are believed to be cyclotron resonance features arising from the warped energy surface of the α-Sn overlayer.)

7.5 Conclusions

In conclusion, results from conventional Hall measurements for the α-Sn/InSb system are difficult to interpret due to the multi-carrier conduction effect. The observation of a double reversal of sign in the Hall coefficient as the sample is cooled suggests that a n-type skin layer or a 2DEG may be present in this system. Tilted field SdH experiments demonstrate unambiguously the presence of a 2DEG with high carrier concentration at the interface of α-Sn/p-InSb(100) and (111) heterostructures. This is the first reported observation of a 2DEG in such structures.[55] The fact that very clear SdH oscillations with sharp peaks can be observed suggests that the mobility of the 2DEG is high. These experiments, however, cannot determine the origin (or origins) and the exact location of this 2DEG in any definitive manner and a number of possibilities are discussed. In theory, determination of the effective masses involved in the conduction can provide the answer. Photoconductivity spectra from magneto-optical experiments revealed several sets of cyclotron resonance structures corresponding to a wide range of effective masses. From the overlayer thickness dependence of the photoconductivity response, some of these features can be tentatively assigned to the 2DEG and some to free carriers in the α-Sn films. However, due to the fact that these cyclotron resonance energies overlap with those of the bound-hole transitions originating from the p-InSb substrate, and that large effective masses resulting from high carrier concentrations and strong non-parabolicity can be obtained in both α-Sn and InSb, magneto-optical measurements also cannot unambiguously identify the origin nor the location of the 2DEG.

CHAPTER 8 CONCLUSIONS

The work presented in this thesis was oriented towards the growth and characterization of α-Sn films on InSb substrates by MBE. Bulk α-Sn is a symmetry-induced zero-bandgap semiconductor. By applying a uniaxial stress or by alloying with Ge, a small bandgap can be opened up. Epitaxial α-Sn films, substrate-stabilized to temperatures near 100°C, thus have potential in infrared device applications.

Substrate quality was found to be extremely important for the pseudomorphic growth of α-Sn films since the α → β phase transformation was found to originate from defect sites. Several cleaning methods for InSb substrates were studied using surface science techniques. The most satisfactory result was achieved using a modified CP4A etchant (HNO_3 : CH_3COOH : HF : DI H_2O @ 2 : 1 : 1 : 10) followed by a combination of low energy Ar ion bombardment (~350eV) and low temperature annealing (~275 °C).

The growth of α-Sn films was carried out in a custom-designed MBE system and the effect of growth conditions on the surface quality and stability of these films was studied. It was found that coherent, single-phase α-Sn films more than 1500Å thick could only be grown on InSb substrates with (100) orientation. The α → β phase transition temperature, used as a measure of stability of the α-Sn film, was found to be dependent on the overlayer thickness. It was shown that thinner films had a higher transition temperature (~130°C for a 200Å thick film) than thicker ones (~90°C for a 4000Å thick film). Such behaviour is expected since the substrate stabilization effect would be reduced with increasing overlayer thickness. The higher transition temperature attainable in thinner films offers the possibility of growing α-Sn/InSb superlattices that would be stable enough for device applications. Due to the enhanced migration of surface adatoms, films grown at elevated substrate temperatures and slow growth rates were found to produce sharper RHEED patterns, corresponding to better surface ordering. On the other hand, preferential diffusion of Sb into the overlayer was detected in films grown under these conditions. Optimum growth conditions were achieved with growth rates in the range of 0.5 to 0.7Å/s and substrates temperatures between 10 and 50°C. Using this

set of growth conditions, it was demonstrated that high quality α-Sn films with good surface morphology could be stabilized up to temperatures near 100°C.

The structural properties of α-Sn films grown on InSb(100) substrates were studied in detail using the RHEED technique. Clean InSb(100) surfaces prior to growth were found to exhibit predominantly (4x2) structures with a small amount of c(8x2) domains. The co-existence of these two structures gave rise to curved 1/2-order diffraction streaks in the <100> azimuths. The initial growth of α-Sn overlayers was found to be characterized by disorder features caused by either the breakage of dimer bonds along the substrate surface or by atomic rearrangement at the interface. This was followed by a layer-by-layer growth mode for films thicker than 20Å. It was also shown that α-Sn films exhibited thickness-dependent surface reconstructions. Two-domain (2x1), (2x2), c(4x4) as well as atomic step structures were observed. The surface structure of α-Sn(100) was found to be very similar to that of Si(100) and a structural model based on dimers was proposed.

The electrical properties of the α-Sn/InSb heterostructure studied by magneto-transport (Hall and SdH effect) and magneto-optical techniques were found to be dominated by a high concentration, high mobility 2DEG at the interface. Due to multi-carrier conduction effects, data from Hall measurements were difficult to analyze and required careful interpretation. Two-dimensionality of the electron gas was demonstrated by the $1/\cos\vartheta$ dependence of the observed SdH oscillations in tilted field experiments. The total carrier concentration of the 2DEG was found to be around 6×10^{12} cm^{-2} with at least seven subbands being occupied at 4.2K. An overlayer thickness dependence of individual subband occupancy was observed. Magneto-optical spectra for α-Sn/InSb samples were found to be very complicated. Bound hole transitions originating from the InSb substrate as well as some broad structures with different overlayer thickness dependence were observed. The latter were believed to arise from cyclotron resonance transitions involving the 2DEG (corresponding to effective masses between $0.044m_o$ to $0.051m_o$) and the warped energy surfaces of the highly-strained pseudomorphic α-Sn overlayer (corresponding to $0.018m_o$ and between $0.028m_o$ to $0.034m_o$). Neither SdH nor magneto-optical measurements were able to identify unambiguously the origin and location of the 2DEG although cross-doping, band-bending and

quantum size effects were all thought to be able to contribute to its occurrence.

APPENDIX : LIST OF PUBLICATIONS

1. "Pseudomorphic Growth of α-Sn on InSb(100) by MBE"
   Yuen W.T., Liu W.K., Hodge C.C., Holmes S.N., Wang P.D. and Stradling R.A.
   Proc. IOP Solid State Phys. Conf., Nottingham, 20-22 Dec., 1988 (KP7)

2. "A study of the Cleaning of InSb(100) Substrates by XPS"
   Yuen W.T., Liu W.K., Evans S., Egdell R.G. and Stradling R.A.
   Proc. IOP Solid State Phys. Conf., Nottingham, 20-22 Dec., 1988 (DP101)

3. "First Observation of a Two-Dimensional Electron Gas at the Interface of α-Sn/InSb(100) Grown by Molecular Beam Epitaxy"
   Yuen W.T., Liu W.K., Holmes S.N. and Stradling R.A.
   Semicond. Sci. Technol. **4**, 819 (1989)

4. "RHEED Studies of the Surface Morphology of α-Sn Pseudomorphically Grown on InSb(100) by MBE : a New Kind of Non-polar/Polar System"
   Yuen W.T., Liu W.K., Joyce B.A. and Stradling R.A.
   Semicond. Sci. Technol. **5**, 373 (1990)

5. "A Two-Dimensional Electron Gas (2DEG) at the Interface of a Non-polar/Polar System : α-Sn/InSb(100) and $(\bar{1}\bar{1}\bar{1})$"
   Yuen W.T., Liu W.K., Stradling R.A. and Joyce B.A.
   Proc. IOP Solid State Phys. Conf., Warwick, 19-21 Dec., 1989 (STD31)

6. "A Two-Dimensional Electron Gas (2DEG) at the Interface of a Non-polar/Polar System : α-Sn/InSb(100) and $(\bar{1}\bar{1}\bar{1})$"
   Yuen W.T., Liu W.K., Stradling R.A. and Joyce B.A.
   Proc. 119th TMS Conf., Anaheim, 18-24 Feb., 1990

7. "A Two-Dimensional Electron Gas (2DEG) at the Interface of α-Sn Thin Films Grown on InSb(100) and $(\bar{1}\bar{1}\bar{1})$ by MBE"
   Yuen W.T., Liu W.K., Holmes S.N. and Stradling R.A.
   Proc. 20th Intl. Conf. Phys. Semicond., Thessaloniki, Aug., 1990

8. "The Growth and Electronic Properties of α-Sn Thin Films Grown on InSb(100) and $(\bar{1}\bar{1}\bar{1})$ Substrates by Molecular Beam Epitaxy (MBE)"
   Yuen W.T., Liu W.K., Stradling R.A. and Joyce B.A.
   accepted for publication in J. Cryst. Gr. (1991)

9. "The Design of a Cost Effective and High Performance Molecular Beam Epitaxy System"
   Yuen W.T., Liu W.K. and Stradling R.A. (to be published)

REFERENCES

1. Busch G.A. and Kern R. Solid State Phys. **7**, 1 (1963)
2. Ewald A.W. and Tufte O.N. J. Appl. Phys. **29**, 1007 (1958)
3. Groves G. and Paul W. Phys. Rev. Lett. **11**, 194 (1963)
4. Ewald A.W. Helv. Phys. Acta. **41**, 795 (1968)
5. Farrow R.F.C., Robertson D.S., Williams G.M., Cullis A.G., Jones G.R., Young I.M. and Dennis P.N.J. J. Cryst. Gr. **54**, 507 (1981)
6. Tu L.W., Wong G.K. and Ketterson J.B. Appl. Phys. Lett. **54**, 1010 (1989)
7. Youngdale E.R., Hoffman C.A., Meyer J.R., Bartoli F.J., Engelhardt M.A., Niles, D.W. and Höchst, H. Semicond. Sci. Technol. **5**, S253 (1990)
8. Broerman J.G. Phys. Rev. Lett. **45**, 747 (1980)
9. Schulman J.N. and McGill T.C. Appl. Phys. Lett. **34**, 663 (1973)
10. Paul W. Semicond. Sci. Technol. **5**, S253 (1990)
11. Busch G.A., Wieland J. and Zoller H. Helv. Phys. Acta. **41**, 795 (1968)
12. Groves S.H., Pidgeon C.R., Ewald A.W. and Wagner R.J. J. Phys. Chem. Solid **31**, 2031 (1970)
13. Bassini F. and Liu L. Phys. Rev. **132**(5), 2047 (1963)
14. Tufte O.N. and Ewald A.W. Phys. Rev. **122**, 1431 (1961)
15. Hinkley E.D. and Ewald A.W. Phys. Rev. **134**, A1261 (1964)
16. Kohnke E.E. and Ewald A.W. Phys. Rev. **102**(6), 1481 (1956)
19. Chelikowsky J.R. and Cohen H.L. Phys. Rev. **B14**(2), 556 (1976)
20. Lavine C.F. and Ewald A.W. J. Phys. Chem. Solid **32**, 1121 (1971)
21. Booth B.L. and Ewald A.W. Phys. Rev. **168**, 796 (1968)
22. Booth B.L. and Ewald A.W. Phys. Rev. Lett. **18**(13), 491 (1967)
23. Linquist R.E. and Ewald A.W. Phys. Rev. **135**(1A), A191 (1964)
24. Wagner R.J. and Ewald A.W. J. Phys. Chem. Solid **32**, 697 (1971)
25. Roman B.J. and Ewald A.W. Phys. Rev. **B5**, 3914 (1972)
26. Liu L. and Brust D. Phys. Rev. Lett. **20**(13), 651 (1968)
    Averous M. Phys. Stat. Sol.(b) **95**, 9 (1979)
27. Zawadzki W. Adv. Phys. **23**, 435 (1974)
28. Craig B.I. and Garrison B.J. Phys. Rev. **B33**, 8130 (1986)
29. Tang M., Niles D.W., Herněndez-Calderón I. and Höchst H. Phys. Rev. **B36**(6), 3336 (1987)
30. Höchst H., Engelhardt M.A. and Niles D.W. SPIE **1106**, 165 (1989)

31. Oguz S., Paul W., Deutsch T.F., Tsauer B.Y. and Murphy D.V.
Appl. Phys. Lett. **43**(9), 848 (1983)
32. Klemm W. and Stöhr H. Z. Anorg. Chem. **241**, 305 (1939)
33. Menéndez J. and Höchst H. Thin Solid Film **111**, 375 (1984)
34. Satoh S. and Kimata M. J. Cryst. Gr. **95**, 564 (1989)
35. Hernéndez-Calderón I. and Höchst H. Phys. Rev. **B27**(8), 4961 (1983)
36. John P., Miller T. and Chiang T.C. Phys. Rev. **B39**(5), 3223 (1989)
37. Woodruff D.P. and Horn K. Phil. Mag. **A47**(3), L5 (1983)
Vacuum **33**(10-12), 633 (1983)
38. Yuen W.T., Liu W.K., Joyce B.A. and Stradling R.A.
Semicond. Sci. Technol. **5**, 373 (1990)
39. Höchst H. and Hernéndez-Calderón I. Surf. Sci. **126**, 25 (1983)
40. Middelmann H.U., Sorba L., Hinkel V. and Horn K.
Phys. Rev. **B35**(2), 718 (1987)
41. Tersoff J. Phys. Rev. Lett. **56**, 2755 (1986) and ref. therein
42. Asom M.T., Kortan A.R., Kimerling L.C. and Farrow R.C.
Appl. Phys. Lett. **55**(14), 1439 (1989)
43. Viña L., Höchst H. and Cardona M. Phys. Rev. **B31**(2), 958 (1985)
44. Hernéndez-Calderón I. and Höchst H. Surf. Sci. **152/153**, 1035 (1985)
45. Höchst H. and Hernéndez-Calderón I.
J. Vac. Sci. Technol. **A3**(3), 911 (1985)
46. Kasukabe Y., Iwai M. and Osaka T.
Jap. J. Appl. Phys. **27**(7), L1201 (1988)
47. Yuen W.T., Liu W.K., Stradling R.A. and Joyce B.A.
accepted for publication in J. Cryst. Gr. (1991)
48. Amornkitbamrung V. and Chatrophorn S. J. Cryst. Gr. **84**, 326 (1987)
49. Höchst H., Engelhardt M.A., Bowman R.C.Jr. and Adams P.M.
Semicond. Sci. Technol. **5**, S240 (1990)
50. Takatani S. and Chung Y.W. Phys. Rev. **B31**(4), 2290 (1985)
51. Tu L.W., Wong G.K., Song S.N., Zhao Z. and Ketterson J.B.
Appl. Phys. Lett. **55**(25), 2643 (1989)
Semicond. Sci. Technol. **5**, S245 (1990)
52. Tu L.W., Wong G.K. and Ketterson J.B.
Appl. Phys. Lett. **55**(13), 1327 (1989)
53. Song S.N., Yi X.J., Zheng J.Q., Zhao Z., Tu L.W., Wong G.K., and
Ketterson J.B. Phys. Rev. Lett. **65**(2), 227 (1990)

54. Wojtowicz T., Dobrowolska M., Yang G., Luo H., Furdyna J.K., Tu L.W. and Wong G.K. Semicond. Sci. Technol. **5**, S248 (1990)
55. Yuen W.T., Liu W.K., Holmes S.N. and Stradling R.A. Semicond. Sci. Technol. **4**, 819 (1989)
56. Hoffman C.A., Meyer R.J., Wagner R.J., Bartoli F.J., Engelhardt M.A. and Höchst H. Phys. Rev. **B40**(17), 11693 (1989)
57. Youngdale E.R., Hoffman C.A., Meyer J.R., Bartoli F.J., Han J.W., Cook J.W.Jr., Schetzina J.E., Engelhardt M.A., Niles D.W. and Höchst H. J. Vac. Sci. Technol. **A8**(2), 1215 (1990)
58. Reno J.L. and Stephenson L.L. Appl. Phys. Lett. **54**(22), 2207 (1989)
59. Höchst H., Niles D.W. and Herněndez-Calderón I. J. Vac. Sci. Technol. **B6**(4), 1219 (1988)
60. Shah S.I., Greene J.E., Abels L.L., Yao Q. and Raccah P.M. J. Cryst. Gr. **83**, 3 (1987)
61. Romano L., Sundgren J.E., Barnett S.A. and Greene J.E. Superlattices & Microstructures **2**(3), 233 (1986)
62. Shah S.I., Greene J.E., Abels L.L. and Raccah P.M. J. Cryst. Gr. **91**, 71 (1986)
63. Pukite P.R., Harwit A. and Iyer S.S. Appl. Phys. Lett. **54**, 2142 (1989)
64. Asom M.T., Fitzgerald E.A., Kortan A.R., Spear B. and Kimerling L.C. Appl. Phys. Lett. **55**(6), 578 (1989)
65. Jenkins D.W. and Dow J.D. Phys. Rev. **B36**(15), 7994 (1987)
66. Höchst H., Engelhardt M.A. and Herněndez-Calderón I. Phys. Rev. Lett. **40**(14), 9703 (1989)
67. Wegscheider W., Eberl K., Menczigar U. and Abstreiter G. Appl. Phys. Lett. **57**(9), 875 (1990)
68. Gallerneault W.M.T., Vnuk F. and Smith R.W. J. Appl. Phys. **54**(7), 4200 (1983)
69. Hanke M., Rücker H., Enderlein R. and Bechstedt F. Proc. 19th Intl. Conf. Phys. Semicond. **1**, 511 (1988)
70. Günther K.G. Z. Naturforsch. A **13a**, 1081 (1958)
71. Davey J.E. and Pankey T. J. Appl. Phys. **39**, 1941 (1968)
72. See review by Joyce B.A. Rep. Prog. Phys. **37**, 363 (1974)
73. Arthur J.R.Jr. J. Appl. Phys. **39**, 4032 (1968)
74. Cho A.Y. and Arthur J.R. Prog. Sol. St. Chem. **10**(3), 157 (1975)
75. Stringfellow G.B. Rep. Prog. Phys. **45**, 469 (1982)

76. Weeks J.D. and Gilmer G.H. Adv. Chem. Phys. **40**, 157 (1979)
77. Venables J.A., Spiller, G.D.T. and Hanbücken M.
Rep. Prog. Phys. **47**, 399 (1984)
78. Bauer E. and Poppa H. Thin Solid Films **12**, 167 (1972)
79. Zhang X., Staton-Becan A.E., Pashley D.W., Parker S.D., Droopad R., Williams R.L. and Newman R.C. J. Appl. Phys. **67**(2), 800 (1990)
80. Neave J.H., Joyce B.A., Dobson P.J. and Norton N.
Appl. Phys. **A31**, 1 (1983)
81. Sakamoto T., Kawamura T., Nago S., Hashiguchi G., Sakamoto K. and Kuniyoshi K. J. Cryst. Gr. **81**, 59 (1987)
82. Gilmer G.H. and Grabow M.H. J. Metals **39**, 19 (1987)
83. Burton W.K., Cabrera N. and Frank F.C.
Phil. Trans./R. Soc. A **243**, 299 (1951)
84. "The Technology and Physics of Molecular Beam Epitaxy"
Ed. Parker E.H.C. (Plenum Press 1985)
85. Joyce B.A. Rep. Prog. Phys. **48**, 1637 (1985)
86. Kloog K. in "Crystals - Growth, Properties and Applications" **3**, pp. 73
Ed. Freyhardt H.C. (Springer 1980)
87. "Molecular Beam Epitaxy" Ed. Pamplin B.R. (Pergamon Press 1980)
88. "Molecular Beam Epitaxy : Fundamental and Current Status"
Eds. Herman M.A. and Sitter M. (Springer-Verlag 1988)
89. See review by Madhukar A. Surf. Sci. **132**, 344 (1983)
90. See e.g. : Charasse M.N. and Hirtz J.P Phys. World **3**(1), 28 (1990)
91. Barnett S.A. and Rockett A. Surf. Sci. **198**, 133 (1988)
92. Tromp R.M., Hamers R.J. and Demuth J.E.
Phys. Rev. Lett. **55**(12), 1303 (1985)
93. Clarke S. and Vvedensky D.D. Phys. Rev. **B37**(11), 6559 (1988)
94. Aarts J., Gerits W.M. and Larsen P.K.
Appl. Phys. Lett. **48**, 931 (1986)
95. Clarke S., Wilby M.R., Vvedensky D.D., Kawamura T. and Sakamoto T.
Appl. Phys. Lett. **54**(24), 2417 (1989)
96. Bauer E. in "Techniques of Metals Research", **II**(2), pp. 501
Ed. Bunshah R.F. (Interscience Publishers 1969)
97. Frank F.C. and van der Merwe J.H. Proc. R. Soc. A **198**, 216 (1949)
98. Jesser W.A. and Kuhlmann-Wilsdolf D. Phys. Stat. Sol. **19**, 95 (1967)
99. Blanc J. in "Heteroepitaxial Semiconductors for Electronic Devices"
pp. 282, Ed. Cullen G.W. and Wang C.C. (Springer-Verlag 1978)

100. Jesser W.A. and Matthews J.W. Phil. Mag. **15**. 1097 (1967)
101. Harrison W.A., Kraut E.A., Waldrop J.R. and Grant R.W.
Phys. Rev. **B18**(8), 4402 (1978)

102. see for example (and ref. therein) :
Chang C.A. and Kuan T.S J. Vac. Sci. Technol. **B1**, 315 (1983)
103. Bauer R.S. and Mikkelsen J.C.Jr. J. Vac. Sci. Technol. **21**, 491 (1982)
104. Kroemer H. J. Cryst. Gr. **81**, 193 (1987)
105. Cho A.Y. Thin Solid Films **100**, 291 (1983)
106. Bowman R.C.Jr., Adams P.M., Engelhardt M.A. and Höchst H.
J. Vac. Sci. Technol. **A8**(3), 1577 (1990)
107. Chang C.C., Citrin P.H., Schwartz B.
J. Vac. Sci. Technol. **14**(4), 943 (1977)
108. Henneke H.L. J. Appl. Phys. **36**, 2967 (1965)
109. Luft B.D., Khusid L.B., Yassen M.L. and Milyavskii Yu. S.
Inorg. mater. **20**(8), 1087 (1984)
110. Bosch A.J., van Welzenis R.G. and Schanen O.F.Z.
J. Appl. Phys. **58**(9), 3434 (1985)
111. Auret F.D. J. Electrochem. Soc. **131**(9), 2115 (1984)
112. Vasquez R.P., Lewis B.F. and Grunthaner F.J.
J. Appl. Phys. **54**(3), 1365 (1983)
113. Farrow R.F.C., Cullis A.G.M., Grant A.J. and Pattison J.E.
J. Cryst. Gr. **45**, 292 (1978)
114. Bean J.C., Becker G.E., Petroff P.M. and Seidel T.E.
J. Appl. Phys. **48**(3), 907 (1977)
115. Zheng Y-D., Chang Y.H., McCombe B.D., Farrow R.F.C., Temofomte T.
and Shirland F.A. Appl. Phys. Lett. **49**(18), 1187 (1986)
116. Noreika A.J., Francombe M.H. and Wood C.E.C.
J. Appl. Phys. **52**(12), 7416 (1981)
117. Ashley T., Dean A.B., Elliott C.T., McConville C.F. and Whitehouse C.R.
Electronics Lett. **24**(20), 1270 (1988)
118. Oe K., Ando S. and Sugiyama K.
Jap. J. Appl. Phys. **19**(7), L417 (1980)
119. Aspnes D.E. and Studna A.A. Appl. Phys. Lett. **39**(4), 316 (1981)
120. Noreika A.J., Greggi J. Jr., Takei W.J. and Francombe M.H.
J. Vac. Sci. Technol. **A1**(2), 558 (1983)
121. Allen J.W. Phil. Mag. **2**, 1475 (1957)

122. Woolf D.A., Westwood D.I. and Williams R.H.
Semicond. Sci. Technol. **4**, 1127 (1989)
123. Hirofuji Y. and Matsuo N. J. Vac. Sci. Technol. **B5**(1), 10 (1987)
124. Tang X., van Welzenis R.G., van Setten F.M. and Bosch A.J.
Semicond. Sci. Technol. **1**, 355 (1986)
125. Bregman J., Shapira Y., Calahorra Z. and Goshen R.
Thin Solid Films **125**, 347 (1985)
126. "Practical Surface Analysis by Auger and X-ray Photoelectron Spectroscopy" Eds. Brigg D. and Seah M.P.
John Wiley and Sons, Chichester 1981
127. Feuerbacher B. and Fitton B. in "Electron Spectroscopy for Surface Anaysis" Ed. Ibach H., Springer Verlag 1977
128. Werner H.W. and Garten R.P.H. Rep. Prog. Phys. **47**, 221 (1984)
129. Fadley C.S. in "Electron Spectroscopy : Theory, Techniques and Applications " Eds. Brundle C.R. and Baker A.D.
Academic Press, London (1978)
130. Iwasaki H., Mizokawa Y., Nishitani R. and Nakamura S.
Surf. Sci., **86**, 811 (1979)
131. Copperthwaite R.G., Kunze O.A., Lloyd J., Neely J.A., Tuma W.
Z. Naturforsch. **A33**, 523 (1978)
132. Iwasaki H., Mizokawa Y., Nishitani R. and Nakamura S.
Jap. J. Appl. Phys. **17**(11), 1925 (1978)
133. Lin A.W.C., Armstrong N.R. and Kuwana T.
Analy. Chem. **49**(8), 1228 (1977)
134. Holm R. and Storp S. Appl. Phys. **9**, 217 (1976)
135. Hewitt R.W. and Winograd N. J. Appl. Phys. **51**(5), 2620 (1980)
136. Legare P., Hilaire L. and Maire G.
Microsc. Spectrosc. Electron. **5**, 771 (1980)
137. Morgan W.E., Stu W.. and van Wazer J.R.
Inorg. Chem. **12**(4), 953 (1973)
138. Hagi-Ali M., Stuck R., Saxena A.N. and Siffert P.
Appl. Phys. **19**, 25 (1979)
139. Wilmsen C.W. J. Vac. Sci. Technol. **13**(11), 64 (1976)
140. Dewald J.F. J. Electrochem. Soc. **104**(4), 244 (1957)
141. Scofield J.H. J. Elec. Spectrosc. Relat. Phenom. **8**, 129 (1976)
142. Spanjaard D., Guillot C., Desjonquères M.C., Tréglia G. and Lecante J.
Surf. Sci. Rep. **5**(1/2), 1 (1985)

143. Chang C.C. Surf. Sci. **25**, 53 (1971)
144. Davis L.E., MacDonald N.C., Palmberg P.W., Riach G.E. and Weber R.E. "Handbook of Auger Electron Spectroscopy" 2nd Ed. Phys. Elec. Div., Perkin-Elmer Corp. 1976
145. Auret F.D. J. Electrochem. Soc. **129**(12), 2752 (1982)
146. Chang C.C. Surf. Sci. **48**, 9 (1975)
147. Cho A.Y. and Cheng K.Y. Appl. Phys. Letts. **38**, 360 (1981)
148. Farley C.W., Crook G.E., Kesan V.P., Block T.K., Stevens H.A., Mattord T.J., Neikirk D.P. and Streetman B.G. J. Vac. Sci. Technol. **B5**(5), 1374 (1987)
149. Farrow R.F.C. and Williams G.M. Thin Solid Films **55**, 303 (1978)
150. Mattern M. and Lüth H. Surf. Sci. **126**, 502 (1983)
151. Davisson C. and Germer L.H. Phys. Rev. **30**, 705 (1927)
152. Thomson G.P. and Reid A. Nature **119**, 890 (1927)
153. Nishikawa S. and Kikuchi S. Proc. Imp. Acad. Jap. **4**, 475 (1928)
154. de Broglie L. Phil. Mag. **47**, 446 (1924)
155. Henzler M. 'Electron Spectroscopy for Surface Analysis', pp.117, Ed. Ibach H., Springer Verlag (1977)
156. Hirsh P.B., Howie A., Nicholson R.D. and Pashley D.W. 'Electron Microscopy of Thin Crystals', London Butterworths (1965)
157. Joyce B.A., Neave J.H., Dobson P.J. and Larsen P.K. Phys. Rev. **29**(2), 814 (1984)
158. Neave J.H. and Joyce B.A. J. Cryst. Growth **44**, 387 (1978)
159. Russell G.J. Prog. Cryst. Gr. & Charact. **5**, 291 (1982)
160. Masud N. and Pendry J.B. J. Phys. C **9**, 814 (1976)
161. Holloway S. and Beeby J.L. J. Phys. C **11**, L247 (1978)
162. Prutton M. 'Surface Science' 2nd. Ed., Oxford Sci. Pub. (1983)
163. Hottier F., Theeten J.B., Masson A. and Domange J.L. Surf. Sci. **65**, 563 (1977)
164. Henzler M. Appl. Surf. Sci. **11/12**, 450 (1982)
165. Larsen P.K. and Chadi D.J. Phys. Rev. **B37**(14), 8282 (1988)
166. Zhang X., Staton-Bevan A.E., Pashley D.W., Parker S.D., Droopad R., Williams R.L. and Newman R.C. J. Appl. Phys. **67**(2), 800 (1990)
167. Clarke S. and Vvedensky D.D. J. Appl. Phys. **63**(7), 2272 (1988)
168. Ihm J., Lee D.H., Joannopoulos J.D. and Barker A.N. J. Vac. Sci. Technol. **B1**, 705 (1983)

169. Tromp R.M., Hamers R.J. and Demuth J.E.
Phys. Rev. Lett. **55**, 1303 (1985)
170. Martin J.A., Savage D.E., Moritz W. and Lagally M.G.
Phys. Rev. Lett. **56**, 1936 (1986)
171. Tabata T., Aruga T. and Murata Y. Surf. Sci. **179**, L63 (1986)
172. Cardillo M.J. and Becker G.E. Phys. Rev. **B21**(4), 1497 (1980)
173. Chadi D.J. Appl. Optics **19**, 3971 (1980)
174. Wang H.C., Lin R.F. and Wang X. Phys. Rev. **B36**, 7712 (1987)
175. Kato K., Ide T., Nishimori T. and Ichinokawa T
Surf. Sci. **207**, 177 (1988)
176. Pandey K.C. Proc. 17th. Intl. Conf. Phys. of Semicond., 55 (1985)
177. Norton N.G. Vacuum **33**(10-12), 621 (1983)
178. Kaplan R. Surf. Sci. **93**, 145 (1980)
179. Phillips J.C. Phys. Rev. Lett. **45**(11), 905 (1980)
180. Stradling R.A. in "Growth and Characterisation of Semiconductors",
Ed. Stradling R.A. and Klipstein, P.C. (Adam Hilger 1990)
181. Lou L.F. and Frye W.H. J. Appl. Phys. **56**(8), 2253 (1984)
182. Ando T., Fowler A.B. and Stern F. Rev. Mod. Phys. **54**, 437 (1982)
183. see for example : Blakemore J.S. "Solid State Physics" 2nd Ed.
(Cambridge University Press 1974)
Smith R.A. "Semiconductors" 2nd Ed.
(Cambridge University Press 1978)
184. Anderson D.A. and Apsley A. Semicond. Sci. Technol. **1** 187 (1986)
185. Beck W.A. and Anderson J.R. J. Appl. Phys. **62**(2), 541 (1987)
186. van der Pauw L.J. Philips Res. Rep. **13**(1), 1 (1956)
187. Holmes S.N. PhD Thesis, Imperial College, London (1989)
188. see for example : Seeger "Semiconductor Physics" 2nd Ed.
(Springer-Verlag 1985)
Singleton J. D. Phil. Thesis, Wadham College,
Oxford (1988)
189. Landwehr G. Festkörperprobleme **15**, 49 (1975)
190. see for example : Dorda G. Festkörperprobleme **13**, 215 (1973)
Dingle R. Festkörperprobleme **15**, 21 (1975)
191. Stradling R.A. Proc. EPS Condensed Matter Conf., Lisbon, 1990
to be published in Physica Scripta
192. Brummell M.A., Hopkins M.A., Nicholas R.J., Portal J.C., Cheng K.Y.
and Cho A.Y. J. Phys. C. **19**, L107 (1986)

193. Pidgeon C.R. and Brown R.N. Phys. Rev. **146**, 575 (1966)
194. Lin-Chung P.J. and Henvis B.W. Phys. Rev. **B12**(2), 630 (1975)
195. Littler C.L., Seiler D.G., Kaplan R. and Wagner R.J.
Phys. Rev. **B27**(12), 7473 (1983)
196. Littler C.L., Seiler D.G., Kaplan R. Wagner R.J. and Zawadzki W.
Solid State Commun. **37**, 783 (1981)
197. Müller H.-U., Ludwiz F. and Herrmann R.
Solid State Commun. **65** (7), 761 (1988)
198. Daerr A., Kotthaus J.P. and Koch J.F.
Solid State Commun. **17**, 455 (1975)
199. Merkt U., Horst M., Evelbauer T. and Kotthaus J.P.
Phys. Rev. **B34**(10), 7234 (1986)